AD-A259 272

(2)

Final Scientific Report AFOSR-TR- 93 0007

on

FUNDAMENTAL PROCESSES IN PARTIALLY IONIZED PLASMAS

Grant-AFOSR-88-0264

...and is ...0-12

Prepared for

AIR FORCE OFFICE OF SCIENTIFIC RESEARCH

DTIC ELECTE JAN1 3 1993 S C D

For the Period

July 1, 1988 to September 30, 1992

Submitted by

C. H. Kruger, Principal Investigator

HIGH TEMPERATURE GASDYNAMICS LABORATORY
Mechanical Engineering Department
Stanford University

H-20774

93-00732 8/P3

93 1 12 028

Final Scientific Report

on

FUNDAMENTAL PROCESSES IN PARTIALLY IONIZED PLASMAS

Prepared for

AIR FORCE OFFICE OF SCIENTIFIC RESEARCH

For the Period

July 1, 1988 to September 30, 1992

Submitted by

C. H. Kruger, Principal Investigator

DTIC QUALITY INSPECTED 1

Accession For
NTIS GRA&I ☑
DTIC TAB ☐
Unannounced ☐
Justification
By
Distribution/
Availability Codes
Dist | Avail and/or Special
A-1

URITY CLASSIFICATION OF THIS PAGE

REPORT DOCUMENTATION PAGE

REPORT SECURITY CLASSIFICATION **Unclassified**	1b RESTRICTIVE MARKINGS **None**
SECURITY CLASSIFICATION AUTHORITY	3. DISTRIBUTION / AVAILABILITY OF REPORT **Six copies of the Final Technical Report to AFOSR as per "A. Final Technical Report" of Air Force Grant Report Requirements**
DECLASSIFICATION / DOWNGRADING SCHEDULE	
PERFORMING ORGANIZATION REPORT NUMBER(S)	5. MONITORING ORGANIZATION REPORT NUMBER(S)
NAME OF PERFORMING ORGANIZATION **Stanford University** 6b. OFFICE SYMBOL (If applicable)	7a. NAME OF MONITORING ORGANIZATION **Air Force Office of Scientific Research**
ADDRESS (City, State, and ZIP Code) **Department of Mechanical Engineering Stanford, CA 94305-3030**	7b. ADDRESS (City, State, and ZIP Code) **Program Manager, Physical & Geophysical Sci. AFOSR, Bolling Air Force Base Washington, DC 20332-6448**
NAME OF FUNDING / SPONSORING ORGANIZATION **Air Force Office of Scientific Research** 8b. OFFICE SYMBOL (If applicable) **AFOSR NE**	9. PROCUREMENT INSTRUMENT IDENTIFICATION NUMBER **Grant AFOSR-88-0264**
ADDRESS (City, State, and ZIP Code) **Program Manager, Physical & Geophysical Sci. AFOSR, Bolling Air Force Base Washington, DC 20332-6448**	10. SOURCE OF FUNDING NUMBERS PROGRAM ELEMENT NO: **61102F** / PROJECT NO: **2301** / TASK NO: **A7** / WORK UNIT ACCESSION NO:

TITLE (Include Security Classification)

Fundamental Processes in Partially Ionized Plasmas

PERSONAL AUTHOR(S)
C.H. Kruger, P.I., Christophe Laux

TYPE OF REPORT	13b. TIME COVERED	14. DATE OF REPORT (Year, Month, Day)	15. PAGE COUNT
Final Scientific Report	FROM **7/1/88** TO **9/30/92**	**1992 November**	

SUPPLEMENTARY NOTATION

COSATI CODES			18. SUBJECT TERMS (Continue on reverse if necessary and identify by block number)
FIELD	GROUP	SUB-GROUP	**Plasmas, Radiation Diagnostics, Radiation Modeling**

ABSTRACT (Continue on reverse if necessary and identify by block number)

This report describes research results on Fundamental Processes in Partially Ionized Plasmas obtained in the High Temperature Gasdynamics Laboratory at Stanford University. This research has emphasized studies of plasma properties and associated diagnostics. The present report discusses, in the first part, optical diagnostics in air plasmas and, in the second part, measurements of the radiative emission of such plasmas. These experimental results have unveiled severe deficiencies in existing computer codes such as the widely used NASA code NEQAIR. Several modeling improvements are therefore proposed and included into NEQAIR. As a result, the enhanced version of the code is capable of predicting the radiative emission of air plasmas with better than 20% accuracy, as opposed to only orders of magnitude with the original version. Finally, the report presents first measurements of the radiative source strength of air for temperatures in the range between 5000 and 7500K. To our knowledge, these are the first measurements of this important property in this temperature range. Excellent agreement is again obtained with the predictions of the enhanced NEQAIR code.

DISTRIBUTION / AVAILABILITY OF ABSTRACT ☐ UNCLASSIFIED/UNLIMITED ☐ SAME AS RPT ☐ DTIC USERS	21. ABSTRACT SECURITY CLASSIFICATION **Unclassified**
NAME OF RESPONSIBLE INDIVIDUAL Spector	22b. TELEPHONE (Include Area Code) **202-767-5011** 22c. OFFICE SYMBOL **NE**

FORM 1473, 84 MAR 83 APR edition may be used until exhausted. All other editions are obsolete.

SECURITY CLASSIFICATION OF THIS PAGE
Unclassified

Table of Contents

Section		Page
1.0	INTRODUCTION	1-1
2.0	OPTICAL DIAGNOSTICS AND RADIATIVE EMISSION OF AIR PLASMAS.	2-1
3.0	PUBLICATIONS AND PRESENTATIONS	3-1
4.0	PERSONNEL	4-1

1.0 INTRODUCTION

This report is the final report on the research program on the fundamental processes in partially ionized plasmas conducted in the High Temperature Gasdynamics Laboratory at Stanford University. This research is supported by a grant from the Air Force Office of Scientific Research (AFOSR-88-0264) and is currently conducted under the direction of Professor Charles H. Kruger. Five graduate students have completed their Ph.D. under this program. Four of these currently have faculty positions at other universities.

Several space power and propulsion systems of potential long range interest to the Air Force involve partially ionized plasmas. Such systems include MPD thrusters, both open and closed cycle MHD power generation, high velocity reentry and thermionic energy conversion. Although the specific configurations, the exact operating conditions, and which of the competing systems will prove to be most useful in the long term remain to be established, it is important at this time to provide a broad fundamental research base in support of development activity. In particular, there are a number of key issues regarding the properties and discharge behavior of partially ionized plasmas and the interaction of discharges with fluid dynamics that need to be understood before the potential and limitations of competing systems can be fully evaluated. In addition, it is important that outstanding young applied scientists be educated in these areas.

Our research on partially ionized plasmas was initiated under grant AFOSR-83-0108 and focused on three major areas:

1. plasma properties,
2. discharge effects: plasma electrode interaction,
3. interaction of discharges and fluid dynamics.

Extensive reports on areas (2) and (3) have been given in previous Annual Scientific Reports and in the Final Report for grant AFOSR-83-0108. Recent research, under grant AFOSR-88-0264, has emphasized area (1), as does this report.

Results on air plasma properties are described in the following section. Publications and presentations resulting from this work are cited in Section 3 and Section 4 lists the personnel who have contributed to this report.

2.0 OPTICAL DIAGNOSTICS AND RADIATIVE EMISSION OF AIR PLASMAS

1. Summary and Overview

At high temperatures, air is a complex mixture of atoms, molecules and charged particles: commonly referred to as a plasma. The radiative properties of air plasmas are of primary interest in a wide range of applications, including chemical and material processing (plasma spray-coating), design of heat-shields for space vehicles (atmospheric re-entry, aeroassisted orbital transfer vehicles), and detection of missile signatures (SDI). Over the past three decades, space programs have stimulated intense research on air radiation, both experimentally (see for example Page and Arnold, 1964, Nerem, 1964, Schreiber et al., 1973, Ogurtsova et al., 1968, Devoto et al., 1978) and theoretically with the development of numerical codes (Kivel and Bailey, 1957, Meyerott et al., 1960, Breene et al., 1963, Allen, 1966, Whiting et al., 1969, Park, 1985a, 1985b). The projected manned missions to Mars have recently provided a new thrust for radiative studies as the Apollo-shaped vehicles, frequently considered for future atmospheric manned reentries, are expected to undergo 80% of the stagnation point peak heating from shock-layer radiation at the design re-entry velocity of 14 km/s (Tauber et al. 1992).

Air plasma modeling is a complex task that requires the understanding of fundamental molecular processes to predict the population of every rotational, vibrational and electronic level for each species present in the gas, along with emission intensities for transitions between these levels. Modeling can be separated into three modules:

- flow field module, to predict the chemical composition of the plasma.
- excitation module, to predict the electronic, vibrational, and rotational level populations.
- radiative module, to predict the intensity emitted by all possible radiative transitions.

Among the various codes, *NEQAIR* (Park, 1985a and 1985b) has been widely used because it includes both an excitation and a radiation module, and because these modules comprise most physical processes of importance. Moreover, *NEQAIR* has been the subject of ongoing development, including recent improvements in performance (speed increase achieved through optimization, vectorization, and restructuring of the code) and flexibility (Moreau et al., 1992).

While experimental data are necessary to assess the quality of the codes, they are often difficult and expensive to obtain. Nevertheless, in addition to the previously mentioned experiments and to those referenced by Park (1985a), spectral measurements have been recently conducted in shock tubes (Sharma et al., 1991a, Sharma and Gillespie, 1991b) and in the bow shock of ballistic missiles (Erdman et al., 1992). However, to numerically reproduce these experiments, the chemical composition and the various characteristic temperatures (translational,

rotational, vibrational, and electronic) of the plasma must be obtained from computations. It is not clear whether the observed discrepancies that may arise between the experiments and the computations are then due to errors in the flowfield computation, or in the excitation module, or in the radiative module. In order to check the validity of each module, a systematic approach is therefore essential. In particular, the radiative module must be thoroughly checked so that non-equilibrium experiments enable investigators to check the flowfield and excitation modules.

The work presented in this report has been mainly dedicated to providing a benchmark experiment to test the radiative module included in NEQAIR, and, based on these experimental results, to improving the radiative model. For clarity, the original code is termed NEQAIR-1, and the enhanced version, NEQAIR-2. The adopted strategy is presented in the following overview.

In Sections 2 and 3, the plasma torch facility and the experimental device used for the emission measurements are described in detail.

In Section 4, the thermodynamic state of the air plasma generated in the torch is investigated using emission measurements to determine electronic and rotational temperatures as well as electron number densities. The chemical composition is also studied by means of the kinetic code CHEMKIN with an extended thermodynamic data base to generate reverse reaction rates above 5,000 K. The results presented in this section show that the plasma is approximately in local thermodynamic equilibrium (LTE) over most of the plasma extent. An LTE temperature profile is measured to an accuracy of a few percent (typically less than 3%). This single profile fully characterizes the thermodynamic state of the plasma, and provides the input data to perform the numerical simulations of Section 5.

In Section 5, the focus turns to the testing of the radiative module of NEQAIR through a comparison between the experimental emission spectrum, measured and calibrated in intensity over the spectral range 2,000 to 8,000 Å, and numerical simulations using the NEQAIR code. The experimental spectrum, measured along a plasma diameter, includes contribution of regions at temperatures up to 7,500 K which is the temperature at the center of the axisymmetric plasma torch. This temperature range is very well suited to investigate the radiation of the major radiative bands of air plasmas. As will be seen in that section, the spectrum contains strong atomic and molecular features due to NO, N_2, N_2^+, CN, O_2, O, N, and C. Since the plasma composition and temperature are well known from the previous section, it is possible to simulate the spectrum numerically using the radiative module of NEQAIR. The comparison with the original version of NEQAIR revealed that some features of the code could be modified or enhanced. The revisions, detailed in the report, include a thorough update of molecular radiative transition probabilities and spectroscopic constants, and the addition of several NO band systems (NO Delta, Epsilon, Beta prime and Gamma prime). Since the C state from which the NO Delta

transition originates is predissociated, a simplified collision-predissociation model for this state has been added to the code. The effects of these changes are discussed, and a final comparison between the experimental spectrum and the results of the enhanced NEQAIR code is presented.

Finally, Section 6 presents measurements of the total radiative source strength of LTE air between 4000 and 7500 K. These results are then compared to the predictions of several codes, in particular the modified NEQAIR code.

2. Experimental facility: Plasma torch.

High temperature plasmas may be conveniently produced in arcs and torches. These various devices are described in details by Dresvin et al (1977), Davies and Simpson (1979), and Boulos et al (1985). Plasma torches offer advantages over arcs for they do not include electrodes, hence eliminating contamination problems. Induction plasma torches may produce either high or low enthalpy plasma flows. High enthalpy torches, which inherently operate at low efficiency, are suited for aerospace applications such as supersonic re-entry simulation (Leger et al., 1990). In contrast, low enthalpy torches such as the one available in our laboratory are typically designed for material and chemical processing (plasma spray-coating). Torches of the latter type achieve efficiencies on the order of 50% and produce relatively uniform enthalpy profiles at the nozzle exit.

Energy is coupled into the plasma by either an oscillating electric field (capacitive coupling) or an oscillating magnetic field (inductive coupling). The principles of inductive coupling are presented in Section 2.1 since the torch used in the present work is of that type. The characteristics of the actual torch are then presented in Section 2.2, and an estimate of the plasma properties in the induction region is given in Section 2.3.

2.1. Induction heating

The basic design for inductively coupled plasma (ICP) torches has not changed much since their first introduction by Reed (1961). Gas is injected at the bottom of a quartz tube surrounded by a coaxial induction coil traversed by a radio frequency current. The rf current produces an oscillating axial magnetic field that forces the free-electrons to spin in a radial plane and thereby generates eddy currents. The oscillating magnetic field induces an oscillating electric field, $\vec{E}(r)$, as may be seen from Maxwell's equation:

$$\vec{\nabla} \times \vec{E} = -\frac{\partial \vec{B}}{\partial t}. \tag{2.1}$$

Integrating over the area shown in Fig. 2.1, and using Stokes theorem,

$$\iint_A (\vec{\nabla} \times \vec{E}) \cdot \vec{n} dA = \oint_C \vec{E} \cdot d\vec{l} = \iint_A \frac{\partial \vec{B}}{\partial t} \cdot \vec{n} dA. \tag{2.2}$$

Since the electric field is tangential (Gauss' theorem), (2.2) reduces to

$$\pi(r+dr)\left[E_\theta + \frac{\partial E_\theta}{\partial r} dr\right] - \pi r E_\theta = -\frac{\partial B_z}{\partial t} \pi r dr. \tag{2.3}$$

and neglecting high order derivatives.

$$E_\theta + r\frac{\partial E_\theta}{\partial r} = -r\frac{\partial B_z}{\partial t}. \qquad (2.4)$$

This induced electromagnetic force accelerates the free electrons, thereby increasing their kinetic energy ε, or equivalently their translational temperature, $T_e = 2/3\ \varepsilon/k$. The free electrons then transfer their kinetic energy to heavy particles through collisions. When ionizing collisions produce enough electrons, the plasma becomes self-sustained.

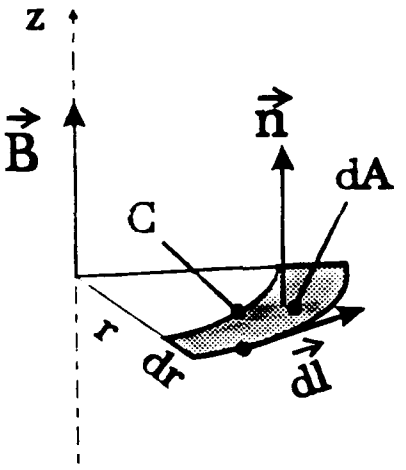

Figure 2.1. Area of integration.

If there were no plasma in the coil region, the magnetic field radial profile would be almost uniform (truly uniform for a coil of infinite length). However, when the plasma is present, the emf that acts on the eddy currents creates an adverse magnetic field (Lenz law) that increases in intensity towards the center of the torch and tends to cancel the driving B field. The plasma therefore shields electromagnetic waves and limits their penetration to the outer radial region of the discharge. This phenomenon was experimentally observed by Eckert (1971) as shown in Figure 2.2.

Freeman and Chase (1968) calculated the H-field distribution in the approximation of the so-called Channel model, and obtained the following expression at radius r:

$$H(r) = 2H_0\frac{ber(\sqrt{2}r/d) + j\,bei(\sqrt{2}r/d)}{ber(\sqrt{2}\rho) + j\,bei(\sqrt{2}\rho)} \qquad (2.5)$$

where *ber* and *bei* are the real and imaginary parts of the zero order Bessel function, H_0 the amplitude of the magnetic field, and ρ a reduced parameter. The so-called skin depth parameter d, defined as

$$d \equiv \sqrt{1/\pi \mu_0 \sigma f}\,, \tag{2.6}$$

characterizes the depth of penetration of the electromagnetic wave into the plasma.

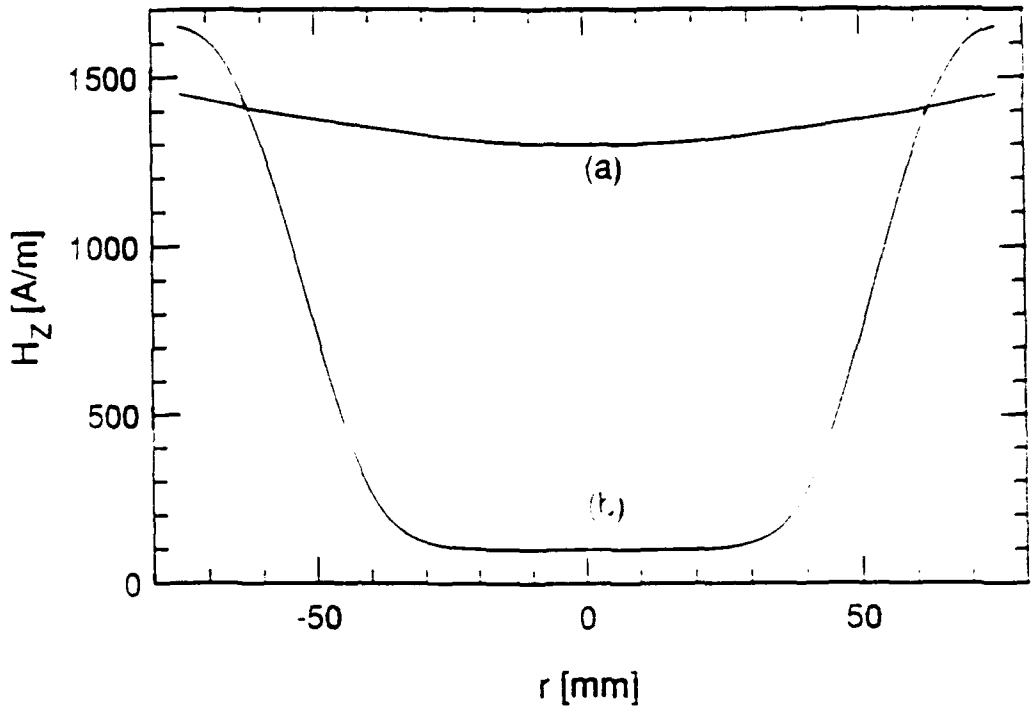

Figure 2.2. Radial profiles of the magnetic field intensity at the mid-section of the coil region, in the absence (a) and presence (b) of the discharge (after Eckert, 1971).

This parameter depends on the frequency f of the discharge and on the electrical conductivity σ of the gas. For an atmospheric pressure air plasma at an average temperature of 8,000 K, the electrical conductivity is σ=800 ohm^{-1}m^{-1} (Dresvin et al., p 42, 1977). At an operating frequency of 4 MHz, the skin depth can therefore be approximated by:

$$d \approx \left(4\pi^2 \times 10^{-7} \times 800 \times 4 \times 10^6\right)^{-0.5} \approx 9\ \text{mm}\,. \tag{2.7}$$

which shows that the electromagnetic field penetrates about a quarter of the way into our 70 mm diameter plasma torch. The inductive heating process therefore takes place primarily in an outer ring and the central part of the plasma is subsequently heated by convection and thermal conduction of heavy particles. This results in lower temperatures at the center of the discharge and in an M-shaped temperature profile in the coil region. The skin depth could be increased by decreasing the operating frequency, but this would also result in a decrease of the coupling efficiency which is determined by the coupling parameter $\kappa = \sqrt{2}\, r_0 / d$, where r_0 is the torch radius.

2.2. Description of the plasma torch

The device used in this work is a TAFA Model 66 inductively coupled plasma torch powered by a radio frequency LEPEL Model T-50-3 power supply operating at 4 MHz. This power supply can deliver up to 120 kVA of line power to the oscillator plates with a maximum of 12 kV DC and 7.5 A. The oscillator plates have in turn a maximum RF power output of 50 kW. The heat discharged into the torch and generator cooling system is measured by a combination of thermocouples at the inlet and outlet of the generator and turbine flowmeters in the flow lines. After subtracting the heat lost into the oscillator tube, this information is used to determine the power deposited into the plasma.

The torch schematic (Figure 2.3) shows the 5-turn copper induction coil (mean diameter 8.6 cm) encapsulated between a confinement tube (inner diameter 7.6 cm, thickness 3 mm) and a Teflon body. The confinement tube is made of quartz, a material that offers good thermal resistance and is relatively transparent to electromagnetic fields. The outer Teflon body acts as an electrical insulator and as an electromagnetic screen. The coil is cooled with de-ionized water to prevent arcing between its turns. Although water-cooling is technically more complicated to operate than air-cooling, a higher power operating range and thus higher heating of the gas is achieved.

The plasma torch can operate with a variety of gases (argon, air, hydrogen, nitrogen, methane, etc.) whose flowrates are monitored in an independent free standing panel. While the work reported here was done with air, argon was used during the torch starting phase, and hydrogen was added for electron number density measurements.

The gas is injected in axial, radial and swirl modes through the manifold located at the bottom of the torch. Axial injection provides bulk movement to the gas and is therefore useful when starting the torch. In normal operation, only swirl and radial injectors are used, in the ratio 1/3:2/3. Radial injection provides the desired axisymmetric pattern of gas flow. Swirl injection creates a cold gas sheath close to the quartz confinement tube to prevent overheating and to reduce heat losses to the cooling water. In addition, the swirl creates a low pressure zone in an annular shell that favorizes gas recirculation in the induction region and stabilizes the plasma. For this reason, such plasmas are called vortex-stabilized plasmas. The recirculation zone has been evidenced by several investigators, experimentally by Chase (1971) and Klubnikin (1975), and theoretically by Rhodes and Keefer (1989).

The water-cooled hollow probe at the center of the manifold is designed for powder or gas injection in commercial operation. In the present case, however it is only used when starting the torch to carry the free electrons generated outside the torch body by a high frequency tesla coil (Electro-Technic model BD-10-A). These free electrons are necessary to trigger the ionizing collisions that will finally provide enough electrons to sustain the plasma. In this starting phase,

argon is preferred over other gases because its low specific heat permits a rapid temperature increase leading to ionization, and because its low thermal conductivity prevents the hot zone from cooling by diffusion, which would result in thermal pinching. Once the argon plasma is established, the plate power is increased and air is progressively substituted to argon.

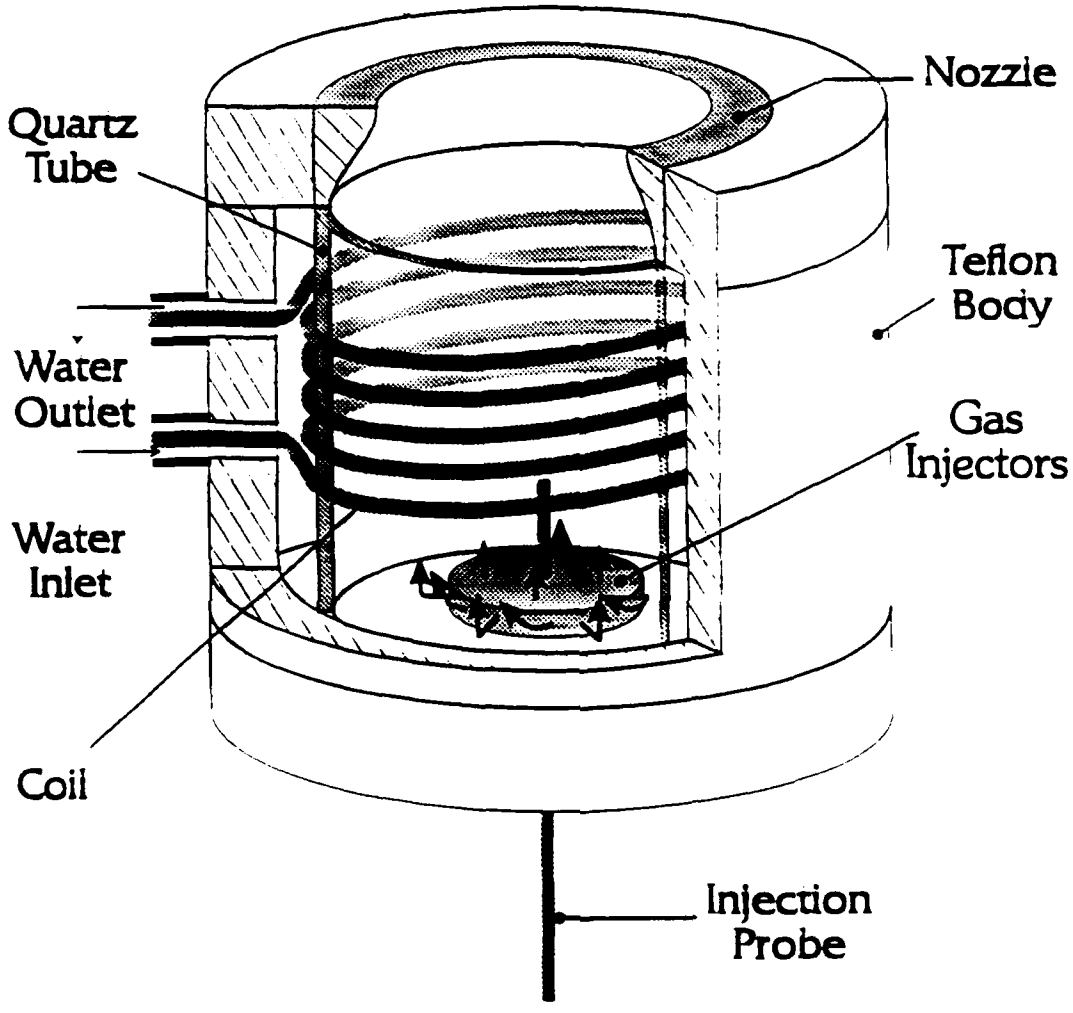

Figure 2.3. Plasma torch

The plasma then expands into ambient air through a converging copper nozzle. Different nozzle diameters from a few millimeters to 7 cm can be mounted on the torch: for the present work, a 5 cm nozzle was used.. All measurements presented in this report were conducted 1 cm downstream of the nozzle exit. In this radial plane, the maximum velocity is about 20 m/s and the maximum temperature is 7,500 K, corresponding to a density ρ of 2.7×10^{-2} kg.m^{-3} and a dynamic viscosity $\mu = 1.60\times10^{-4}$ kg.m^{-1}.s^{-1}. With these values, and based on a nozzle diameter of 5 cm, the

Reynolds number at the measurement point is about 170. The plasma jet is therefore laminar in the measurement region: it remains so downstream of the nozzle over a few centimeters, then turns into a bushy plume approximately 50 cm high.

2.3. Properties of the air plasma in the induction region

The induction zone could not be optically accessed here, and therefore no measurements were made in that region. However, an estimate of the plasma properties inside the coil region will be of importance, particularly in Section 4, when studying possible chemical non-equilibrium effects. Several authors have investigated the induction region, both theoretically and experimentally. We present below some of their observations and how they may be applied to the present torch.

As mentioned in the previous section, the center of the plasma in the induction region is expected to be colder than the annular shell into which most of the electromagnetic energy is coupled. The temperature difference between the coupling shell and the center depends on the type of gas, the skin depth, and the dimensions of the torch. This difference was however reported to be small, with a maximum of 1000 K in argon plasmas (Gol'dfarb and Dresvin, 1965), and a few hundred degrees for oxygen, nitrogen or air plasmas (Dresvin et al., p 194, 1972).

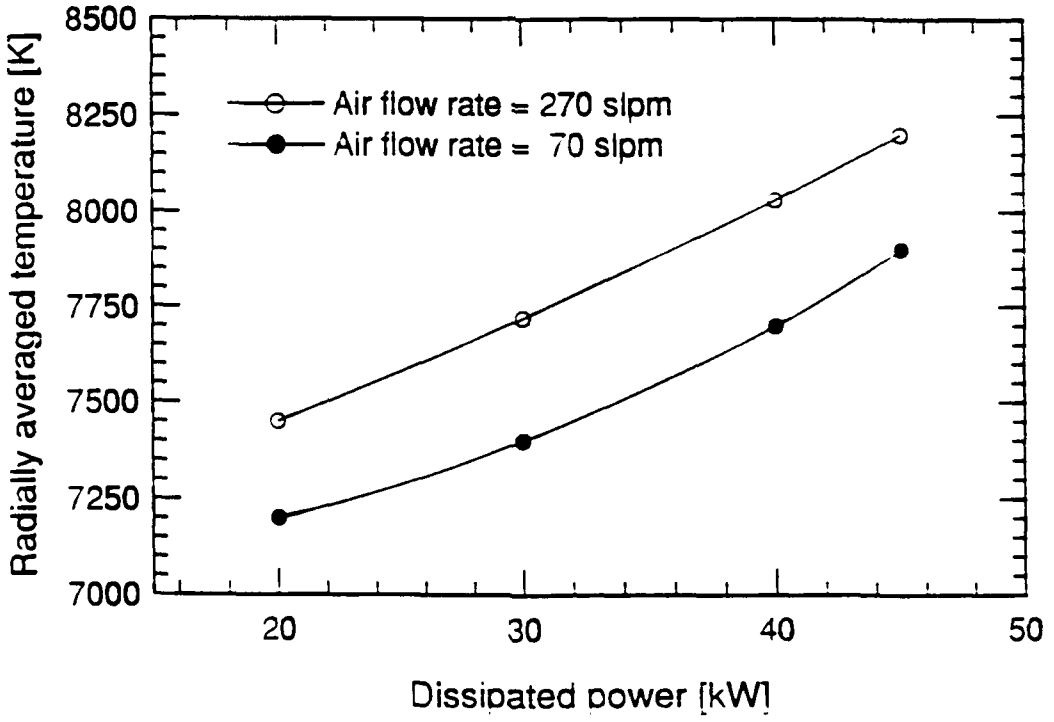

Figure 2.4. Radially averaged temperature as a function of dissipated power (Goykhman, 1970).

Temperature measurements were presented by Goykhman et al. (1970) for an air plasma produced by a torch similar to the present one: an inductive plasma torch, with a 60 mm diameter quartz tube, a 4-turn induction coil, and 50 kW nominal power. The 5.28 MHz generator frequency was slightly higher than in the present torch, but Dresvin et al. (1972) observed that, for argon plasmas at least, the maximum temperature in the coil region is independent of the operating frequency. Fig. 2.4 shows a plot of the temperature averaged over a plasma radius in the mid-section of the coil region as a function of the dissipated power and for two flow rate cases. Since our experiments were conducted at a flow rate of 95 slpm and a deposited power of about 27 kW, the average temperature in the induction region should not be above 8000 K, and taking into account the observations from the previous paragraph, 9,000 K is a conservative estimate for the maximum temperature in the induction region.

3. Experimental facility: Optical measurements.

3.1. Emission measurements

All measurements were conducted in a non-intrusive manner using optical diagnostics such as emission spectroscopy. This technique is not spatially resolved but since the plasma presents a high degree of axisymmetry, local values can be inferred from line-of-sight measurements along several chords of the plasma circular cross-section through the Abel-inversion. This mathematical transform imposes several constraints on the optical system design. First, measurements are required at several lateral locations, preferably every millimeter since the plasma has a 25 mm radius. Second, the probed volumes must be constant area cylinders. Finally, to allow for spatial resolution, the probed volume must be narrow, ideally pencil-like. The light is collected by a 50 cm focal length UV grade fused silica quartz lens placed at one focal length from the jet axis. It is coupled with a solid angle limiting iris of adjustable circular aperture to stop the beam down to anywhere above f 25, and is set on a stage with both lateral and axial translation capability. The collimated beam is then refocussed by a 15 cm focal length UV grade fused silica quartz lens onto the monochromator entrance aperture which acts as an area field stop. The corresponding system magnification is 0.3, which means that the imaged plasma area is 3.3 times the monochromator aperture area. With a typical setting of 2 mm for the gate height and 60 μm for the slit width, a spatial resolution of 0.2 mm laterally and 6.6 mm axially is achieved.

The light then goes through a Stanford Research System model SR540 optical chopper into a SPEX model 1400-11 3/4 meter scanning monochromator. The choice of lenses and stop fields ensures proper underfilling of the 7.5 entrance f number monochromator. The 1,200 lines/mm, 10× 10 cm grating is blazed at 3,000 Å. With the monochromator used in single pass, the linear dispersion varies between 11.1 Å/mm at 2,000 Å and 10.4 Å/mm at 8,000 Å. Both the entrance and exit slits are continuously adjustable from 20 μm to three millimeters. The dispersed light is then detected by a Hamamatsu model R1104 head-on photomultiplier tube with a high photocathode efficiency spatial uniformity and a broad quantum efficiency range as will be seen in Section 3.3. Data are acquired using a Stanford Research Systems model SR510 lock-in amplifier and then transferred via an RS232 line to a laboratory computer for analysis.

The set-up described above is adequately suited for emission measurements above 3,000 Å. Measurements in the ultra violet region between 2,000 and 3,000 Å are subject to specific problems that must be addressed by the choice of different optics. Chromatic aberration, while rather mild for most lens materials in the visible or the infra-red, increases dramatically below 2,500 Å as can be seen in Fig. 3.2. For measurements at a fixed wavelength, the problem can be circumvented by adjusting the lens position, but this solution is not practical for scans over large wavelength ranges.

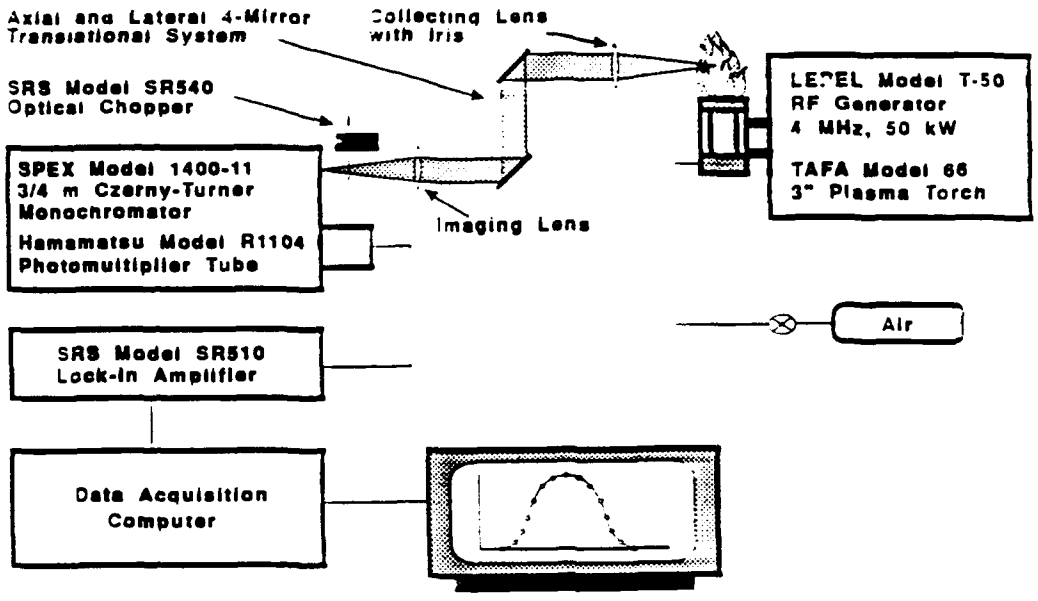

Figure 3.1. Experimental set-up for emission measurements.

Among the possible solutions are achromats, but they are difficult to build for wavelengths below 2,500 Å, or spherical mirrors in lieu of lenses, but this requires major changes in the optical system. A simple solution is to minimize the chromatic aberration by using a different lens material. Magnesium fluoride lenses offer a dramatic improvement other fused silica (Fig. 3.2) while still allowing for a broad spectral bandpass (Fig. 3.3).

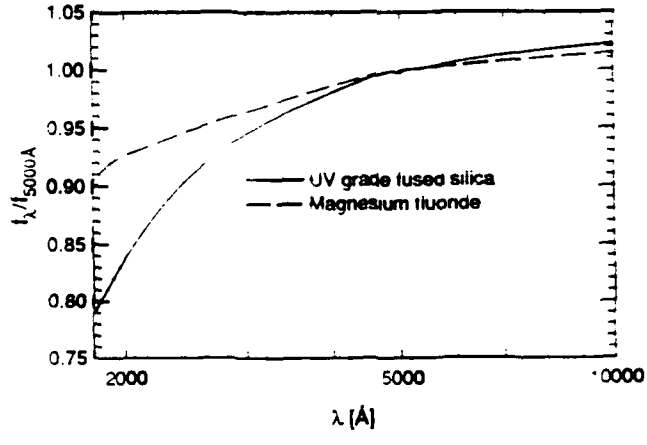

Fig. 3.2. Chromatic aberration of UV grade fused silica and magnesium fluoride.[1]

[1] The focal length of a lens varies with the refractive index which is itself a function of wavelength. The variations are very well approximated by the thin lens formula: $f_\lambda/f_{\lambda_0} = (n_{\lambda_0}-1)/(n_\lambda-1)$. Refractive indices for UV grade fused silica and magnesium fluoride are taken from Oriel, *Optics and Filters*, p12-5.

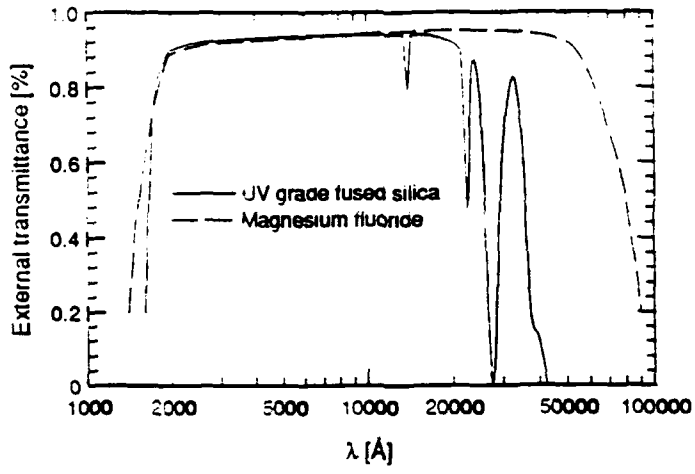

Fig. 3.3. Transmittivity of 10 mm thick fused silica and 3 mm thick magnesium fluoride windows.[2]

Another problem is linked to the use of the UV calibration source. The deuterium lamp, discussed in more details in section 3.3, has a very small circular emitting area of about one millimeter in diameter. To insure uniform illumination of the entrance slit, the magnification of the system has to be increased in order to at least double the image size. Since this increase is accompanied by a significant signal level reduction, a compromise must be reached. For these reasons, we replaced the collecting lens by a 50 cm magnesium fluoride lens, and the imaging one by a 100 cm focal length magnesium fluoride lens for all UV scans.

3.2. Radiation source strength measurements

Total radiation measurements are made with a Scientech model 36-0001 surface absorbing disk calorimeter. The detector spectral response is flat between 2,500 and 25,000 Å, and varies by about ± % between 2,000 and 2,500 A. Self-calibration is provided by an internal heater coil to an accuracy of about 3 %. Lateral measurements are performed every millimeter using a translational stage including a 25 cm focal length quartz lens used in 2f/2f, and a rectangular area stop yielding a spatial resolution of 1 mm laterally and 6.6 mm axially. The 6.6 mm height was so chosen as to provide the same axial spatial averaging as for temperature measurements.

Since the detector, the display meter, and the electrical connexions and cables are very sensitive to the RF noise generated by the plasma torch, all equipment is shielded by copper Faraday type cages. However, the shielding is not fully efficient in removing all the noise. A simple solution was found with the introduction of a low-pass electrical filter between the analog display recorder and the digital conversion port of the lock-in amplifier. With a frequency cut-off at 40 Hz, all 60 Hz and

[2] Oriel, *Optics and Filters*, p 12-7, 8.

high frequency noise are eliminated and the drift rate that would otherwise be sometimes comparable, over several minutes, to the magnitude of the measured signal, is cut down to less than a percent of the measured signal. This improvement is particularly important as the slow 3 s response time of the detector causes long measurement times.

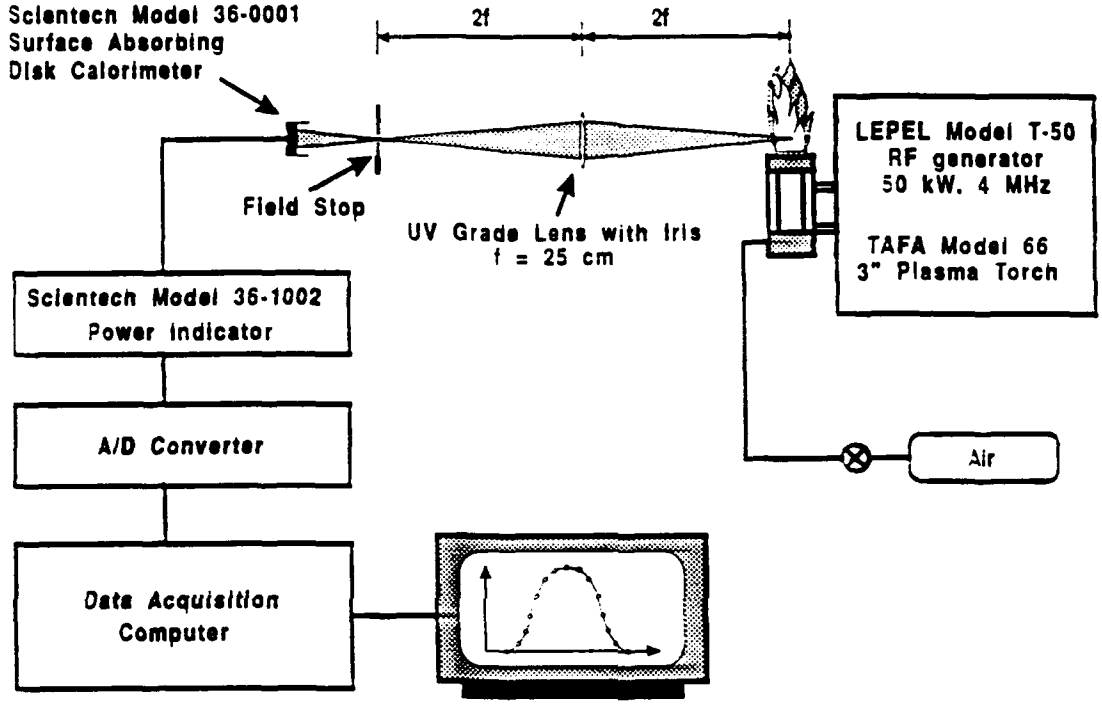

Figure 3.4. Experimental set-up for radiation source strength measurements.

3.3. Calibration

Spectroscopic temperature measurements require the knowledge of either the relative or the absolute intensity of spectral features. The measured emission spectra need also to be corrected for the spectral response of the detection system which includes lenses, mirrors, monochromator and photomultiplier tube. The detection system had therefore to be calibrated in intensity between 2.000 and 8.000 Å. To cover this broad spectral range with maximum accuracy, the combination of a deuterium lamp and a quartz halogen lamp was used. Deuterium lamps cover the ultraviolet range 2.000 to 4.000 Å and have their maximum spectral radiance around 2.000 Å (see Fig. 3.5). Tungsten lamps cover the rest of the range from 2.500 Å and above with maximum spectral radiance at long wavelengths (see also Fig. 3.5). The overlapping region from 2.500 to 4.000 Å provides a check for the quality of the calibration.

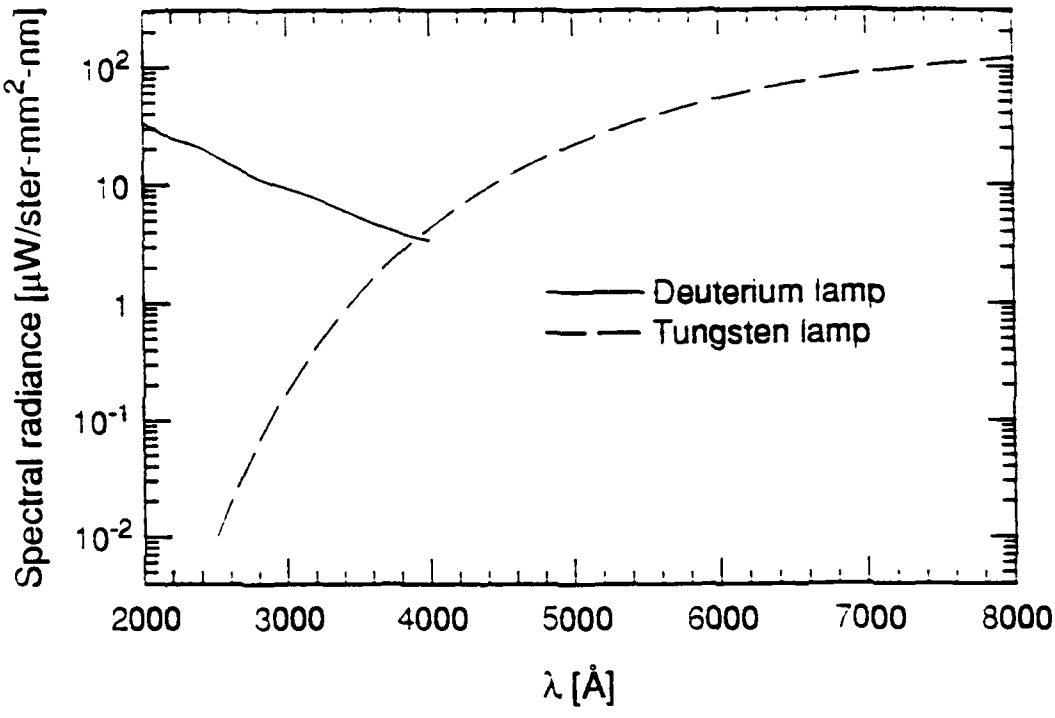

Figure 3.5. Spectral radiance of the Optronic tungsten and deuterium standards.

Both lamps used in this work are standards of spectral radiance with calibrations traceable to the National Institute of Standards and Technology (NIST) standards. The Optronic model UV-40IR lamp consists of a 40 Watt deuterium lamp with a ultraviolet transmitting suprasil window. It is calibrated in intervals of 100 Å from 2,000 to 4,000 Å with an uncertainty less than 10%. The Optronic model 550A lamp is a modified GE-18A/T10/2P tungsten ribbon-filament placed behind a sapphire window for optimum ultraviolet transmission. It is calibrated from 2,500 to 8,000 Å in intervals of 100 Å and has a quoted uncertainty of less than 3%.

The relative spectral response of the detection system (optical train with MgF_2 lenses, monochromator, and PMT) is presented in Fig. 3.6 where the plotted curve represents the normalized measured output signal in volts per unit emitted power. Note the excellent agreement between the two lamps in the overlapping region 3,000-4,000 Å.

The spectral response fall-off at the 2,000 Å end is due to the photocathode quantum efficiency decrease, to the decreasing transmittivity of the two lenses, and, mainly, to the poor reflectivity of the six aluminum silicon monoxide mirrors; at longer wavelengths, the decrease is principally caused by the poorer quantum efficiency of the photocathode (Fig. 3.7). The two peaks around 5100 Å and 6300 Å may be attributed to the different spectral response of the grating to the parallely and perpendicularly polarized components of the light.

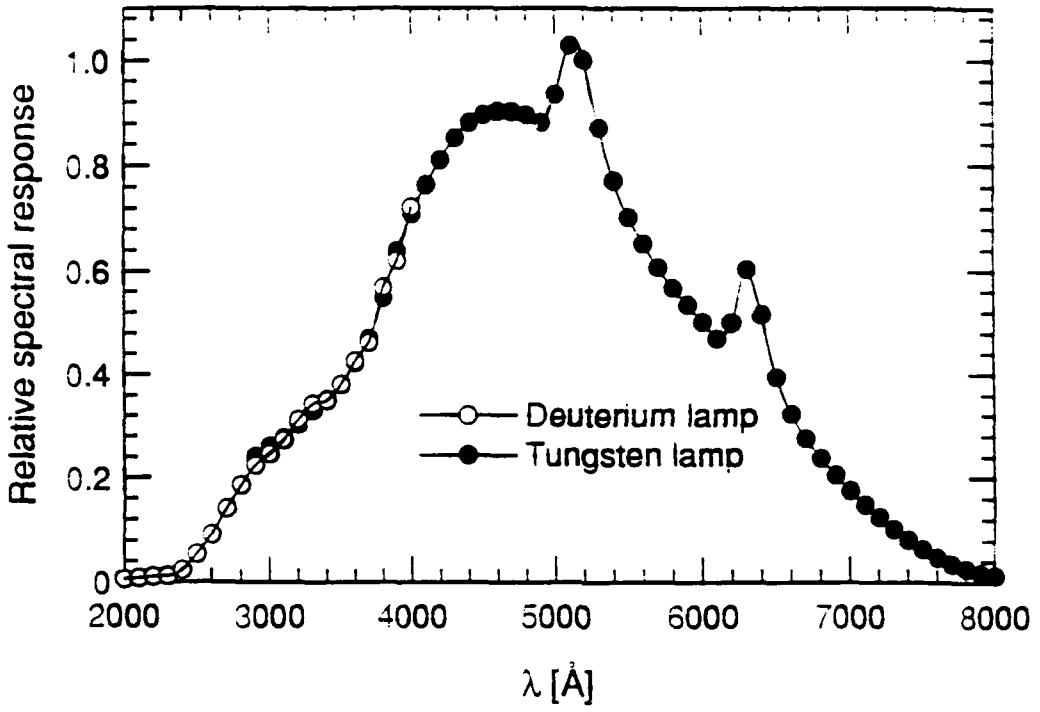

Figure 3.6. Relative spectral response (Volt/Watt) of the detection system including 2 magnesium fluoride lenses, 4 mirrors, monochromator and photomultiplier tube. The curve is normalized by the value at 5100 Å.

As the standards of spectral radiance are calibrated for only 20 hours of use, it is advantageous to substitute non-calibrated tungsten ribbon lamps such as the GE-18A/T10/1 projection lamps for measurements above 3,500 Å. In this case, the ribbon temperature is measured using a Pyro-Micro disappearing filament, single color pyrometer, and corrected for tungsten emissivity by an iterative procedure. The emissivity of tungsten as a function of temperature and of wavelength was measured by several investigators, in particular Larrabee (1959) who also provided curve fits between 1600 and 2400 K for wavelengths between 3,500 and 8,000 Å. When performed with this latter method, the relative calibration of the detection system above 3,500 Å is found to be in excellent agreement with the one obtained with the standard of spectral radiance. For absolute calibrations, discrepancies do not exceed 10%.

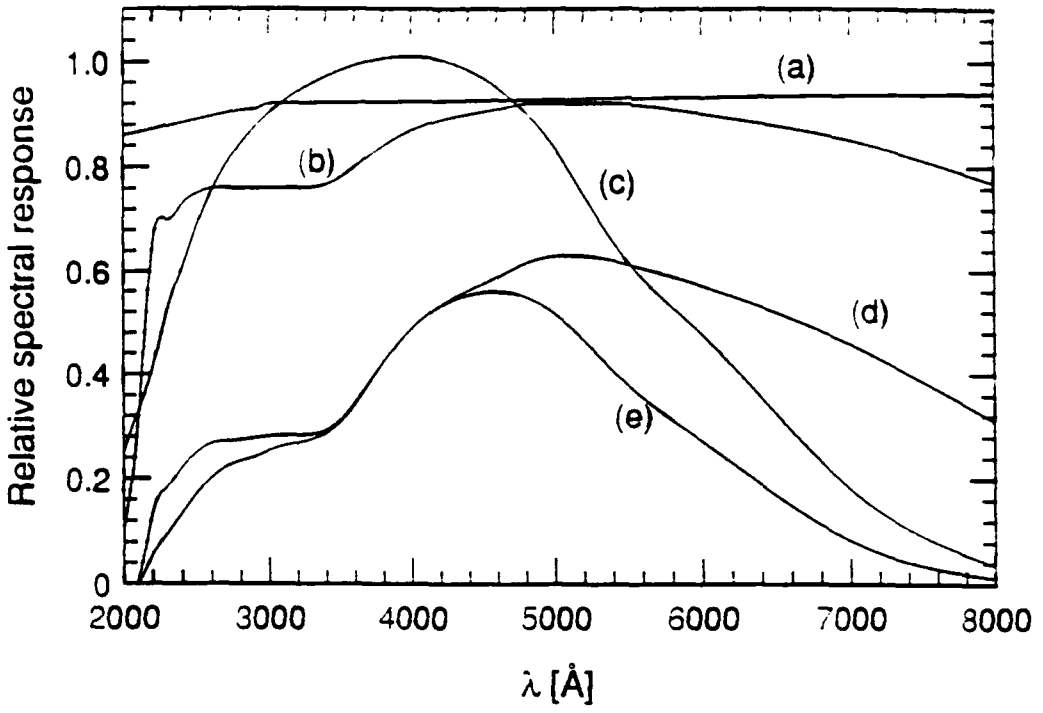

Figure 3.7. **Relative spectral response of the individual components of the detection system.**
(a) External transmittivity of one magnesium fluoride lens.[3]
(b) Reflectance of one Al(SiO) mirror.[4]
(c) Radiant sensitivity of the R1104 photomultiplier tube.[5]
(d) All 4 mirrors and 2 lenses included in the optical train.
(e) Complete detection system: 4 mirrors, 2 lenses, and PMT.

---

[3] Oriel Corporation, *Optics and Filters*, p 12-8

[4] Oriel Corporation, *Optics and Filters*, p 5-2

[5] Hamamatsu, *Photomultiplier Tubes*

4. Thermodynamic state of the plasma.

4.1. Equilibrium

Thermodynamic characterization of a plasma involves the determination of the number density of the various species present in the plasma —atoms, molecules, ions, and electrons, and of the distribution of particles among the available quantum energy states.

In the limiting case of a plasma in Complete Thermodynamic Equilibrium (CTE), all microscopic processes affecting the distribution of the species are in detailed balance. In that case, all plasma particles have a Maxwellian velocity distribution characterized by a common temperature T, and radiative emission is described by the Planck blackbody function at the same temperature T. The thermodynamic state of the plasma is then completely determined by two parameters, the temperature T and the pressure. With the notable exception of the solar plasma below the photosphere, such a situation is not encountered in common man-made plasmas the dimensions of which being too small to prevent radiation escape.

The other limiting case is one where the population distribution over energy states cannot be described by a simple distribution such as the Boltzmann distribution. Instead, each level needs to be determined individually which is practically impossible considering that the number of available energy states is infinite.

Many common applications however fall in between these two extreme cases and a more complete discussion can be found in Mitchner and Kruger (1973) or Biberman et al (1987). For atmospheric pressure plasmas such as the one studied in this work, the frequency of collisions between particles is high enough for the free electrons to transfer their kinetic energy to heavy species efficiently. Such a plasma is referred to as a thermal plasma, and the kinetic temperature of the free-electrons is close to the kinetic temperature of the heavy species, at least in the current-free region downstream of the RF coil where the measurements are conducted. Moreover, since the spacing between adjacent rotational levels is small in comparison to the average kinetic energy associated with translational motion, and since the energy exchange between translational and rotational motion occurs very rapidly, molecules tend to follow an equilibrium distribution over the rotational levels. The characteristic temperature of the distribution, termed T_r, is close to the kinetic (translational) temperature T of the gas.

For vibrational levels, the situation is different in that the vibrational energy spacing tends to exceed the translational energy of heavy particles, and the period of molecular vibrations is short compared to the interaction time between colliding particles. As a result, vibrational-translational (V-T) energy exchange is hindered at least for the lowest vibrational levels (for higher levels, the period of molecular vibrations increases and the V-T exchange increases significantly). Collisions

with free electrons, on the other hand, are much more efficient, and electronic-vibrational energy exchange tends to be much more important than V-T exchange. In addition, vibrational-vibrational energy exchange is also very efficient. As a result, the vibrational energy levels tend to follow a quasi equilibrium distribution, but at a characteristic temperature T_v close to the free electron temperature T_e. Such a distribution (Treanor distribution) holds in practice for the lowest vibrational levels only since for higher lying levels the rate of V-T exchange dominates, and therefore the higher levels tend to be closer to an equilibrium distribution at the temperature of the heavy particles. As will be seen in Section 5, however, only a few vibrational levels are significatly populated (typically up to v'=4) under our experimental conditions and therfore the vibrational distribution should be closer to the free electron temperature.

The population of the electronic levels is governed by collisions with free electrons, and by several phenomena such as radiation escape and predissociation that cause a depletion of these levels. Radiation escape arises when the plasma extent is finite: in that case, the radiative field is no longer blackbody at all wavelengths. Predissociation is a molecular process by which the molecule undergoes spontaneous (and non-radiative) dissociation because of a crossing with another potential curve. At relatively high pressure, and atmospheric pressure in particular, the rates of collisional excitation and deexcitation by electron impact tend to be much higher than the depleting radiative and predissociation rates (with the notable exception of the electronic C state of NO as will be seen in Section 5). As a result, the electronic levels tend to follow a Boltzmann distribution at the temperature of the free electrons. The situation is however complicated in such situations as ionizing or recombining plasmas. Since high lying bound electrons undergo little influence from the nucleus, they tend to behave in the same way as free-electrons. Therefore these high lying levels tend to be in Saha equilibrium with the free electrons at the temperature of the free electrons but not inequilibrium with the ground state. Under ionizing conditions, free electrons are produced whereas in recombining plasmas they undergo depletion through ion recombination processes. Since ionization and recombination rates are finite, a defect or an excess of free electrons can appear because of inefficient communication between the low and high lying bound electronic energy levels. In the case of a recombining plasma, overpopulated high-lying electronic levels can be caused by the limited rate at which these high-lying levels cascade down to lower levels (see for example Owano et al., 1990, Gordon, 1992). Situations such as those depicted in Figure 4.1 may occur. Only in the particular case where the bound electrons follow a Bolztmann distribution can the concept of the electronic temperature, T_{el}, be introduced.

Thermal equilibrium will be achieved if all energy levels can be described by a common temperature T. If, in addition, the various species present in the plasma are in chemical equilibrium, the plasma is completely characterized by two parameters, the temperature T and the

pressure. The situation is analogous to the case of CTE, except that the concept now applies only locally, and only to the species distribution, not the radiative field. This case is commonly referred to as Local Thermodynamic equilibrium (LTE).

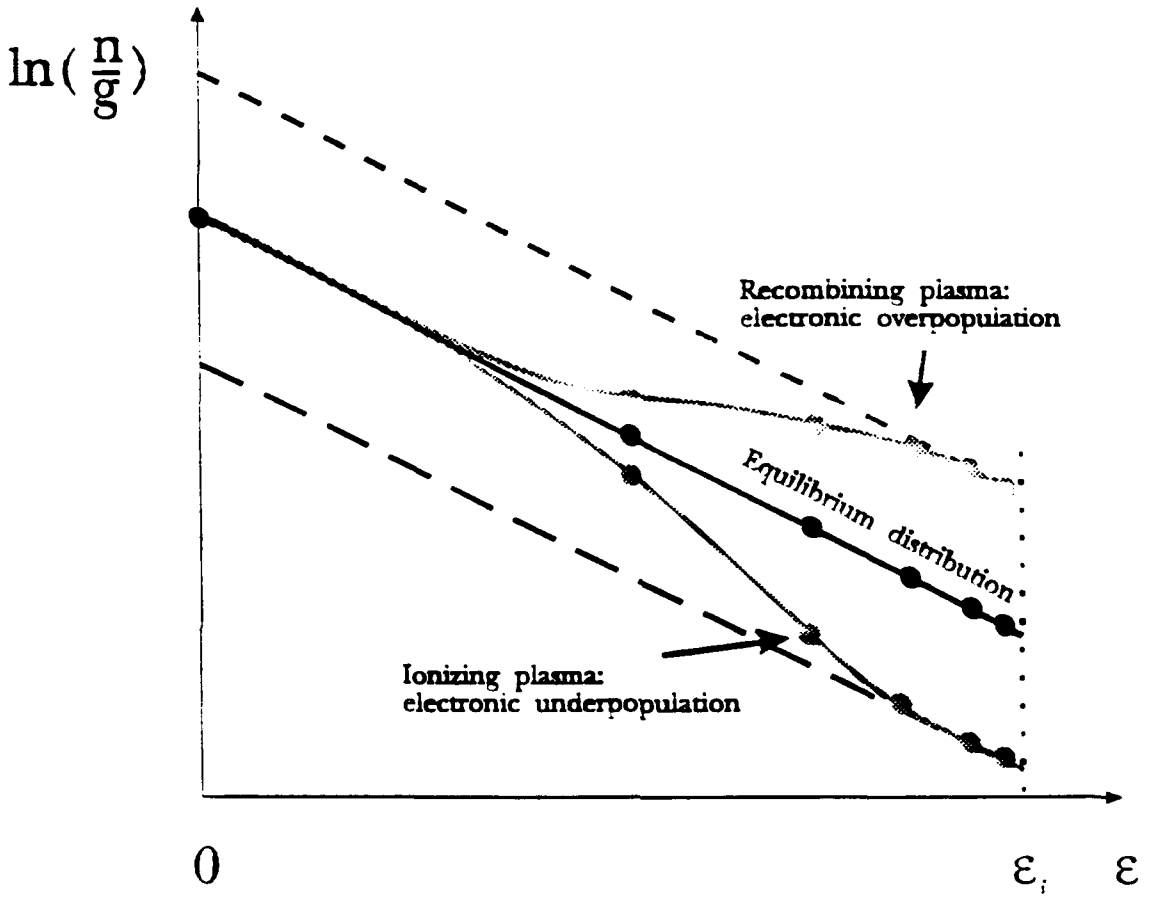

Figure 4.1. Electronic population distributions in equilibrium, ionizing, and recombining plasmas.

4.2. Thermal equilibrium

4.2.1. Electronic temperatures. Population distribution of the electronic levels.

In a plasma in Local Thermodynamic Equilibrium (LTE), the distribution of electronic levels follows a Boltzmann statistic characterized by a single temperature T. The population of any given electronic level i, with energy ε_i and degeneracy g_i, is related to the ground level population n_0 of degeneracy g_0 by:

$$\frac{n_i}{g_i} = \frac{n_0}{g_0} \exp\left(-\frac{\varepsilon_i}{kT}\right). \qquad (4.1)$$

Taking the logarithm, Eq. 4.1 becomes:

$$\ln\left(\frac{n_i}{g_i}\right) = \ln\left(\frac{n_0}{g_0}\right) - \frac{\varepsilon_i}{kT}. \qquad (4.2)$$

A plot of $\ln(n_i/g_i)$ versus ε_i (Boltzmann plot) therefore yields a straight line of slope -1/kT from which the characteristic temperature of the distribution can be readily inferred.

However, as stated earlier, this ideal situation does not always hold. In argon plasmas for instance, the upper electronic levels may be overpopulated with respect to the equilibrium distribution when the electron number density is itself elevated (Gordon, 1992). More generally, departures from LTE occur in ionizing or recombining plasmas. In our case, the air plasma ionizes within the coil region and recombines as it cools after leaving the induction zone. Since all our measurements are conducted one centimeter downstream of the nozzle exit, we are mainly concerned with recombination effects.

When the plasma cools, the free electrons tend to recombine with the ions, but since recombination rates are finite the process is not instantaneous and an excess of free electrons may appear. The outer bound electrons, which undergo little influence from the nucleus and thus behave similarly to the free electrons, also see their density increase. If they cannot "cascade" down fast enough into the lower levels of the particle, the high- lying electronic levels become overpopulated, and the population distribution is no longer Boltzmannian.

In order to investigate a possible departure from equilibrium in the electronic levels, two approaches can be followed. A first method (Sections 4.2.1.a and 4.2.1.b) consists in measuring the number densities of several electronic levels to determine whether they follow a Boltzmann distribution. As mentioned earlier, departure from a Boltzmann distribution could be caused by an elevated free-electron number density. The second method (Section 4.2.1.c) therefore consists in measuring the free electron number density and comparing it to equilibrium predictions.

4.2.1.a LTE Temperature

The LTE temperature is defined from the Boltzmann relation between an excited electronic level and the electronic ground state of the particle:

$$\frac{n_i}{g_i} = \frac{n_0}{g_0} \exp\left(-\frac{\varepsilon_i}{kT_{LTE}}\right). \qquad (4.3)$$

Graphically, it is obtained on a Boltzmann plot from the slope of the line joining the ground state

to the electronic level under consideration. For a plasma in LTE this temperature is level-independent because all levels lie on a straight line. Therefore, if the plasma is in LTE, the LTE temperature does represent the electronic level distribution. On the other hand, if the electronic levels do not follow a Boltzmann distribution with respect to the ground state, every probed level yields a different LTE temperature. In this case, the different LTE temperatures have no physical meaning; they only indicate a non-Boltzmann distribution.

The number density of an excited state can be accessed by emission spectroscopy by probing the radiative transitions issued from that state. Transitions from atomic electronic levels produce a single spectral line that spans a narrow spectral range, typically a few angstroms. Atomic transitions are therefore more easily accessed than molecular transitions that span very large spectral ranges, typically several thousand angstroms. For this reason, electronic temperatures are determined in the present work from atomic transitions only. Not all atomic transitions can be probed however: they have to lie in a wavelength range adequate for the detection system and they must be easily differentiable against the underlying background due to continuum, molecular bands, or second order light. These restrictions led to the selection of the five atomic transitions whose characteristics are summarized in Table 4.1.

Atom	ε_l (cm^{-1})	g_l	ε_u (cm^{-1})	g_u	λ (Å)	A_{ul} (10^7 sec^{-1})	f_{lu}	Accuracy
Oxygen	73768	5	86629	15	7773.4	3.40	0.922	10%
Oxygen	86629	15	102865	25	6157.3	0.701	0.0664	10%
Nitrogen	83366	6	96752	4	7468.31	1.61	0.089	25%
Nitrogen	83319	4	96752	4	7442.30	1.06	0.088	25%
Nitrogen	83286	2	96752	4	7423.64	0.52	0.086	25%

Table 4.1. Electronic transitions considered in the present study (Wiese et al. 1966).

The total intensity I of a spectral line is related to the number density of a transition's upper state (emitting level) n_u by:

$$I\left[\frac{\text{Watt}}{\text{cm}^2-\text{sr}}\right] = n_u \frac{A_{ul}}{4\pi}(\varepsilon_u - \varepsilon_l) \qquad (4.4)$$

where the Einstein coefficient A_{ul} and the upper and lower energies ε_u and ε_l are the constants indicated in Table 4.1.

The procedure for determining total line intensities is as follows. First the monochromator is tuned to the wavelength of the transition under consideration. In our case, the monochromator entrance and exit slits were set to 40 and 1,000 µm respectively, which correspond to spectral widths of 0.44 and 11 Å, respectively. The large exit slit width is necessary to minimize line-wing

cut-off and to capture over 99% of the line energy (see for instance Owano, 1991a p101). It also enables to encompass the oxygen line at 7773.4 Å which is in fact a triplet spread over 3.44 Å. The total intensity emitted by the plasma is then measured every millimeter along plasma chords, and a typical lateral intensity profile is presented in Figure 4.2. The monochromator is then detuned by a few angstroms to a region free of lines where the measured signal corresponds to background, continuum, or second order light. Subtracting this signal from the total intensity produces a lateral profile of line intensity only.

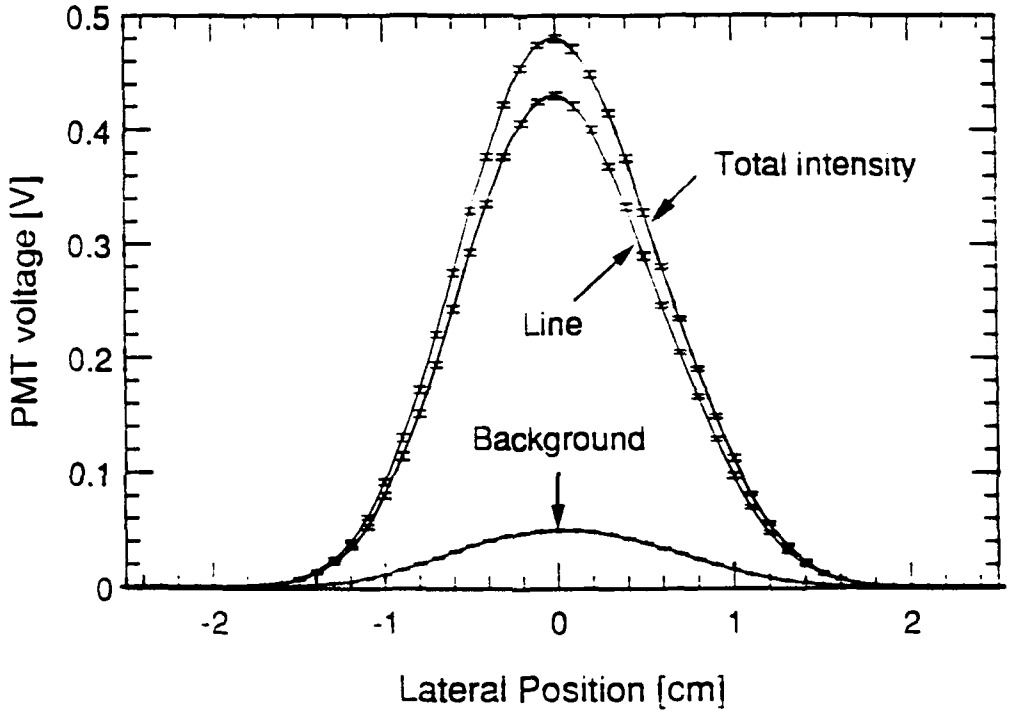

Figure 4.2. Lateral emission profile of the oxygen line at 7.773 A

This profile, in unit of volts, corresponds to the line intensity averaged along plasma chords. It is converted to radial variations using a mathematical treatment known as the Abel-inversion, for which a detailed account can be found in Appendix 1. At this stage, the units become volt/m. Conversion into radiance units is obtained by intensity calibration using the tungsten lamp described in Chapter 3. To this end, the calibrated lamp is placed at the focal point of the detecting lens with the same wavelength, slit settings, and PMT voltage as for line intensity measurements. The procedure yields a calibration factor, in Volt/(Watt/cm^2/sr), that is used to transform the radial intensity profile into the desired radiance units of Watt/cm^3/sr. The number density of the emitting state is then readily obtained from Eq. 4.4.

The remaining parameter needed to calculate an LTE temperature profile from Eq. 4.3 is the

number density of the ground state. This parameter cannot be measured by emission spectroscopy—the ground state does not emit radiation, nor by absorption spectroscopy—the corresponding electronic transitions are in vacuum ultraviolet. However, a measurement is not needed since the ground state number density is related to the total number density n_s of the species s (oxygen or nitrogen here) by the following relation:

$$\frac{n_0}{g_0} = \frac{n_s(T_{LTE})}{Q_{el}(T_{LTE})} \tag{4.5}$$

where Q_{el} stands for the electronic partition function of the atom s. Introducing X_s, the mole fraction of species s, and using the LTE assumption,

$$n_s = X_s(T_{LTE})\frac{P}{kT_{LTE}}. \tag{4.6}$$

Substituting Eqs. 4.5 and 4.6 into Eq. 4.3:

$$\frac{n_u}{g_u} = X_s(T_{LTE})\frac{P}{kT_{LTE}}\frac{1}{Q_{el}(T_{LTE})}\exp\left(-\frac{\varepsilon_u}{kT_{LTE}}\right). \tag{4.7}$$

Eq. 4.7 is an implicit equation from which T_{LTE} can be obtained by iteration. Since the mole fraction of atomic oxygen or nitrogen varies relatively slowly in the temperature range of interest here (see Fig. 4.3), the behavior of Eq. 4.7 is mainly controlled by the exponential term, and therefore convergence is reached in a few iterations, typically less than five.

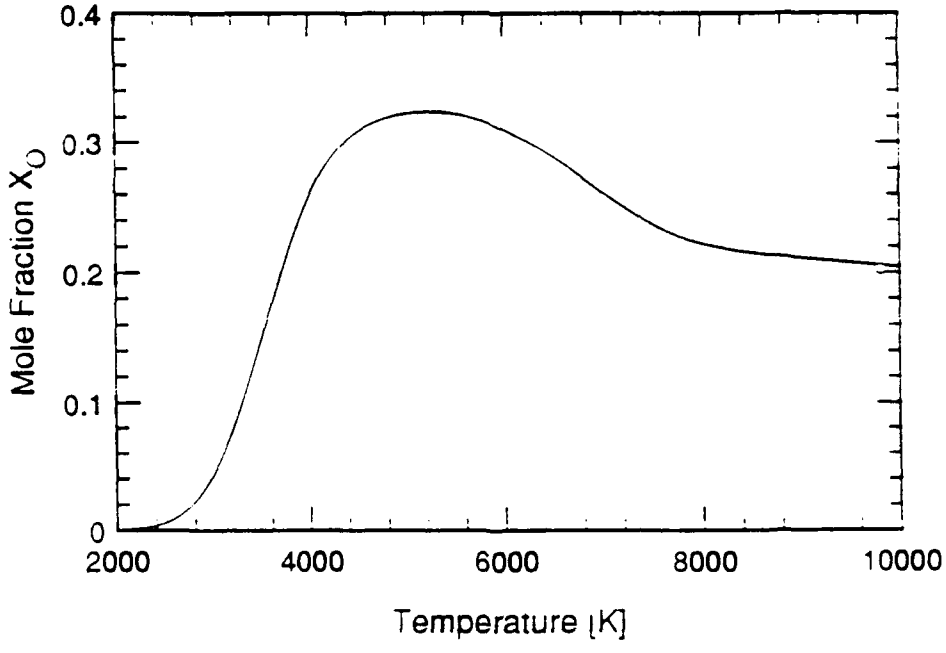

Figure 4.3. Atomic oxygen mole fraction in chemical equilibrium air.

The five radial LTE temperature profiles thus determined are presented in Fig. 4.4. Each curve has been truncated at the radial position beyond which the measured PMT signal drops below the detection limit. The very good agreement between the five temperature profiles evidences the equilibrium distribution of the electronic levels. However, an uncertainty analysis and an estimate of the effects of line self-absorption are warranted to establish the validity of the temperature profiles as accurate descriptions of electronic level distribution.

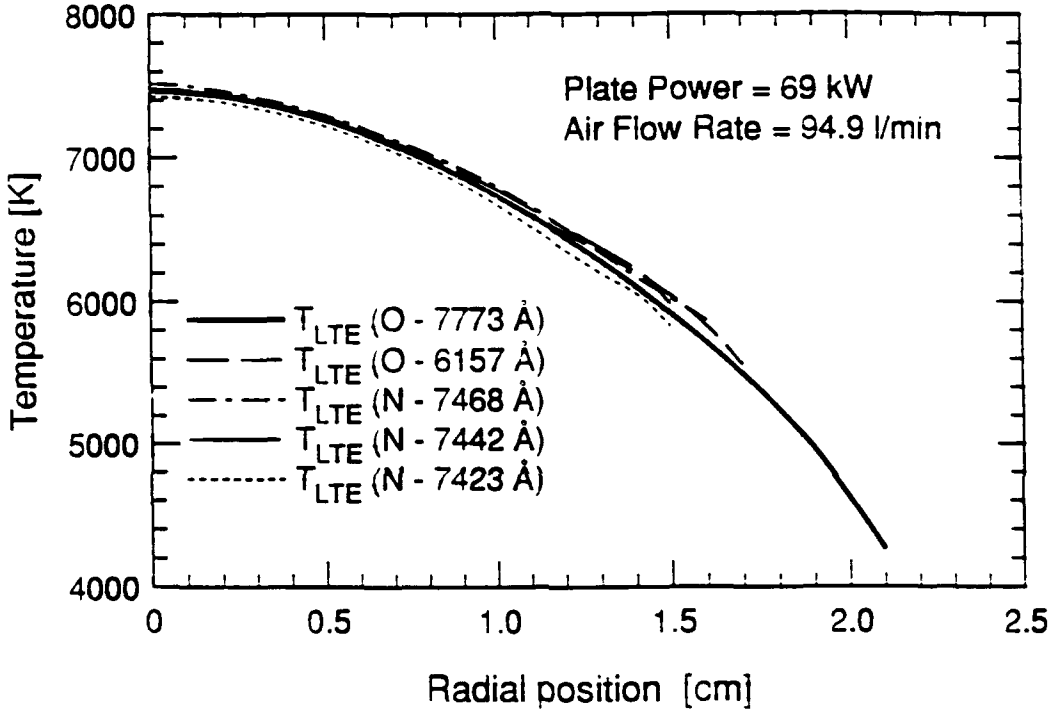

Figure 4.4. LTE temperature profiles.

Uncertainty analysis

Special attention was paid to determine the error bars on the temperature profiles. For that purpose, a computer program was written to simultaneously perform the data reduction and an uncertainty analysis that accounts for the standard deviation on the measurements, the uncertainty propagated by the fitting and the Abel-inversion procedures, the uncertainty on the absolute calibration (typically 5%), and the uncertainty on the Einstein coefficients (see Table 4.1). The error bars thus determined are presented in Figure 4.5 for the five atomic lines.

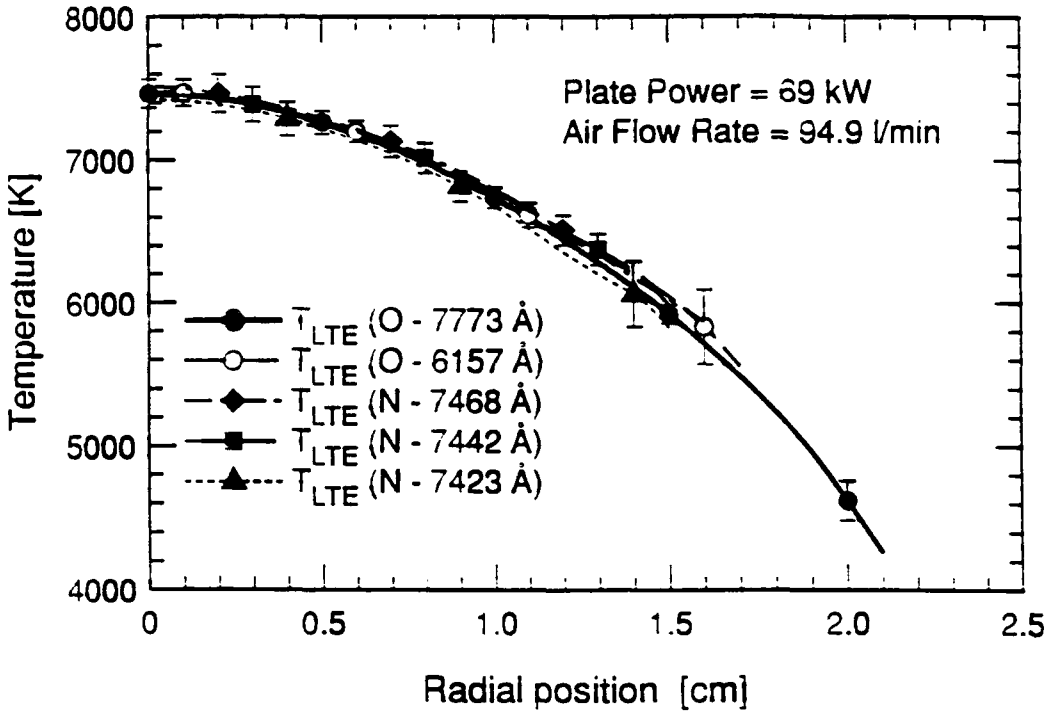

Figure 4.5. Uncertainties on the LTE temperature profiles.

These error bars, which are typically on the order of 100 K or 1.5%, may appear at first sight surprisingly small. The following simple analysis, however, should shed some light on the reasons for such small uncertainties.

Taking the logarithm of Eq. 4.7 and differentiating, we obtain:

$$\left|\frac{\Delta(n_u/g_u)}{n_u/g_u}\right| = \left|\frac{\Delta X_s}{X_s}\right| + \left|\frac{\Delta T_{LTE}}{T_{LTE}}\right| + \left|\frac{\Delta Q_{el}}{Q_{el}}\right| + \frac{\varepsilon_u}{kT_{LTE}}\left|\frac{\Delta T_{LTE}}{T_{LTE}}\right| \tag{4.8}$$

The electronic partition functions of atomic oxygen and nitrogen, respectively equal to

$$Q_{el}^{O} = 5 + 3e^{-228/T} + e^{-326/T} + O(e^{-23.000/T}), \tag{4.9}$$

and

$$Q_{el}^{N} = 4 + O(e^{-28.000/T}), \tag{4.10}$$

are practically constant over the temperature range of this study and can be considered equal to 9 and 4, respectively, with better than 1% accuracy up to 10,000 K. Also, as may be seen from Fig. 4.3, the oxygen and nitrogen mole fractions vary slowly with temperature. Hence, neglecting $|\Delta X_s / X_s|$ and $|\Delta Q_{el} / Q_{el}|$:

$$\left|\frac{\Delta T_{LTE}}{T_{LTE}}\right| \cong \frac{1}{\left|\frac{\varepsilon_u}{kT_{LTE}}+1\right|}\left|\frac{\Delta(n_u/g_u)}{n_u/g_u}\right|. \tag{4.11}$$

Considering for instance the oxygen line at 7,773 Å, the uncertainty at an average temperature of 7,000 K is therefore given by:

$$\left|\frac{\Delta T_{LTE}}{T_{LTE}}\right| \cong \frac{1}{17.8+1}\left|\frac{\Delta(n_u/g_u)}{n_u/g_u}\right| \cong 0.05\left|\frac{\Delta(n_u/g_u)}{n_u/g_u}\right| \tag{4.12}$$

Consequently, at 7,000 K, it is sufficient to know n_u within 30% accuracy to obtain no more than 1.5% (or 100 K) uncertainty on the LTE temperature. At this rate, a difference of several hundred degrees between the different LTE temperatures would mean a non-Boltzmannian distribution. This is not the case however for any of the five temperature profiles since they are typically within a few ten degrees of each other.

Line self-absorption

As it crosses its way out of the plasma, the light emitted inside the plasma undergoes some absorption. Since the absorption coefficient is proportional to the line oscillator strength or equivalently to the Einstein coefficient,[1] the values listed in Table 4.1 suggest that the oxygen line at 7,773 Å is subject to the most intense self-absorption of the 5 lines. For a plasma in LTE, the spectral absorption coefficient has the following expression:

$$\kappa(\lambda) = \frac{\pi e^2}{m_e c} n_l f_{lu}\left[1-\exp\left(-\frac{\varepsilon_{ul}}{kT_{LTE}}\right)\right]\Phi(\lambda), \tag{4.13}$$

where n_l is the number density of the lower level of the transition, f_{lu} the electronic oscillator strength, and $\Phi(\lambda)$ the line shape factor that includes Doppler, natural, Stark, van der Waals, and resonance broadening mechanisms. While Doppler broadening results in a Gaussian lineshape:

$$\Phi_G(\lambda-\lambda_0) = \frac{1}{\Delta\lambda_G}\sqrt{\frac{\ln 2}{\pi}}\exp\left[-\ln 2\frac{(\lambda-\lambda_0)^2}{\Delta\lambda_G{}^2}\right], \tag{4.14}$$

---

[1] The Einstein coefficient A_{ul} [sec^{-1}] is related to the dimensionless absorption oscillator strength f_{lu} by:

$$A_{ul} = \frac{8\pi^2 e^2}{4\pi\varepsilon_0 m_e c(\lambda_{ul})^2}\frac{g_l}{g_u}f_{lu} = \frac{6.670\times10^{15}}{(\lambda_{ul}[\text{Angstrom}])^2}\frac{g_l}{g_u}f_{lu}$$

the four other mechanisms produce a Lorentzian profile:

$$\Phi_L(\lambda-\lambda_0)=\frac{\Delta\lambda_L}{\pi(\lambda-\lambda_0)^2+\Delta\lambda_L^2}. \tag{4.15}$$

We have neglected in the above equation the frequency shift that usually accompanies Lorentzian mechanisms for it is much smaller than the linewidth of the transitions considered in our study. It should be noted also that the total Lorentzian half width is the sum of all Lorentzian widths, i.e. $\Delta\lambda_L = \Delta\lambda_{natural}+\Delta\lambda_{Stark}+\Delta\lambda_{Resonance}+\Delta\lambda_{van\ der\ Waals}$. The profile due to both broadening types is called the Voigt profile:

$$\Phi_{Voigt}(\lambda-\lambda_0)=\frac{a}{\pi\Delta\lambda_D}\sqrt{\frac{\ln 2}{\pi}}\int_{-\infty}^{+\infty}\frac{e^{-y^2}}{a^2+(\xi-y)^2}dy, \tag{4.16}$$

with

$$a=\sqrt{\ln 2}\,\frac{\Delta\lambda_L}{\Delta\lambda_D},\ \text{and}\ \xi=\sqrt{\ln 2}\,\frac{\lambda-\lambda_0}{\Delta\lambda_D}. \tag{4.17}$$

It is therefore important to determine which broadening mechanisms have an influence on the total line broadening. This and expressions for the half widths at half maximum are presented below. All terms in the equations are in SI units, unless explicitly specified otherwise.

Doppler broadening: If the photon emitted during the transition has a frequency ν_0 in the reference frame of the emitting molecule, an observer placed in the laboratory frame will see the molecules coming in its direction with a velocity v emit a photon of frequency $\nu = \nu_0(1+v/c)$. If the molecules have a Boltzmann velocity distribution characterized by the heavy particle temperature T_h, the resulting Doppler line is Gaussian with a half width at half maximum given by:

$$\Delta\lambda_{Doppler}=\frac{1}{2}\lambda_{ul}\sqrt{\frac{8kT_h}{m_hc^2}}=3.58\times10^{-7}\,\lambda_{ul}\sqrt{\frac{T_h[K]}{\hat{M}_h[g/mol]}}. \tag{4.18}$$

Natural broadening is due to the Heisenberg uncertainty principle applied to the energies of the initial and the final state of the transition. This results in an uncertainty on the transition frequency or wavelength which translates into a Lorentzian line profile of half width at half maximum:

$$\Delta\lambda_{Natural}=\frac{\lambda_{ul}^2}{2c}\left(\sum_{n<u}A_{un}+\sum_{n<l}A_{lm}\right), \tag{4.19}$$

where the two summation terms are the inverses of the transition's upper and lower level lifetimes. Natural broadening, which is generally negligible in comparison with the other mechanisms,

represents a lower bound to the spectral linewidth. In the case of the oxygen line at 7.773 Å the natural half width at half maximum was calculated using the constants of Wiese et al (1966) and found to be $\Delta\lambda_{Natural} = 3.4\times10^{-4}$ Å.

The next three broadening mechanisms, resonance, van der Waals, and Stark, are respectively due to collisions with "like" neutrals, "unlike" neutrals, and charged particles. A brief description follows along with numerical expressions and applications to the oxygen line.

Resonance broadening is caused by collisions between "like" particles (e.g. two oxygen atoms) where the perturber's initial state is connected by an allowed transition to either the upper or lower state of the radiative transition under consideration. Typically, the three perturbing transitions that need to be considered are $g\rightarrow l$, $g\rightarrow u$, and $l\rightarrow u$, where g stands for the ground state of the particles, and l and u for the lower and upper states of the radiative transition, as usual. Using the expression given by Griem (1964, p 97), we obtain:

$$\Delta\lambda_{Resonance} = \underbrace{\frac{3e^2}{16\pi^2\varepsilon_0 m_e c^2}}_{6.72\times10^{-16}} \lambda_{ul}^2 \left[\lambda_{lg} f_{gl} \sqrt{\frac{g_g}{g_l}} n_g + \lambda_{ug} f_{gu} \sqrt{\frac{g_g}{g_u}} n_g + \lambda_{ul} f_{lu} \sqrt{\frac{g_l}{g_u}} n_l \right], \qquad (4.20)$$

For the oxygen line at 7,773 Å, the constants listed by Wiese et al (1966) for the relevant transitions lead to:

$$\Delta\lambda_{Resonance}[\text{Å}] \approx \left(2.76\times10^{-3} + 6.851\exp(-106.226/T_h)\right) X_O P[\text{atm}] T_h, \qquad (4.21)$$

which has a maximum of 3.5×10^{-6} Å at 10,000 K. In other words, resonance broadening is completely negligible for this oxygen transition—indeed only the lower state is connected to the ground state by an allowed transition, and only very weakly so since $f_{gl} = 5.4\times10^{-7}$.

Van der Waals broadening is caused by collisions with neutral perturbers that do not share a resonant transition with the radiating particle. Griem (1964, p 99) gives the following expression for a radiator r colliding with a perturber p:

$$\Delta\lambda_{van\ der\ Waals} = \frac{\lambda_{ul}^2}{2c} \left(\frac{9\pi\hbar^5 \overline{R_r^2}}{16 m_e^3 E_p^2} \right)^{2/5} \overline{v_{rp}^{3/5}} N_p, \qquad (4.22)$$

with

$$\overline{R_\alpha^2} \approx \frac{1}{2}\frac{E_H}{E_\infty - E_\alpha}\left[5\frac{z^2 E_H}{E_\infty - E_\alpha} - 1 - 3l_\alpha(l_\alpha+1)\right]. \tag{4.23}$$

In the above expressions, E_p is the energy of the first excited state of the perturber connected with its ground state by an allowed transition. E_H and E_∞ are the ionization potential of the hydrogen atom and of the radiating atom, respectively, E_α is the excitation potential of the upper state of the line. l_α is its orbital quantum number. z is the number of effective charges, N_p is the number density of the perturbing species, and v is the relative speed of the radiating atom and the perturber. The relative velocity term can be expressed as a function of the mean speed:

$$\overline{v_{rp}^{3/5}} = (4/\pi)^{2/10}\,\Gamma(9/5)\left(\overline{v_{rp}}\right)^{3/5} = 0.98\left(\overline{v_{rp}}\right)^{3/5} = 0.98\left(\sqrt{8kT/\pi m_{rp}^*}\right)^{3/5} \tag{4.24}$$

where m_{rp}^* is the reduced mass of the radiator and the perturber. Summing over all perturbers present in the plasma and introducing the mole fraction X_p of perturber p, Eq. 4.22 becomes:

$$\Delta\lambda_{van\ der\ Waals} \approx \frac{\lambda_{ul}^2}{2c}\left(\frac{9\pi\hbar^5\overline{R_\alpha^2}}{16m_e^3}\right)^{2/5}\left(\sqrt{8kT/\pi}\right)^{3/5}\frac{P}{kT}\sum_p\left[\frac{X_p}{E_p^{4/5}\left(m_{rp}^*\right)^{3/10}}\right]. \tag{4.25}$$

The summation in this expression runs over all neutral species present in the plasma. For an air plasma, the five perturbers that must be considered are O, N, N_2, O_2, and NO, which together constitute 98% of the chemical equilibrium composition for temperatures up to 10,000 K. We computed the mole fractions of these five components up to 10,000 K and combined these values with the E_p's and m_{rp}^*'s that are indicated in Table 4.2. Note that the reduced masses indicated in the table are for the case where the radiator is an oxygen atom. When a different radiator is considered, a new set must be considered.

Perturber	M_{rp}^* [g/mole]	Transition issued from the first excited state optically connected to the ground state.	E_p [eV]	$M_{rp}^{*\,-0.3}E_p^{-0.8}$
O	8.00	$^3S^0 \rightarrow {}^3P^0$	9.5	0.088
N	7.47	$^4P \rightarrow {}^4S^0$	10.3	0.085
O_2	10.67	$A^3\Sigma_u^+ \rightarrow X^3\Sigma_g^-$ (Herzberg I)	4.4	0.150
N_2	10.18	$a'^1\Sigma_u^- \rightarrow X^1\Sigma_g^+$ (Willkinson-Mulliken)	8.5	0.090
NO	10.43	$A^2\Sigma^+ \rightarrow X^2\Pi$ (Gamma)	5.5	0.127

Table 4.2. Constants needed in Eq. 4.25 when the radiator is an oxygen atom. For other radiators, the reduced mass must of course be modified as warranted.

The summation term in Eq. 4.25 was calculated up to 10,000 K for several radiators, namely O, N, O_2, N_2, and NO.

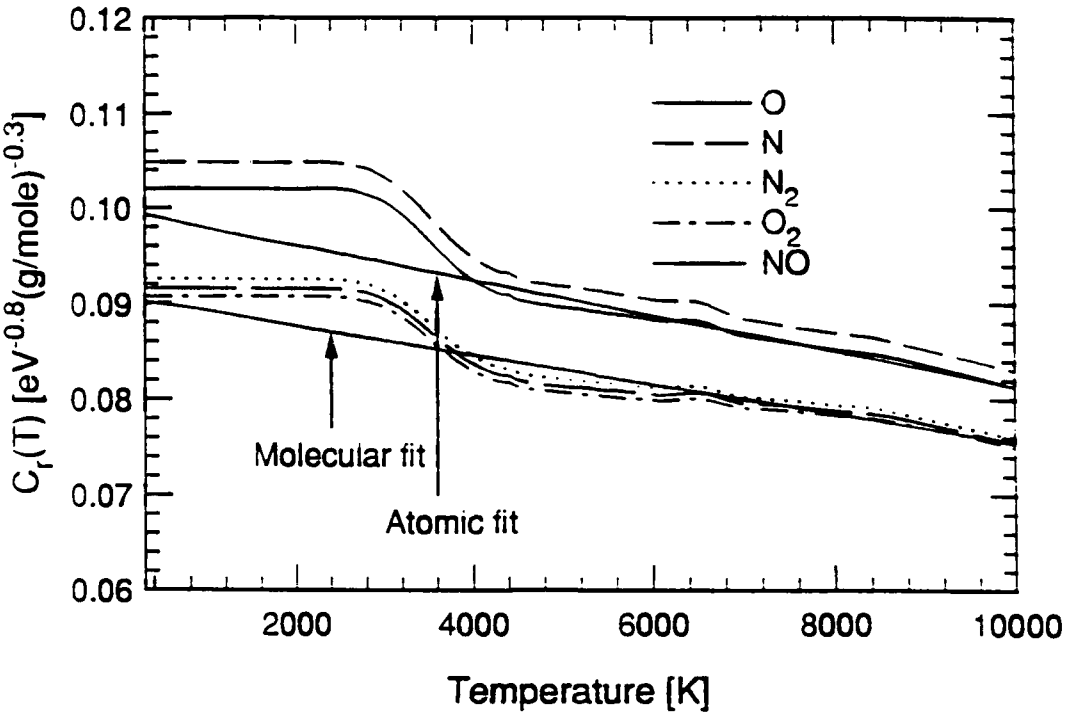

Figure 4.6. Evolution of C_r with temperature for O, N, N_2, O_2, and NO as the radiator *r*.

As can be seen in Fig. 4.6, this term is almost constant over the entire temperature range for either O, N, N_2 O_2 or NO as a radiator. An approximate linear fit of the curves shown in Fig. 4.6 was performed for each of the radiating species previously mentioned. For air in chemical equilibrium at temperatures up to 10,000 K, it is therefore possible to give analytical formulas for the van der Waals broadening of O, N, O_2, N_2, and NO lines:

$$\Delta\lambda_{van\ der\ Waals} \approx 4.0\times10^{-2}(\lambda_{ul})^2 T^{-0.7} P\left(R_\alpha^2\right)^{0.4} C_r(T) \qquad (4.26)$$

where R_α^2 depends only on the radiating species and on the transition under consideration, and where $C_r(T)$, defined as

$$C_r(T) = \sum_p \frac{X_p}{(E_p[eV])^{0.8}\left(M_{r_p}^*[g/mol]\right)^{0.3}}, \qquad (4.27)$$

is a function that only depends on temperature (although very weakly) and on the radiating species. The $C_r(T)$ functions for O, N, N_2, O_2, and NO are summarized in Table 4.3.

Radiator r	$C_r(T)$ [(eV)$^{-0.8}$(g/mole)$^{-0.3}$]
O or N	$0.10\text{-}1.9\times10^{-6}T$
N_2, O_2 or NO	$0.08\text{-}1.3\times10^{-6}T$

Table 4.3. Van der Waals broadening coefficients for O, N, N_2, O_2, and NO lines in a chemical equilibrium air plasma. These fits are within better than 10% of the actual values for all temperatures up to 10,000 K.

We can now determine an expression for the van der Waals broadening of the oxygen atom transition at 7,773 Å. Recalling that for oxygen atoms the effective charge number z is equal to 1 and that the ionization potential is 13.614 eV, that the excitation potential E_α of the upper state of the line at 7,773 Å is 10.75 eV and its orbital quantum number l_α is 1, and finally that E_H = 13.6 eV, the matrix element of Eq. 4.24 can be calculated:

$$\overline{R_\alpha^2} \approx \frac{1}{2}\frac{13.6[\text{eV}]}{13.614[\text{eV}]-10.75[\text{eV}]}\left[5\frac{1^2\times13.6}{13.614-10.75}-1-3\times1(1+1)\right]=44.5. \qquad (4.28)$$

We finally obtain for the van der Waals broadening of the oxygen line at 7,773 Å:

$$\Delta\lambda_{van\,der\,Waals} = \left(11.2-2.12\times10^{-4}T\right)T^{-0.7}P[atm] \qquad (4.29)$$

Van der Waals broadening therefore decreases with temperature, which is not surprising since although the collision frequency increases with temperature, the density decreases faster.

Stark broadening is due to the Coulomb interaction between the outer electron of the radiator and the charged particles present in the plasma. Both ions and electrons induce broadening but because of their comparatively higher relative velocities electrons are responsible for most of it. For this reason, we consider only electron Stark broadening which is a function of the free electron number density and a weak function of the electron temperature. Griem (1964) gives the following expression for electron Stark broadening:

$$\Delta\lambda_{Stark}[\text{Å}] \approx w(T_e)\frac{n_e[cm^{-3}]}{10^{16}} \qquad (4.30)$$

where $w(T_e)$ is a tabulated function in units of Å that depends on the radiator and on the transition. Griem provides numerical values for the most important transitions of a number of atoms (Griem, 1964, Table 4.5, pp. 454 *ff.*). For the oxygen line at 7,773 Å, $w(T_e)$ varies between 1.99×10^{-2} Å at 2,500 K, 2.48×10^{-2} Å at 5,000 K, and 3.27×10^{-2} Å at 10,000 K (*ib.*, p 468).

Broadening widths for the mechanisms presented above are plotted as a function of temperature up to 10,000 K in Fig. 4.7 where it appears that Doppler and Van der Waals broadening are the dominant mechanisms for the oxygen line. A Voigt profile must therefore be computed and substituted in Equation 4.13 to determine the spectral absorption coefficient k_λ as a function of temperature. Since no analytical expression exists for the Voigt profile, the numerical program proposed by Drayson (1976) was used to compute Voigt line profiles.

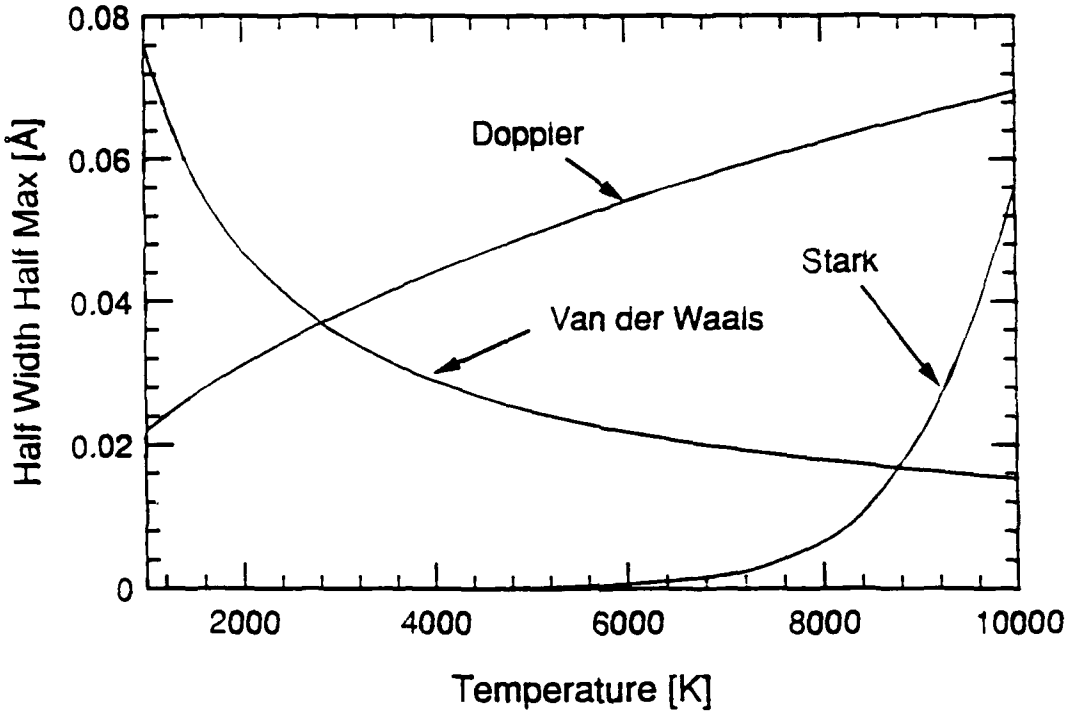

Figure 4.7. Broadening widths for the oxygen triplet at 7,773 A

We can now return to the problem of interest which is to correct the measured temperature for line self absorption. The procedure is as follows: We first use the measured lateral intensity profile and assume that there is no absorption to determine an "optically thin" temperature profile from the line under consideration. We then divide the plasma in 25 equally spaced (1 mm) concentric rings in which thermodynamic properties are nearly constant and defined by the optically thin temperature profile.

With the conventions of Fig. 4.8, the radiative transport equation for a given ring n at a given lateral location z reads:

$$I_n(\lambda) = B_\lambda(T_n)\left[1-\exp\left(-k'_n(\lambda)l_n(z)\right)\right] + I'_n(\lambda)\exp\left(-k'_n(\lambda)l_n(z)\right) \qquad (4.31)$$

where k_n' is the absorption coefficient corrected for stimulated emission, which is related to the absorption coefficient by the following relation for a plasma in LTE:

$$k_n(\lambda) = k_n(\lambda)\left[1 - \exp(-\epsilon_{ul}/kT_n)\right], \tag{4.32}$$

and where $B_\lambda(T)$ is the Planck blackbody function:

$$B_\lambda(T_n) = \frac{C_1}{\lambda_{ul}^5\left(\exp(-C_2/\lambda_{ul}T_n) - 1\right)}, \tag{4.33}$$

with $C_1 = 1.19\times10^4$ Wμm^{4}cm^{-2}sr^{-1}, and $C_2 = 1.438\times10^4$ μmK.

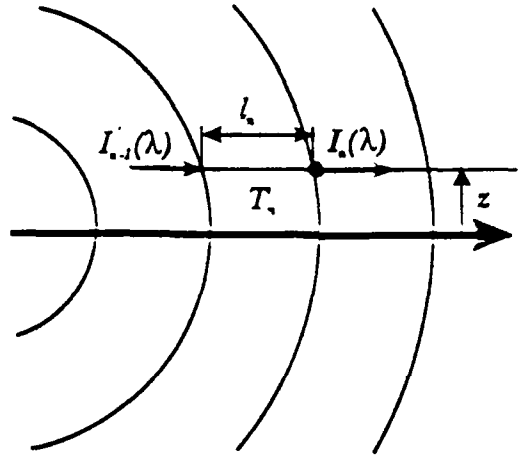

Figure 4.8. Defining elements for the radiative transport equation Eq. 4.31.

In Eq. 4.31, the first term corresponds to the net light emitted by the plasma in the n^{th} layer, and the second term corresponds to the amount of light incident on the n^{th} layer that got transmitted by that layer. When all layers are included, a spectral profile is obtained for the given lateral position z. Along a plasma diameter (z=0), one obtains the spectral profile shown in Fig. 4.9. At the exit of the last layer, the intensity profile is spectrally integrated to determine the total line intensity corrected for self absorption.

We can thereby reconstruct a lateral profile of net emitted intensity, and compare it to what it would be if the plasma were optically thin. This procedure was numerically performed and $\eta_1(z)$, the resulting ratio between the profile including spectral absorption and the optically thin one, is plotted in Fig. 4.10 for the oxygen triplet at 7,773 Å. We then multiply the measured lateral intensity profile by $\eta_1(z)$ and recompute a new temperature profile using the same method as previously described. This procedure is then iterated, that is a new profile of self absorbed over optically thin intensity $\eta_2(z)$ is calculated to more accurately correct the original measured lateral intensity profile, and again a new temperature profile is calculated. After a few iterations, the temperature profiles do not change by more than a fraction of a degree Kelvin. At this point, the

resulting temperature profile is corrected for self absorption. It should be noted here that convergence to less than a few degrees is typically obtained with only one iteration.

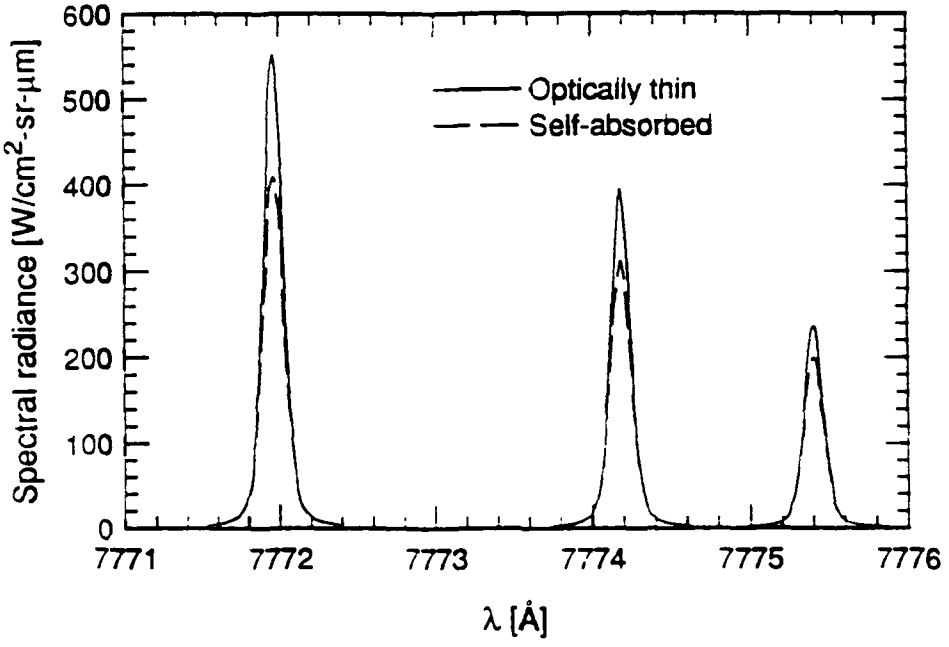

Figure 4.9. Numerical prediction of the spectral emission of the oxygen triplet at 7,773 Å along a diameter of the plasma (z=0).

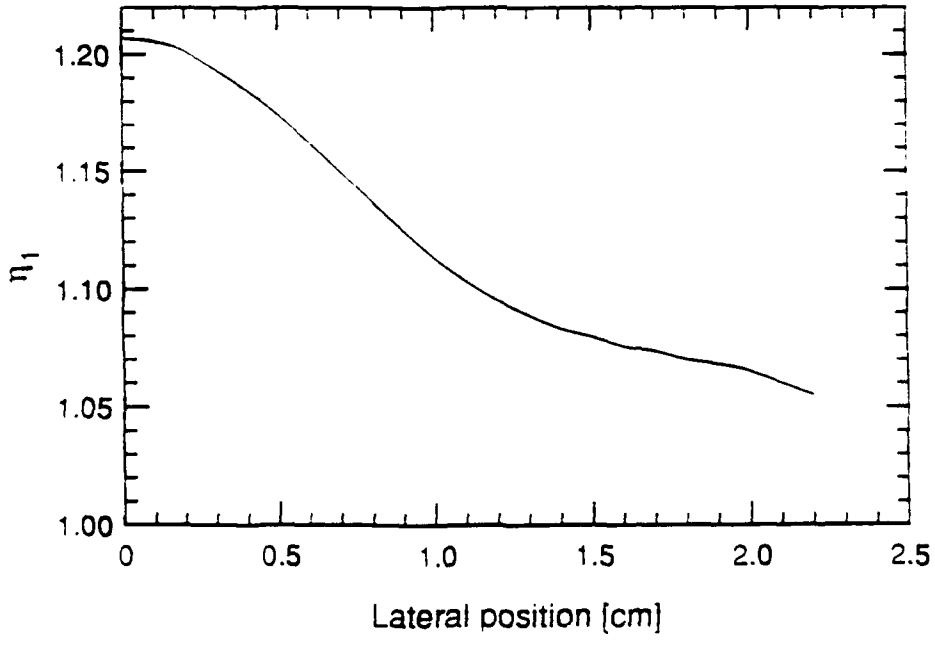

Figure 4.10. Ratio between the optically thin and the self-absorbed integrated emission of the oxygen triplet as a function of lateral position z.

The LTE temperature profile of the oxygen line at 7,773 Å corrected for self absorption is plotted in Fig. 4.11 along with the optically-thin profile. As can be seen, the difference is at most 100 K, which is no more than the uncertainty due to Einstein coefficients and experimental errors. A similar treatment was also applied to the four other temperature profiles and the corrections never exceed 80 K.

The conclusions reached earlier regarding the LTE distribution of the electronic levels are therefore unchanged after an uncertainty analysis and corrections for line self-absorption.

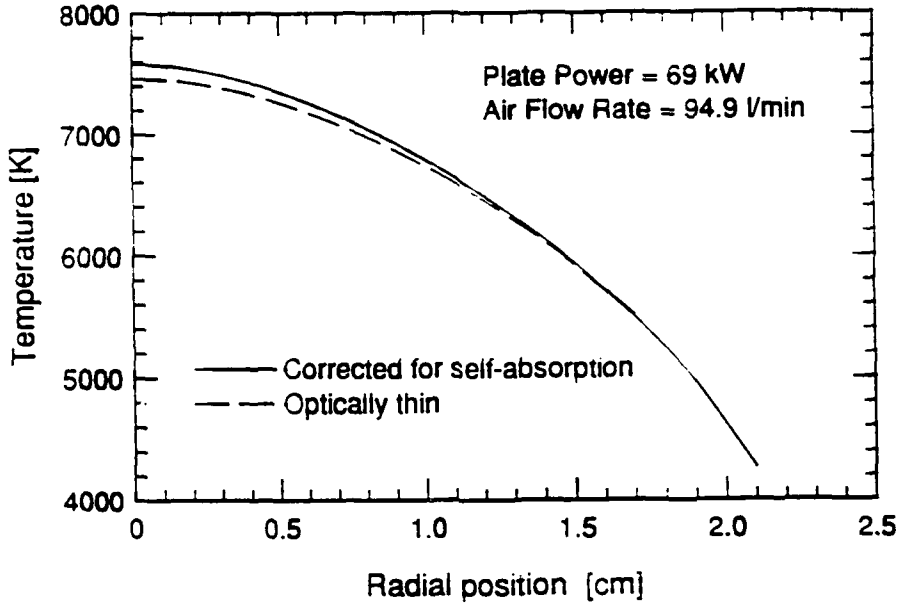

Figure 4.11. Self absorption correction of the LTE temperature from the 7,773 Å oxygen triplet.

4.2.1.b Boltzmann temperature

Another way to examine possible departures from LTE is developed in this section with the introduction of the so-called Boltzmann temperature. The Boltzmann temperature T_B is defined by the distribution of excited electronic levels. It is obtained from the Boltzmann relation between the number densities of at least two excited levels of a same atom.

$$\frac{n_{u1}}{g_{u1}} = \frac{n_{u2}}{g_{u2}} \exp\left(-\frac{\varepsilon_{u1} - \varepsilon_{u2}}{k T_B} \right). \tag{4.34}$$

Two transitions originating from different upper states u1 and u2 are therefore needed. While the oxygen lines of the previous section may be used, the nitrogen lines do not qualify because they have a common upper state. Although LTE and Boltzmann temperatures are not

independent (Eq. 4.34 is the ratio of Eq. 4.3 written for two electronic levels), the Boltzmann temperature offers several advantages. First, it has a physical meaning, because even when the plasma is not in LTE, T_B represents the kinetic temperature of the free electrons if the probed levels are close to the ionization limit. This stems from the fact that high-lying electronic levels tend to be in equilibrium with the free electrons. Second, in contrast to the LTE temperature, no assumption needs to be made about the ground state number density since it is no longer involved. Finally, the Boltzmann temperature is more sensitive to a possible non-equilibrium distribution of the electronic levels. However, the latter point also implies that the Boltzmann temperature cannot be determined as accurately as the LTE temperature because it involves the Einstein coefficients of two transitions, and these are not yet known very precisely (10% for the two oxygen lines).

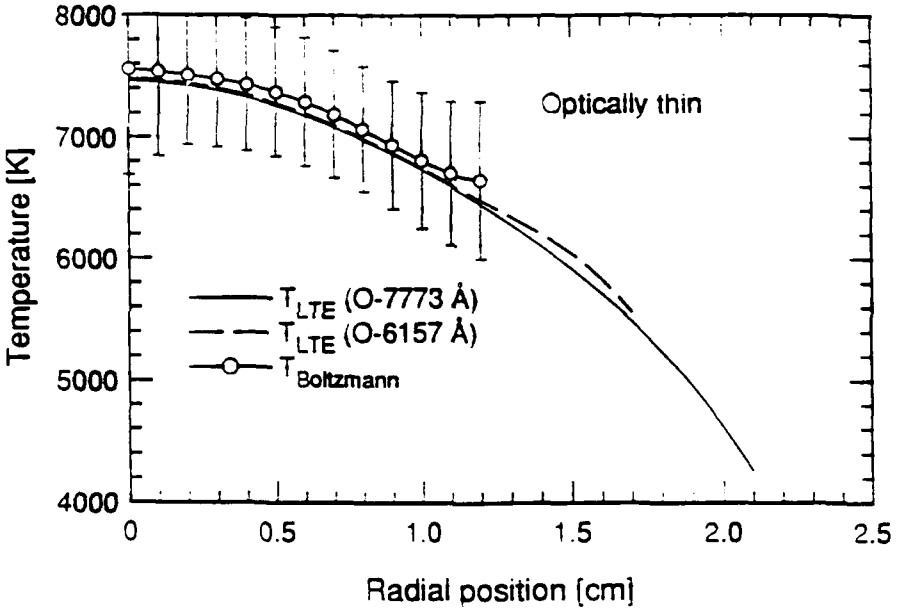

Figure 4.12. Boltzmann temperature determined from the relative intensity of the two oxygen lines.

The following uncertainty analysis gives an idea about the precision to expect for the Boltzmann temperature based on two lines. Defining $n_u^* = n_u/g_u$, Eq. 4.34 may be rearranged as:

$$\frac{1}{T_B} = \frac{k}{\varepsilon_{u2} - \varepsilon_{u1}} \ln\left(\frac{n_{u1}^*}{n_{u2}^*}\right). \tag{4.35}$$

Taking the logarithm and differentiating, this equation becomes:

$$\left|\frac{\Delta T_B}{T_B}\right| = \frac{T_B}{\left|\varepsilon_{u2} - \varepsilon_{u1}\right|} \left|\frac{\Delta(n_{u1}^*/n_{u2}^*)}{n_{u1}^*/n_{u2}^*}\right|. \tag{4.36}$$

The energy difference between the two oxygen levels being 2.03 eV, the uncertainty at 6.000 K is

then

$$\left|\frac{\Delta T_B}{T_B}\right| \equiv 0.25\left|\frac{\Delta(n_{u1}^*/n_{u2}^*)}{n_{u1}^*/n_{u2}^*}\right|. \tag{4.37}$$

Since the number density ratio cannot be known with better than 20% accuracy due to uncertainties on Einstein coefficients alone, the Boltzmann temperature cannot be determined to an accuracy better than 5%. Although it can be argued that the ratio of Einstein coefficients should be more accurate than their absolute magnitude, the error bars indicated in Fig. 4.12 do include the effect of 10% uncertainty on these coefficients in addition to all the other uncertainty causes that were mentioned previously in the LTE temperature determination procedure. Also plotted in Fig. 4.12 are the LTE temperatures from the oxygen lines at 7,773 Å and at 6,157 Å. The comparison shows that the Boltzmann temperature is within experimental uncertainty from the LTE temperatures discussed in the previous section.

The last question to be addressed here concerns the effect of self absorption on the Boltzmann temperature profile. The two oxygen line intensity profiles corrected for self absorption lead to the Boltzmann temperature presented in Fig. 4.13 along with the corrected LTE temperature from the oxygen lines at 7,773 Å and at 6,157 Å. This corrected Boltzmann profile is also within experimental uncertainty of the LTE temperatures.

In conclusion, the Boltzmann temperature also support a Boltzmann distribution of the electronic levels.

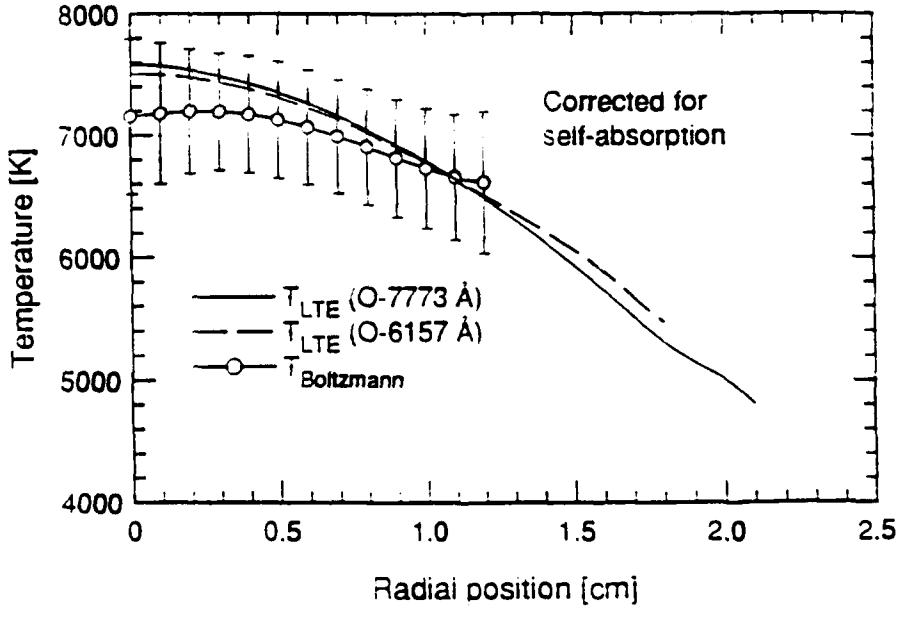

Figure 4.13. Boltzmann temperature determined from the relative intensity of the two oxygen lines corrected for self absorption.

4.2.1.c. Electron number density

A more direct way to determine whether the outer electronic levels are overpopulated due to an elevated free electron number density is precisely to measure the free electron number density. To that purpose, a small amount (1.9 l/min) of hydrogen H_2 was mixed with the 95 l/min air flow and injected into the torch. At the operating temperature conditions, H_2 dissociates almost completely and several atomic hydrogen lines from the Balmer series appear in the visible, in particular the H_β transition at 4861.32 Å. The H_β line is Stark-broadened due to collisions between the hydrogen atoms and the charged particles which are present in this temperature range.

Stark broadening of the H_β transition has been widely studied (Griem, 1964, Vidal et al, 1973). It is a function of the free electron concentration and a weak function of temperature. A fit of the values given by Vidal et al (1973) gives for the Stark Half Width at Half Maximum:

$$\Delta\lambda_{Stark}[\text{ Å}] = 1.740\times10^{-10}\left(n_e[\text{cm}^{-3}]\right)^{0.647}. \qquad (4.38)$$

This fit is valid for electron densities between 10^{13} and 10^{17} cm^{-3} but it does not take into account the temperature dependence since the correction would not exceed a factor 20% over the temperature range 5,000 to 40,000 K.

The other broadening mechanisms are also examined following the same method as in Section 4.2.1.b. Half Widths at Half Maximum for the H_β line in an air plasma are summarized in Table 4.4 and plotted as a function of the electron number density in Figure 4.14. The conversion from temperature to electron number density was done assuming a chemical equilibrium concentration of electrons. Over the temperature range of interest here (5,000 to 7,500 K), resonance broadening is negligible since it does not exceed 0.005 Å for a hydrogen mole fraction of 4%.

$\Delta\lambda_{Stark}$	$\Delta\lambda_{resonance}$	$\Delta\lambda_{van\ der\ Waals}$	$\Delta\lambda_{Doppler}$
$1.74\times10^{-10}\left(n_e[\text{cm}^{-3}]\right)^{0.647}$	$592X_H\frac{P[\text{atm}]}{T}$	$(24.5-6.00\times10^{-4}T)\frac{P[\text{atm}]}{T^{0.7}}$	$1.74\times10^{-3}\sqrt{T}$

Table 4.4. Half Widths at Half Maximum (in Å) for the hydrogen beta line at 4861.32 Å

The monochromator entrance and exit slits were both set to 40 µm which should correspond to a Gaussian slit function of half width at half maximum equal to 0.22 Å. These very small widths are necessary to introduce as little instrumental broadening as possible. However, as can be seen in Fig. 4.14, the resulting theoretical instrumental broadening is already larger than the Doppler broadening which is the only other mechanism that gives a Gaussian component to the

Voigt profile. It is therefore critical to determine the instrumental broadening quite accurately. The quoted instrumental broadening is not very accurate because the physical slit settings are close to the narrowest achievable width for the monochromator. For that reason, the actual slit function was measured with a narrow spectral source (HeNe at 6.328Å); it was found to be nearly Gaussian with a half width at half maximum of 0.3 ±0.05 Å. An instrumental broadening of 0.3 Å was therefore taken into account to determine the relation between the half width at half maximum and the electron number density. The resulting Voigt HWHM is shown in Fig. 4.14.

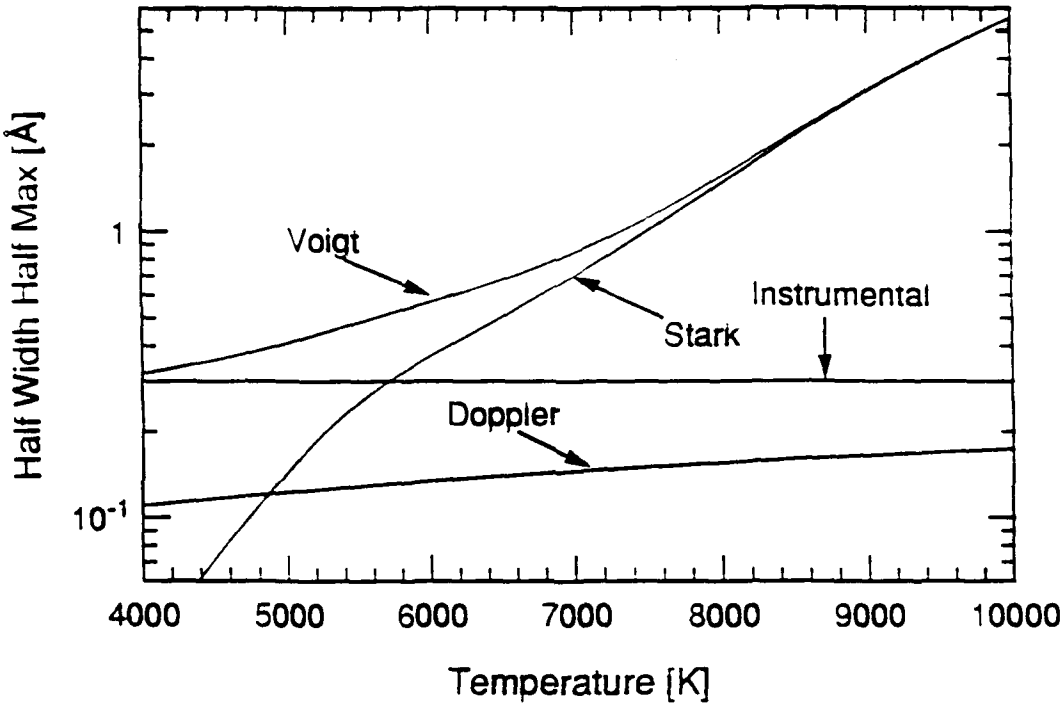

Figure 4.14. Broadening widths for the hydrogen beta line at 4861.32 Å.

The H_β line-shape was measured every mm over the radius of the plasma, yielding 25 profiles such as the one shown in Fig. 4.15. The distortion is due to the underlying continuum which essentially comprises bands of the second positive system of N_2. The spectrum was therefore also measured in pure air to determine the baseline. When the baseline is subtracted, a symmetric line-shape is recovered. The line profiles were then Abel-inverted, and the electron number density determined from their half width at half maximum.

Figure 4.16 shows the measured electron number density profile out to a radius of about 1.5 cm. Beyond that point, the H_β line intensity decreases below the detection limit. Also shown in Figure 4.16 is the chemical equilibrium electron density which was calculated from the LTE temperature of the oxygen line at 7.773 Å corrected for self-absorption. The close agreement between the two profiles shows that the electron number density is not elevated with respect to its

equilibrium value. This electron number density measurement therefore adds further support to a Boltzmann distribution of the electronic levels.

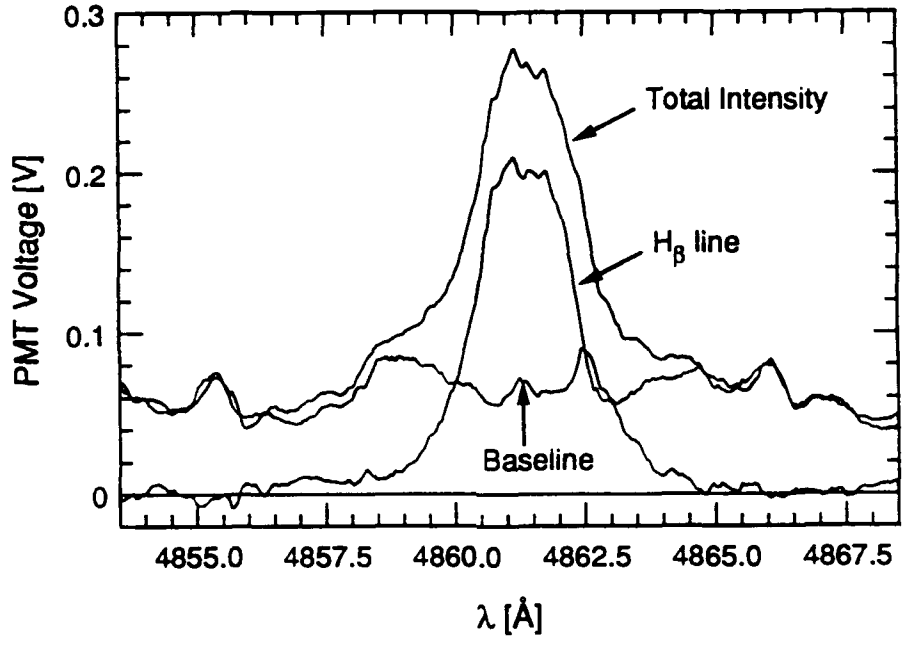

Figure 4.15. H_β line profile reconstruction obtained by subtracting the baseline signal due mainly to N_2 from the total measured intensity.

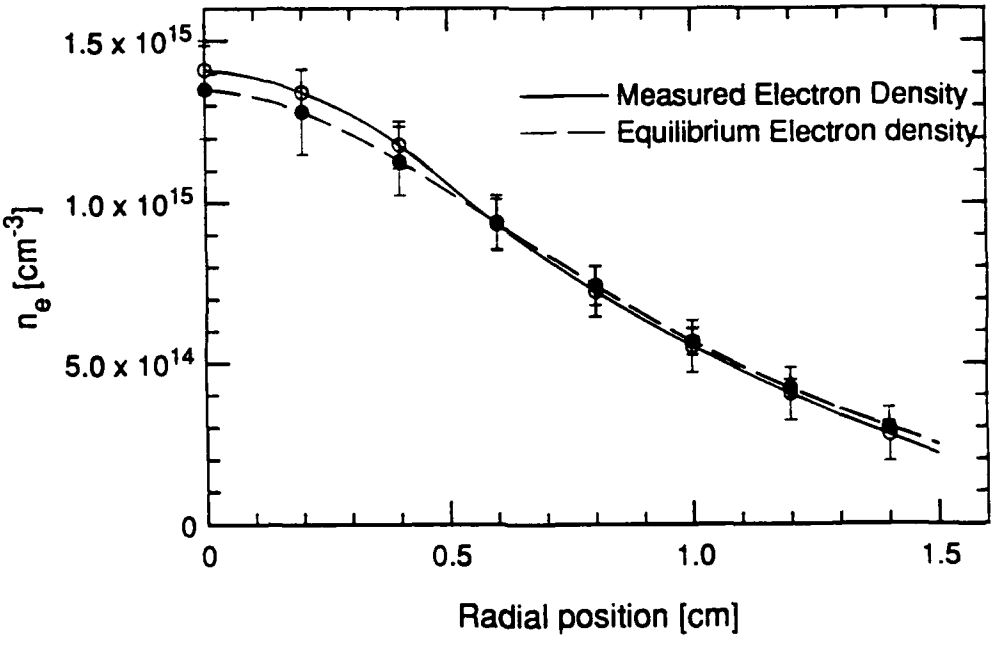

Figure 4.16. Comparison between measured and predicted equilibrium electron number density.

4.2.2. Rotational temperature

4.2.2.a. $N_2^+(0,0)$ band

Rotational temperatures can be measured by resolving rotational lines and inferring a temperature from molecular Boltzmann plots (Tourin, 1966). We have applied this technique to the rotational lines of the (0,0) vibrational band of the N_2^+ first negative system. However, even with many rotational lines (23 in our case), the temperature profile obtained through Abel-inversion is extremely sensitive to the uncertainty in the measurements because the energy spacing between rotational levels is very small. Consequently, we only determined a temperature from a rotational spectrum measured along the diameter of the plasma. This temperature corresponds nevertheless to an average rotational temperature over the central part of the plasma where N_2^+ has its maximum emission. As shown in Figure 4.17, this radially averaged temperature lies within the LTE and Boltzmann temperatures, and is therefore consistent with rotational equilibrium.

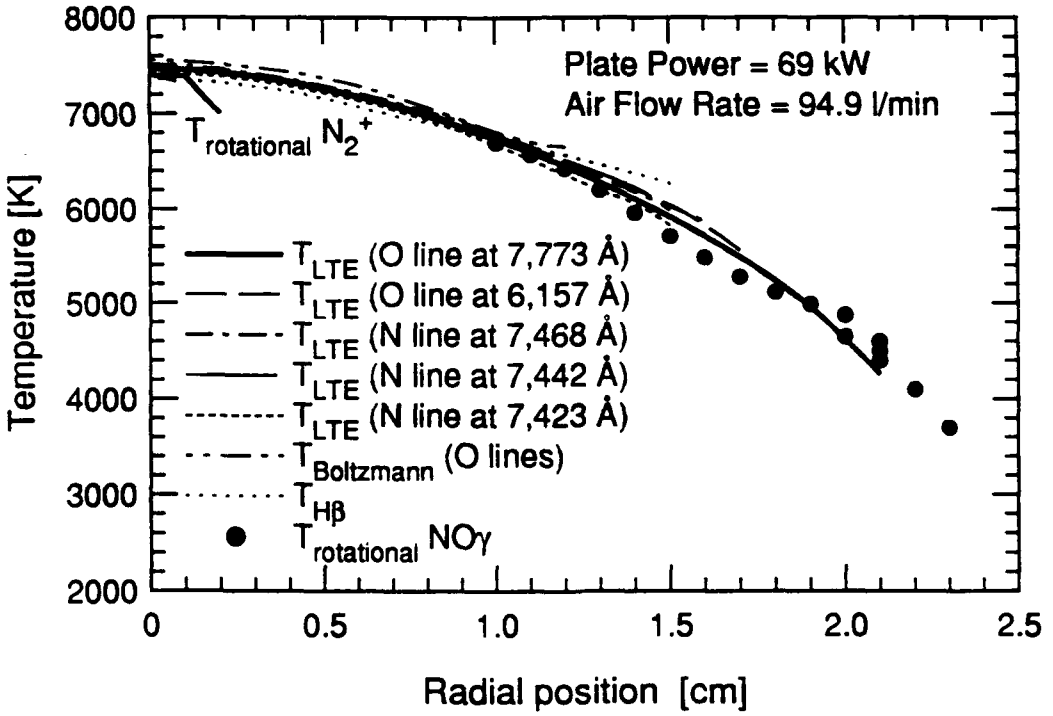

Figure 4.17 LTE, Boltzmann, and rotational temperature profiles in the plasma torch.

4.2.2.b. NO γ (0,1) band

A rotational temperature was also obtained from the Abel-inverted shape of the (0,1) band of NO Gamma following the work by Gomès et al (1992). This technique is currently limited to regions below 6,500 K, since above that temperature NO Delta and Epsilon bands interfere with NO Gamma. The technique could be extended above 6,500 K if the absolute intensity of these superimposed bands were known with good accuracy, but this is not yet the case. Again, good agreement is obtained with the previous temperatures, which adds further support to rotational equilibrium.

4.3. Chemical equilibrium

The question of chemical equilibrium was addressed using the kinetic code *CHEMKIN* (Kee et al., 1986) with 11 air species and with the 33 reactions for which rates were selected by Park (1989). In this code, the reverse reaction rates are computed from the forward rates and from thermodynamic constants. Since the *CHEMKIN* thermodynamic data base is limited to temperatures below 5,000 K, we extended the range up to 10,000 K using the thermodynamic functions of Liu (1989, 1990).

As mentioned in Section 2.3, the maximum temperature reached by the plasma in the induction region is estimated to be around 9,000 K. At the point where the spectral measurements are made, the maximum temperature is about 7,500 K as follows from the measurements presented in Section 4.2. The flow time between these two points is on the order of 10 milliseconds. If we assume that the plasma in the coil region is in chemical equilibrium at a temperature of 9,000 K and undergoes instantaneous cooling down to 6,000 K, then the time required to return to equilibrium at 6,000 K would be on the order of one millisecond, as can be seen in Fig 4.18. Since this time is much smaller in comparison with the 10 ms plasma characteristic flow time, flow-induced chemical non-equilibrium is unlikely in this plasma.

Radial diffusion effects and rapid cooling can induce elevated electron number densities at the plasma edges. However, the temperature in those outer regions drops below 5,000 K, and therefore contributes only a negligible percentage to the radiative power emitted along a plasma diameter.

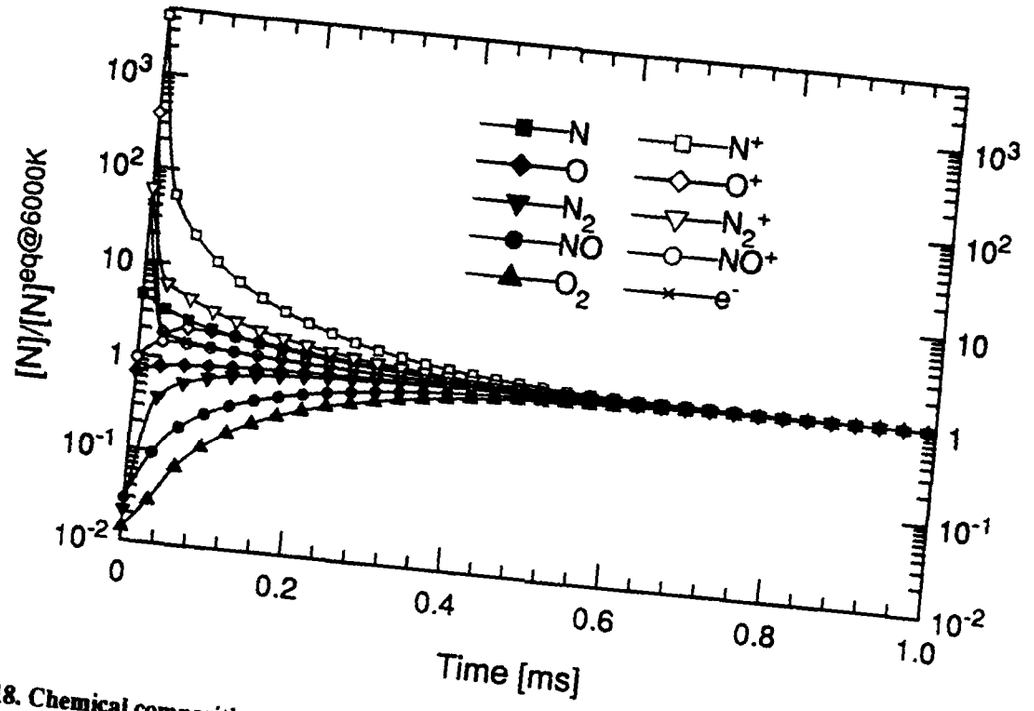

Figure 4.18. Chemical composition evolution with an imposed temperature drop from 9,000 to 6,000 K at t=0.

4.4. Conclusion

In summary, the foregoing results support the assumption of at least approximate LTE over most of the plasma extent. As a result, a single temperature profile fully represents the thermodynamic state of the plasma. Since the oxygen triplet at 7,773 Å provided the most precise temperature, all LTE numerical simulations in the rest of this work are based on this temperature.

5. Spectral emission of air plasmas

5.1. Experimental spectrum

The emission spectrum was recorded between 2,000 and 8,000 Å along a diameter (5 cm) of the plasma. This wavelength range was limited by the poor efficiency of the detection system above 8,000 Å, and by the strong absorption of oxygen in room air below 2,000 Å. Since it is recorded along the plasma diameter, this spectrum includes the contribution of regions at temperatures ranging from 300 to 7,500 K. The monochromator entrance and exit slits were respectively set at 60 and 260 μm, corresponding to a trapezoidal spectral bandpass of base 3.5 and top 2.2 angstroms. The monochromator scanning speed was 2.3 Å/sec. Data were acquired using the lock-in amplifier at a rate of 5 Hz with an averaging time constant of 0.1 second.

The relative spectral response of the detection system was measured with a deuterium lamp (Optronic Model UV-40IR) between 2,000 and 4,000 Å, and a quartz halogen tungsten lamp (Optronic Model 55A) between 3,000 and 8,000 Å. Excellent agreement was obtained between the two calibrations in the overlapping region 3,000-4,000 Å. Absolute intensity calibration was obtained with the quartz-halogen tungsten lamp which is a spectral radiance source traceable to NIST standards. With these two high quality lamps, calibration uncertainties were limited to less than 10%, with the maximum in the extreme regions (2,000-3,000 and 7,000-8,000 Å) of the spectrum.

A high-bandpass optical filter (cut-off at 4,000 Å) was used when recording the spectrum above 6,000 Å, in order to reject the second order structures due to intense near-UV bands such as the (0,0) band of N_2^+ first negative and the (0,0) to (4,4) bands of CN violet which would otherwise appear strongly in the vicinity of the oxygen triplet at 7,774 Å.

The experimental spectrum is presented in Fig. 5.1. As mentioned earlier, it includes strong bands of NO, N_2^+, N_2, CN and lines of O, N, and C. The spectral region 5,000-7,000 Å is not plotted because it does not include prominent spectral features under the present experimental conditions.

5.2. Computed spectrum

The radiative emission spectra presented below were predicted using the *NEQAIR* code (Park, 1985a, b). The required input data are the chemical composition of the plasma, the kinetic temperature of the heavy species (T) and of the free-electrons (T_e), and the rotational and vibrational temperatures (T_r, T_v) of the molecular species.

The code is divided into two parts, an excitation and a radiation module. The excitation module predicts the population distribution of the electronic states in the Quasi-Steady-State (QSS) approximation using a collisional-radiative model for the populations of bound electronic states. The radiative module determines the emission (and absorption) by performing a line-by-line calculation of the radiative contribution of the electronic systems (Whiting, 1969).

In the case of molecules, the contribution at a particular wavelength λ of a rotational transition between two vibrational levels v', v" belonging to different electronic levels e', e'' is:

$$I(\lambda) = \underbrace{N_{e'v'J'}}_{\substack{\text{Excitation}\\ \text{Module}}} \underbrace{A^{e'v'}_{e''v''} S^{J'}_{J''} \Delta E^{e'v'J'}_{e''v''J''} \Phi(\lambda)}_{\substack{\text{Radiation}\\ \text{Module}}}, \tag{5.1}$$

where $N_{e'v'J'}$ is the population of the emitting level, $A^{e'v'}_{e''v''}$ the probability of a radiative transition from (e',v') to (e'',v''), $S^{J'}_{J''}$ (Hönl-London factor), the probability of a transition from J' to J'', $\Delta E^{e'v'J'}_{e''v''J''}$ the difference of energy between the two levels, and $\Phi(\lambda)$ the lineshape function (Doppler, collisional, and Stark broadening).

The goal of the present work is to test the radiative module of *NEQAIR* independently of the excitation module. This is possible since the plasma was found to be in LTE. The QSS computations of the excitation module were therefore by-passed, and the population of the electronic levels replaced by a Boltzmann distribution:

$$\frac{N_{e'}}{N_{total}} = \frac{Q^{e'}_{el} \sum_{v'J'} Q^{e',v'}_{vib} Q^{e',v',J'}_{rot}}{\sum_{e'v'J'} Q^{e'}_{el} Q^{e',v'}_{vib} Q^{e',v',J'}_{rot}}. \tag{5.2}$$

where

$$Q^{e'}_{el} = g_{e'} \exp\left(-\frac{\varepsilon_{e'} - \varepsilon_{e'=0}}{kT}\right), \tag{5.3}$$

$$Q^{e',v'}_{vib} = \exp\left(-\frac{\varepsilon_{v'} - \varepsilon_{v'=0}}{kT}\right), \tag{5.4}$$

$$Q^{e',v',J'}_{rot} = (2J'+1)\exp\left(-\frac{\varepsilon_{J'} - \varepsilon_{J'=0}}{kT}\right), \tag{5.5}$$

are respectively the electronic, vibrational, and rotational partition functions. It should be noted, however, that the populations of most radiating states are predicted to be within 10% of their LTE value when using the QSS approximation. The only exception is the upper state of the First positive system of N_2, but this system is too weak to be measured under our experimental conditions.

To model the experiment, the plasma was divided into 25 equally spaced concentric rings, and thermodynamic properties were assumed uniform in each ring. All temperatures (translational, ro-

tational, vibrational and electronic) were set equal to the LTE temperature measured from the 7,774 Å oxygen triplet. In each ring, the chemical equilibrium composition at the corresponding temperature was calculated with the *STANJAN* code (Reynolds) from a baseline air composition of 78.084% N_2, 20.946% O_2, 0.934% Ar, and 0.033% CO_2. This small amount of atmospheric carbon dioxide is apparently responsible for the formation of CN, whose Violet system is a very intense radiator, and of C, which produces a strong line at 2,478.6 Å.

NEQAIR was used to predict the emission spectrum in each ring between 2,000 and 8,000 Å, with a resolution of 1,000 points per angstrom. This high resolution is not required for optically thin computations, but is necessary for absorption calculations in order to resolve the rotational lines, their width being typically 0.01 Å under the conditions of this experiment. The radiative transport equation is then solved, and after the last slab, the resulting spectrum is convolved with the experimental slit function using a Fast-Fourier transform.

In the following sections, we will first present a comparison between the experimental spectrum and the computations performed with the original version of the code, *NEQAIR-1*, then describe the improvements that were warranted from this analysis, and finally assess the quality of the revised code, *NEQAIR-2*.

5.3. Comparison with *NEQAIR-1*.

The comparison with the predictions of *NEQAIR-1* (see Fig. 5.2) revealed that several features of the code should be improved, particularly the intensity and position of the molecular bands, and that additional bands should be considered. As may be seen from Figs. 5.1 and 5.2:

(a) In the short wavelength range, where radiation is essentially due to NO bands, the numerical spectrum fails to reproduce both the intensity and the shape of the spectral features.

(b) Between 2,950 and 2,975 Å, the (4,2), (3,1), and (2,0) bands of N_2 (second positive system) are more widely spaced than in the experiment.

(c) Between 3,000 and 4,000 Å, where most radiation is due to N_2 (second positive) and N_2^+ (first negative); the intensity of the N_2 bands appears to be a factor 2 too high relative to the N_2^+ bands.

(d) The intensity of the violet system of CN (particularly between 3,800 and 3,876 Å) is strongly under predicted by the code.

(e) The intensities of the atomic nitrogen triplet (7,423-7,442-7,468 Å) and of the atomic oxygen triplet (7,773 Å) are underestimated.

This initial comparison led to a re-examination of the radiative model: the resulting improvements are presented in the next section.

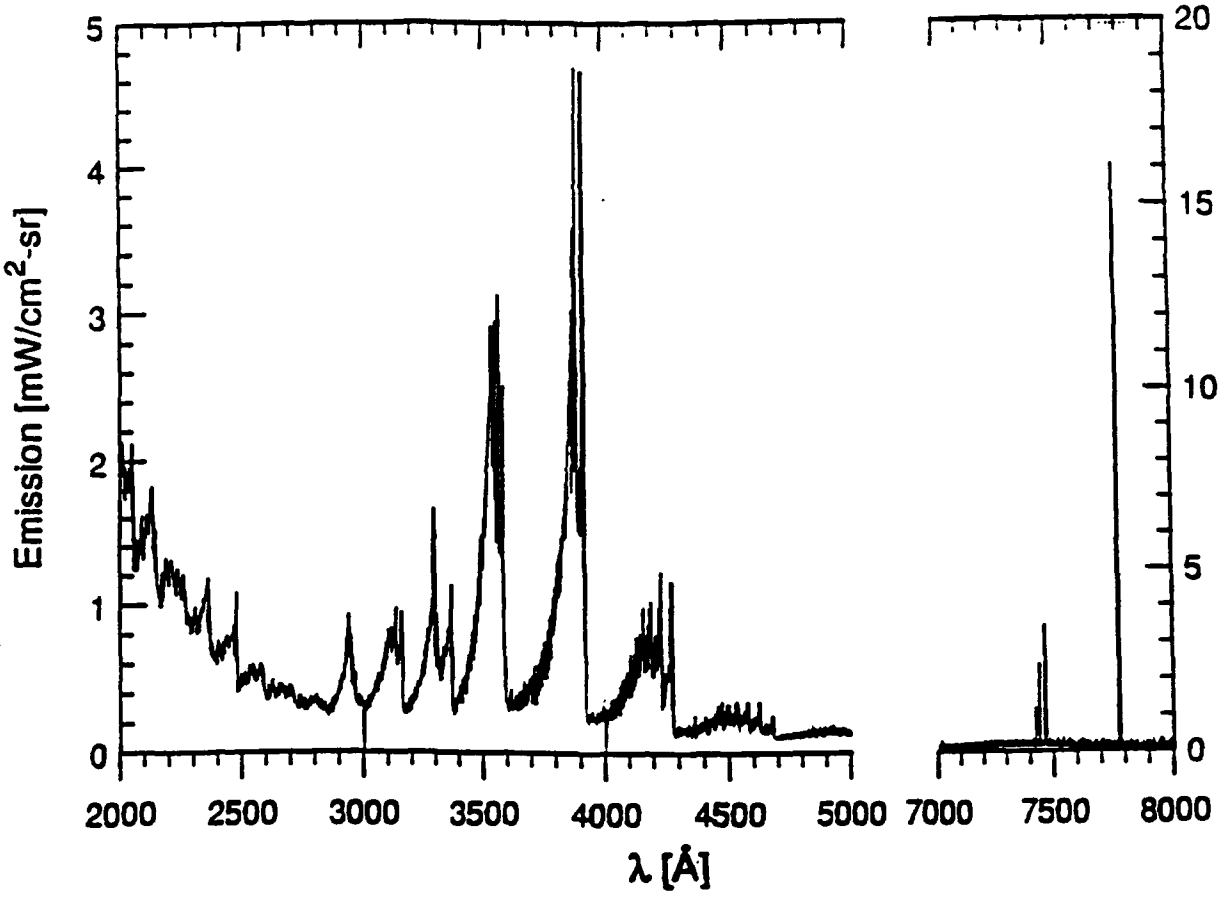

Figure 5.1. Experimental spectrum.

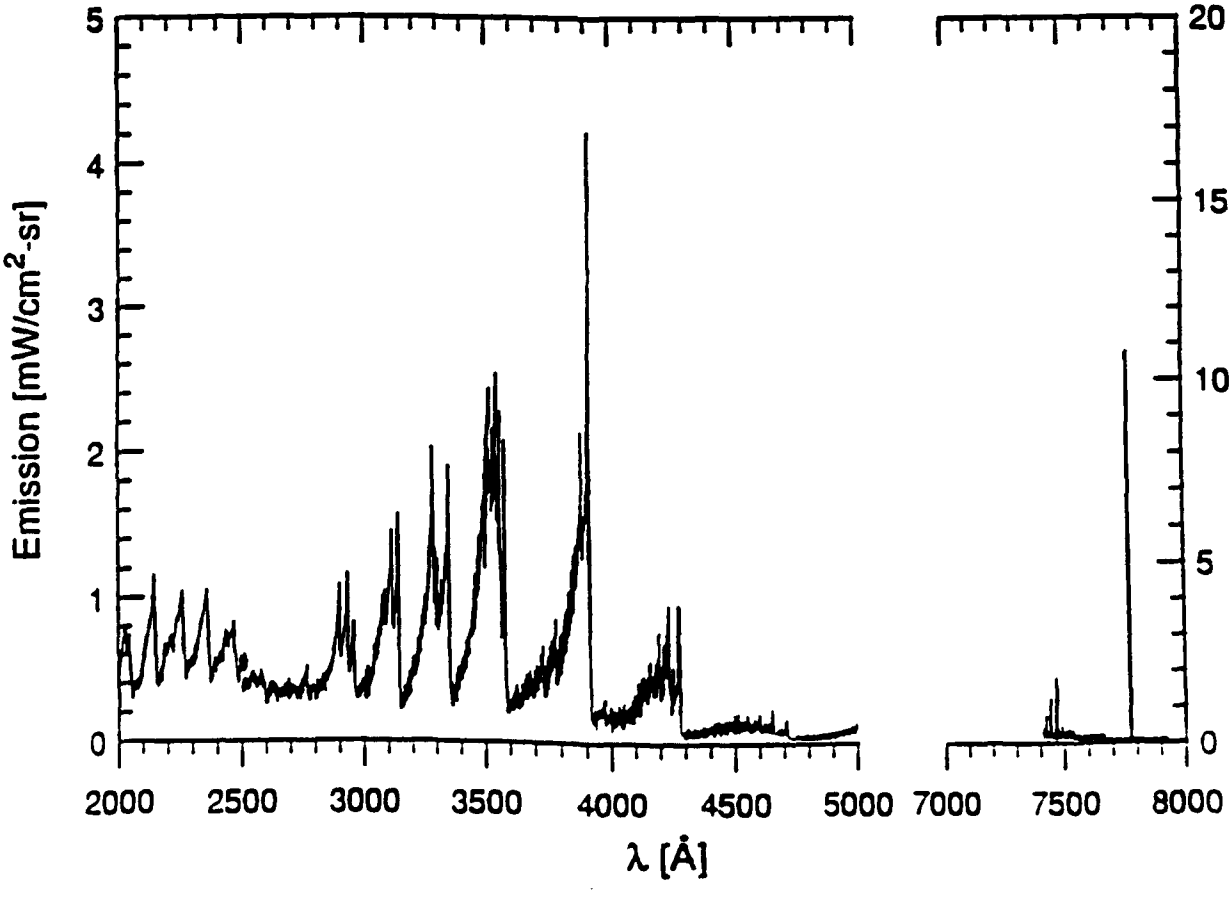

Figure 5.2. Numerical spectrum (*NEQAIR-1*).

5.4. Modeling improvements.

5.4.1. Radiative transition probabilities:

As follows from Eq. 5.1, the emission intensity is proportional to the radiative transition probability $A_{e'v'}^{e''v''}$. This quantity, or equivalently the square of the electronic-vibrational transition moment, $R_e^{v'v''}$, was approximated in *NEQAIR-1* by the product of the Franck-Condon factor, $q_{v'v''}$, times the square of the electronic transition moment, R_e. Since the variations of the latter with internuclear distance, and hence with the vibrational transition, were not known with good accuracy, R_e was taken as a constant in *NEQAIR-1* for all vibrational bands of an electronic system. However, recent progress in computational chemistry has resulted in accurate predictions of the electronic transition moment variations. We used these results to compile reliable transition probabilities for the seven electronic band systems of interest in our temperature and spectral ranges that were included in the original version of *NEQAIR*: the first and second positive systems of N_2, the first negative system of N_2^+, the beta and gamma systems of NO, the Schumann-Runge system of O_2.

A detail account of the transition probabilities calculations is provided below. To make the results applicable to a broader range of applications including optical diagnostics, quantitative spectroscopy and radiation modeling, the computed quantities are the Einstein A coefficients, the band oscillator strengths, the sums of the squared electronic-vibrational transition moments, and the Franck-Condon factors.

5.4.1.a. Definitions and previous results

The key parameter from which transition probabilities are calculated is the square of the electronic-vibrational transition moment

$$\left(R_e^{v'v''}\right)^2 = \left(\int_0^\infty \Psi_{v'}(r) R_e(r) \Psi_{v''}(r) dr\right)^2, \tag{5.6}$$

where v' and v" are the vibrational levels in the upper and lower electronic levels of the transition respectively, $\Psi_{v'}$ and $\Psi_{v''}$ are the corresponding vibrational wavefunctions, r is the internuclear distance, and R_e, the electronic transition moment function (ETMF), is an average of the electric dipole moment with respect to the electronic wavefunctions.

The calculation of transition probabilities therefore depends on the determination of both $R_e(r)$ and the vibrational wavefunctions. Although the latter are routinely calculated, the electronic transition moments have often been inferred from spectroscopic intensity measurements. Such measurements are subject to difficulties associated with gas non-equilibrium, presence of impurities, calibration, and low signal levels for weak transitions. Moreover, the most intense bands span only a

narrow range of internuclear distance r, thus experimental band strengths give very little information about the variation of the electronic transition moment with r. Numerous compilations and reviews of transition probabilities based on these measurements are nevertheless available (Nicholls, 1964 and 1977, Allen, 1966, Schadee, 1967, Kuz'menko et al, 1979).

In recent years, however, electronic transition moment functions for spin-allowed transitions have been obtained by *ab initio* calculations (Werner et al, 1984, Rizzo et al, 1988, Langhoff et al, 1988a, 1988b, 1991, Bauschlicher and Langhoff, 1988). Since these are usually in very good agreement with the few accurate experimental data available, it is then reasonable to calculate reliable transition probabilities. In the present work, we combine these *ab initio* ETMFs with accurate spectroscopic constants to produce extensive arrays of data directly usable in the applications previously mentioned.

5.4.1.b. Method of calculation

The r-centroid approximation (Fraser, 1954, Nicholls and Jarmain, 1955) has been widely used to calculate the integrals of Eq. 5.6. The r-centroid, defined by

$$\bar{r}_{v'v''} = \frac{\int \Psi_{v'} r \Psi_{v''} dr}{\int \Psi_{v'} \Psi_{v''} dr}, \tag{5.7}$$

has such properties that, under a wide range of conditions, the following approximation holds to very good accuracy for low values of n (Nicholls, 1974):

$$\overline{r^n_{v'v''}} = \frac{\int \Psi_{v'} r^n \Psi_{v''} dr}{\int \Psi_{v'} \Psi_{v''} dr} \cong \left(\bar{r}_{v'v''}\right)^n. \tag{5.8}$$

Therefore, when the ETMF varies with the internuclear distance in a polynomial fashion, Eq. 5.6 may be approximated by

$$\left(R_e^{v'v''}\right)^2 \cong \left[R_e\left(\bar{r}_{v'v''}\right)\right]^2 \left[\int \Psi_{v'}(r) \Psi_{v''}(r) dr\right]^2, \tag{5.9}$$

where the second factor on the RHS is the square of the vibrational overlap integral, also called the Franck-Condon factor. The importance of an accurate vibrational analysis is clearly seen from Eq. 5.9, since Franck-Condon factors vary by several orders of magnitude from band to band, whereas electronic transition moments usually change by at most one order of magnitude.

The r-centroid approximation gives very good results for many of the transitions considered in this study, with the possible exception of NO beta for which the ETMF is not perfectly fitted by a low degree polynomial. The method also requires the knowledge of r-centroids and Franck-Condon

factors, which have not always been calculated from the more accurate spectroscopic data now available.

For these reasons, we have instead calculated the integrals of Eq. 5.6 directly. This required modification of an existing Franck-Condon factor program (Zare, 1964). Einstein coefficients, absorption band oscillator strengths, and sums of the electronic-vibrational transition moments are then obtained from (Schadee, 1978):

$$A_{v'v''} = \frac{64\pi^4 \nu^3 \left(2-\delta_{0,\Lambda'+\Lambda''}\right)}{3hc^3\left(2-\delta_{0,\Lambda''}\right)}\left(R_e^{v'v''}\right)^2 = 2.026\times10^{-6}\left(\bar{\nu}_{v'v''}\right)^3 \frac{2-\delta_{0,\Lambda'+\Lambda''}}{2-\delta_{0,\Lambda''}}\left(R_e^{v'v''}\right)^2, \qquad (5.10)$$

$$f_{v'v''}^{abs} = \frac{8\pi^2 m_e \nu \left(2-\delta_{0,\Lambda'+\Lambda''}\right)}{3he^2\left(2-\delta_{0,\Lambda''}\right)}\left(R_e^{v'v''}\right)^2 = 3.0376\times10^{-6}\,\bar{\nu}_{v'v''} \frac{2-\delta_{0,\Lambda'+\Lambda''}}{2-\delta_{0,\Lambda''}}\left(R_e^{v'v''}\right)^2, \qquad (5.11)$$

$$\sum\left(R_e^{v'v''}\right)^2 = \left(2-\delta_{0,\Lambda'+\Lambda''}\right)(2S+1)\left(R_e^{v'v''}\right)^2, \qquad (5.12)$$

provided that the ETMFs have been calculated following the convention of Whiting et al (1980). In the preceding numerical expressions, $\bar{\nu}_{v'v''}$ is the wavenumber in cm^{-1}, $R_e^{v'v''}$ the electronic-vibrational transition moment in atomic units (ea_0), and $\delta_{i,j}$ the Kronecker delta, which is equal to 1 if i=j and 0 otherwise; (2S+1) is the spin multiplicity and Λ the projected spin angular momentum equal to 0, 1, 2, ... for Σ, Π, Δ,... states, respectively.

In addition, emission band oscillator strengths may be calculated from the absorption strengths:

$$f_{v'v''}^{emis} = \frac{2-\delta_{0,\Lambda''}}{2-\delta_{0,\Lambda'}} f_{v'v''}^{abs}. \qquad (5.13)$$

5.4.1.c. Vibrational analysis

The vibrational wavefunctions are constructed from the numerical solution of the radial Schrödinger equation of nuclear motion (Cooley, 1961). An existing program (Zare, 1964) was used to calculate rotationless Rydberg-Klein-Rees potentials based on Dunham expansion coefficients Y_{ij}. The program requires only Y_{i0} and Y_{i1} to obtain

$$G(v) = \sum_{i=1}^{n} Y_{i0}\left(v+\tfrac{1}{2}\right)^i, \text{ and } B_v = \sum_{i=0}^{n} Y_{i1}\left(v+\tfrac{1}{2}\right)^i. \qquad (5.14)$$

As pointed out earlier, special attention must be paid to the spectroscopic constants Y_{ij} that enter the construction of the potentials. Lavrov (1991) recently published a review of such constants for O_2, N_2 and NO. For N_2, however, we used the latest results of Roux and Michaud (1990) and Roux et al (1992). For N_2^+, the values were taken from Klynning and Pagès (1982), and for CN, from Rehfuss et al. (1992) and Prasad et al. (1992).

5.4.1.d. Electronic transition moments

N_2 First positive system $B\,^3\Pi_g$— $A\,^3\Sigma_u^+$

The ETMF from Werner et al (1984) was preferred over the one from Rizzo et al (1988) since it yields radiative lifetimes that agree better with the experimental values summarized in Werner et al (1984), Table IX. Piper et al (1989) inferred Einstein coefficients by combining their experimental transition moment variation with the radiative lifetimes measured by Eyler and Pipkin (1983) for v' = 5 to 12; this procedure enabled them to determine the lifetimes of the levels v' = 0 to 4, and these further support the ETMF from Werner et al (1984). Finally, recent lifetime measurements (1988) for the v' = 0 level yielded a value of 13 ± 1 μs as compared to 13.5 μs when using the ETMF from Werner et al (1984) vs. 9.8 μs with the one from Rizzo et al (1988). The quoted uncertainty on the ETMF is 5%, and thus should result in 10% accuracy for transition probabilities.

N_2 Second positive system $C\,^3\Pi_u$— $B\,^3\Pi_g$

Werner et al (1984) calculated an ETMF that gives excellent agreement with the measured radiative lifetimes presented in their Table VIII. As for the first positive system, resulting transition probabilities should be accurate within 10%.

N_2^+ First negative system $B\,^2\Sigma_u^+$— $X\,^2\Sigma_g^+$

The ETMF calculated by Langhoff and Bauschlicher (1988) agrees very well with the experimental Einstein coefficients of Johnson and Fowler (1970), as may be seen in Table VII of Langhoff and Bauschlicher (1988). The presently calculated transition probabilities are in even closer agreement because updated spectroscopic constants are used in the vibrational analysis.

NO Beta system $B\,^2\Pi_r$— $X\,^2\Pi_r$

The ETMF of the NO beta system is more difficult to determine because of the strong coupling of the transition upper state with the neighboring $C\,^2\Pi$ state. The most reliable ETMF was obtained by Langhoff et al (1991). The resulting lifetimes are somewhat higher than the experimental values of Gadd and Slanger (1990) for v' = 0 to 6. However, once rescaled by the ratio of the experimental to the theoretical lifetimes, the calculated transition probabilities are within a few percent of the values measured by Piper et al (1991) for v' = 0 to 5. For v' = 6, two sets of experimental transition probabilities are available (Gadd and Slanger, 1990, Piper et al, 1991). While the two sets are in good agreement (better than 10%) for the most intense bands, larger discrepancies exist for the weaker bands. The present calculated Einstein coefficients, once rescaled by the ratio of lifetimes, fall however between the two sets. Langhoff et al (1991) suggested that the differences may be partially attributed to calibration problems since no smooth ETMF can match both the lifetimes and

the transition probabilities of Gadd and Slanger (1990).

For levels above v'=6, our calculated transition probabilities can only be regarded as approximate because of the increasing influence of vibrational-rotational interactions (Langhoff et al, 1991, Gadd et al, 1991).

NO Gamma system $A\,^2\Sigma^+ — X\,^2\Pi_r$

The ETMF used here is the (344)MRCI(7electrons) of Langhoff et al (1988). The calculated transition probabilities are within 10% of those measured by Piper and Cowles (1986) for the bands originating from v' = 0, 1 and 2.

O_2 Schumann-Runge system $B\,^3\Sigma_u^- — X\,^3\Sigma_g^-$

Transition probabilities for the O_2 Schumann-Runge are obtained with the semi-empirical ETMF defined by Friedmann (1990), which is based on the results of Allison et al (1986). The present calculations agree very well with the experimental mean oscillator strengths of Lewis et al (1986).

CN Violet system $B\,^3\Sigma_u^- — X\,^3\Sigma_g^-$

The transition probabilities of the CN violet system are computed using the electronic transition moment of Bauschlicher and Langhoff (1988).

5.4.1.e. Results

Tables of Einstein A coefficients, absorption band oscillator strengths, and sums of the electronic-vibrational transition moments are given for each of the systems previously mentioned. Franck-Condon factor arrays hare also been computed so that comparisons can be made with other sets of experimental transition probabilities obtained with different Franck-Condon factors. Finally, tables of wavelengths and *r*-centroids have also been prepared. All tables are available in the computer diskette attached to this report..

The 1,500 or so updated transition probabilities that were introduced into the new version of the *NEQAIR* code have resulted in intensity changes of about -10% for the first negative system of N_2^+ and the second positive systems of N_2,-15% for the first positive system of N_2, -25% for NO beta, +300% for NO gamma, +250% for the Schumann-Runge system of O_2, and a factor 10 increase for the Violet system of CN (these values are for the global power emitted between 2,000 and 20,000 Å by a plasma in LTE at 8,000 K, and are virtually constant over at least the range 4,000-8,000 K).

5.4.2. Spectroscopic constants:

Predicting line positions accurately is of special importance when trying to match experimental measurements to gain information on populations or temperatures, or when absorption calculations are required. Line positions are determined from the difference of energy between the levels of the transition,

$$\Delta T = \Delta T_e + \Delta G(\mathrm{v}) + \Delta F_\mathrm{v}(J) \tag{5.15}$$

where T_e, $G(\mathrm{v})$, and $F_\mathrm{v}(J)$ are the electronic, vibrational, and rotational term energies respectively. $G(\mathrm{v})$ is itself defined as

$$G(\mathrm{v}) = \omega_e\left(\mathrm{v}+\tfrac{1}{2}\right) - \omega_e x_e\left(\mathrm{v}+\tfrac{1}{2}\right)^2 + \omega_e y_e\left(\mathrm{v}+\tfrac{1}{2}\right)^3 + \omega_e z_e\left(\mathrm{v}+\tfrac{1}{2}\right)^4 + \ldots \tag{5.16}$$

and $F_\mathrm{v}(J)$ as

$$F_\mathrm{v}(J) = B_\mathrm{v} J(J+1) - D_\mathrm{v} J^2 (J+1)^2 + \ldots, \tag{5.17}$$

where

$$B_\mathrm{v} = B_e\left(\mathrm{v}+\tfrac{1}{2}\right) - \alpha_e\left(\mathrm{v}+\tfrac{1}{2}\right)^2 + \gamma_e\left(\mathrm{v}+\tfrac{1}{2}\right)^3 + \delta_e\left(\mathrm{v}+\tfrac{1}{2}\right)^4 + \ldots, \tag{5.18}$$

$$D_\mathrm{v} = D_e\left(\mathrm{v}+\tfrac{1}{2}\right) + \beta_e\left(\mathrm{v}+\tfrac{1}{2}\right)^2 + \ldots . \tag{5.19}$$

Improved electronic term energies (T_e) and Klein-Dunham coefficients (ω_e, $\omega_e x_e$,..., B_e, α_e, D_e, β_e,...), based on accurate data from Fourier transform spectroscopy, have been included into *NEQAIR-2*; they are tabulated and referenced in Appendix C1. Since these spectroscopic constants were obtained by polynomial fits of experimental line positions, it is essential, when using such developments, to include the same number of polynomial terms as in the original fit. *NEQAIR-1*, which was limited to 3 terms in each development, was modified to include all necessary coefficients. The resulting effect is quite drastic for the vibrational bands of the second positive system of N_2 (Fig. 5.3): the large shift of about 30 Å in band positions in *NEQAIR-1* was due to the neglecting of $\omega_e z_e$ in Eq. 5.16.

Figure 5.3 Effect of improved spectroscopic constants on the N_2 Second positive system.

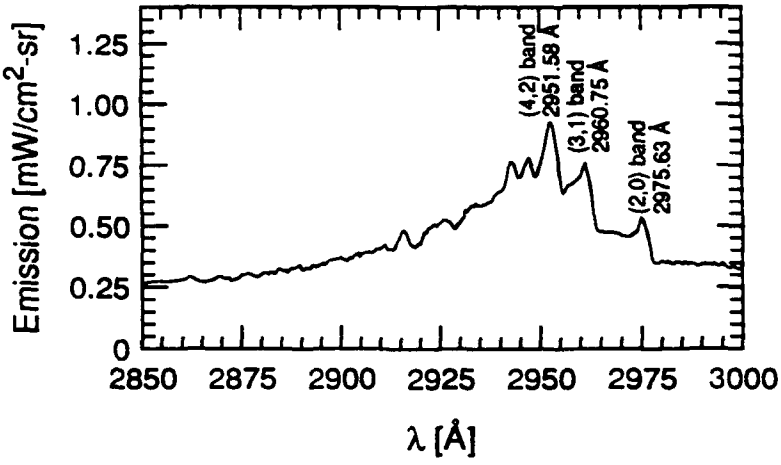

Figure 5.3a. Experimental spectrum

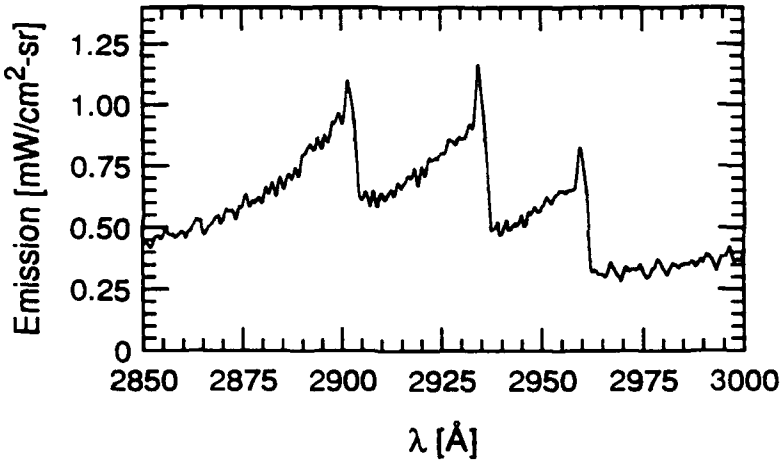

Figure 5.3b. Numerical spectrum (*NEQAIR-1*).

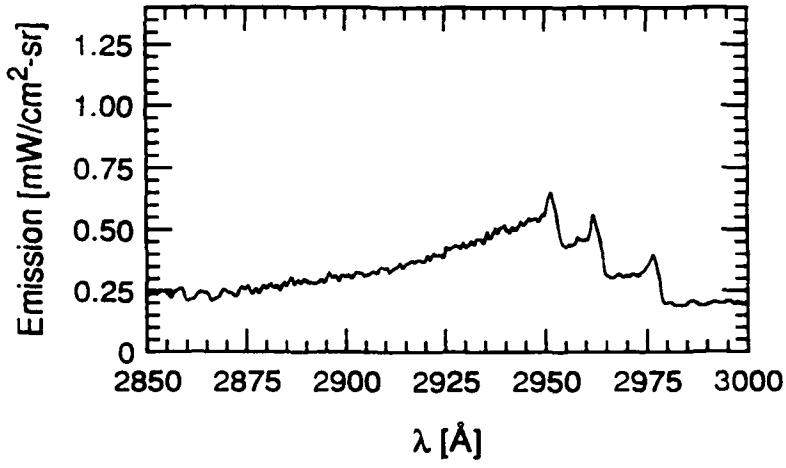

Figure 5.3c. Numerical spectrum (*NEQAIR-2*).

5.4.3. Additional bands:

The spectral region below 2,800 Å, where the electronic systems of NO are the dominant radiators, is of particular interest for ultra-violet signatures. It appeared in the course of this work that the numerical spectrum failed to reproduce the experimental one, even after updating the transition probabilities for NO Beta and Gamma (see Fig. 5.4a). We therefore considered additional electronic systems of NO, including the Delta, Epsilon, Beta prime, and Gamma prime. The positions of the emitting levels for these transitions are sketched in Fig. 5.5. The electronic level C (upper of the Delta transition), is strongly predissociated above v'=0, J'>4.5 (see for example Gadd et al., 1991) due to interferences with the $a^4\Pi$ state, but the other levels are not subject to predissociation. We present first the addition of the non-predissociated levels, and then the contribution of NO Delta.

5.4.3.a. NO Epsilon (D→ X):

The radiative transition probabilities for this system were obtained from the electronic transition moment computed by De Vivie and Peyerimhoff (1988), and from potential curves based on the spectroscopic constants of Huber and Herzberg (1979) and Amiot (1982). However, while computational chemistry usually predicts the correct variation of the electronic transition moment with internuclear distance, experimental studies produce more accurate values of its absolute magnitude. For this reason, the radiative lifetime of the v'=0 state was matched to the radiative lifetime measured by Tsukiyama et al. (1988), and the transition probabilities were normalized accordingly.

As shown in Fig. 5.4b, the NO Epsilon bands contribute significantly to the radiation in the range 2,000-2,500 Å . In particular, the "stair-case" structure of the experimental spectrum in that region is numerically recovered, at least partially, with the introduction of NO Epsilon. Although further studies are needed to predict band intensities with better accuracy, NO Epsilon appears as a major source of radiation in the ultra-violet.

5.4.3.b. NO Beta Prime (B'→ X) and Gamma prime (E→ X):

The radiative transition probabilities for NO Beta prime and Gamma prime were obtained from the electronic transition moments of De Vivie and Peyerimhoff (1988), and from the spectroscopic constants of Huber and Herzberg (1979) and Amiot (1982). These transition probabilities are about one order of magnitude smaller than those of the Delta or Epsilon transition. Moreover, since the emitting levels lie about 1 eV higher in energy than the C or D states, their population is much smaller than those of the C and D states, and the bands lie farther in the vacuum ultra-violet. For these reasons, the NO Beta prime and Gamma prime bands produce a very small amount of radiation in the wavelength and temperature ranges considered here. The missing structures in the computed spectrum of Fig. 5.4b cannot therefore be attributed to these systems.

Figure 5.4. Influence of additional NO bands.

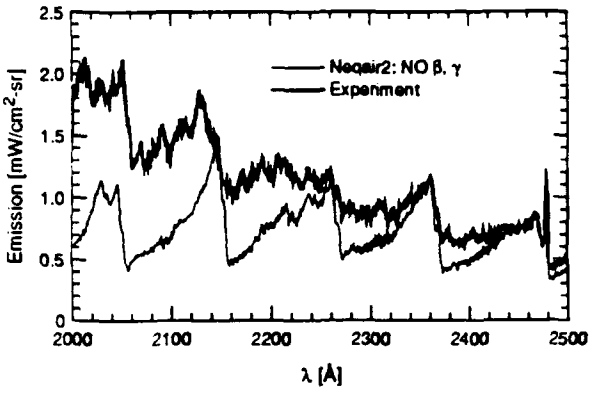

Fig 5.4a. NO Beta and Gamma. Optically thin computations.

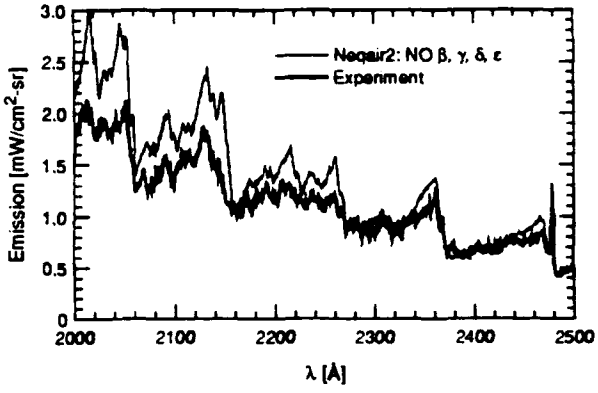

Fig 5.4d. NO Beta, Gamma, Delta, Epsilon with predissociation of C state. Optically thin computations.

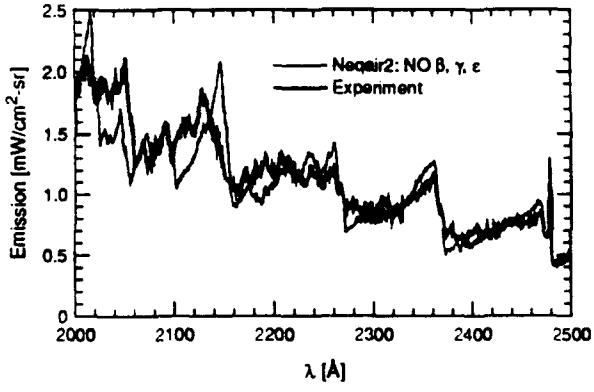

Fig. 5.4b. Addition of NO Epsilon. Optically thin computations.

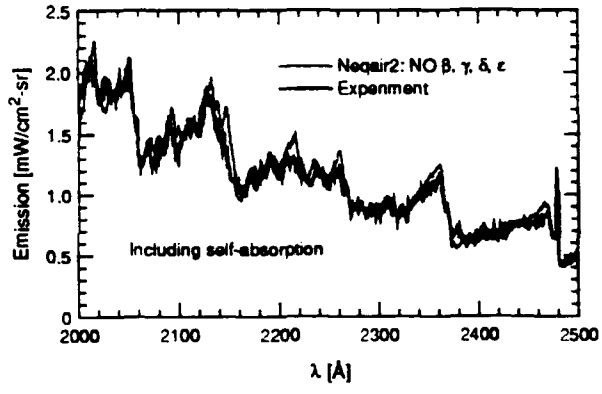

Fig. 5.4e. NO Beta, Gamma, Delta and Epsilon with predissociation of the C state. Including self absorption.

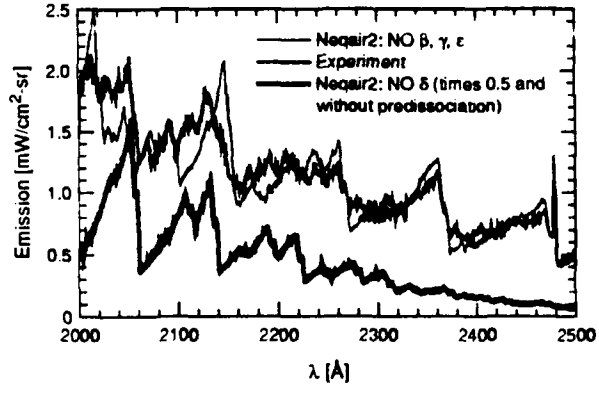

Fig. 5.4c. NO Beta, Gamma, Epsilon and (bottom curve) NO Delta without predissociation. Optically thin computations.

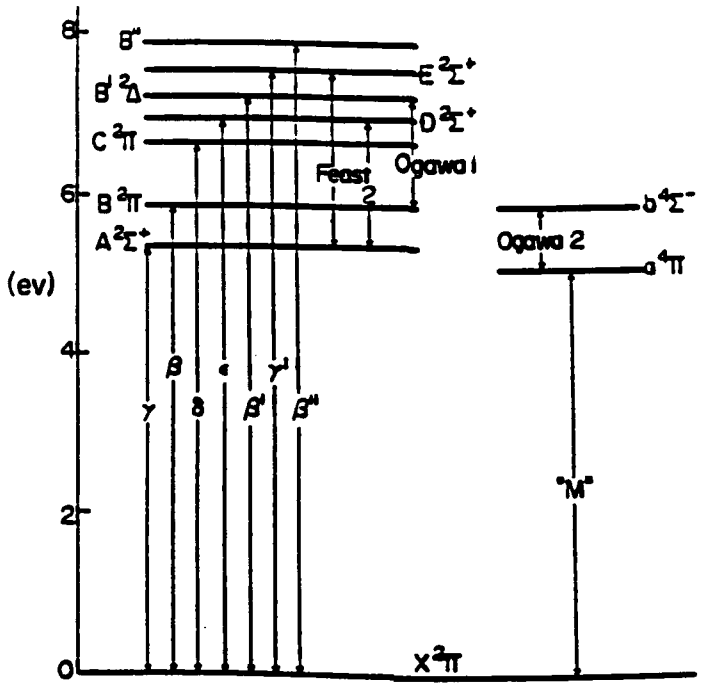

Figure 5.5. NO energy level diagram.

5.4.3.c. NO Delta (C→ X):

The radiative transition probabilities for NO Delta were determined from the electronic transition moments of Cooper (1982) and from the spectroscopic constants of Huber and Herzberg (1979) and Amiot (1982).

As mentioned earlier, the emitting C-level is strongly predissociated. Indeed, if such were not the case, the computed intensity of the Delta band would be much too strong, as may be seen in Fig. 5.4c. It is interesting to note however that the position of the missing features of the numerical spectrum coincide with the strongest Delta bands.

Several authors have measured (Tsukiyama et al., 1987 and 1988, Rottke and Zacharias, 1985, Benoist d'Azy et al., 1975, Hikida et al., 1987, Hart and Bourne, 1989) or computed (DeVivie and Peyerimhoff, 1990) the predissociative lifetimes of individual rotational levels of the C state, and have obtained values on the order of 30 ns for the non-predissociated levels (v=0, J'<5), and between 10 ns and 0.03 ns for the predissociated ones. On the other hand, the kinetic collision time (i.e. the inverse of the collision frequency) by heavy particle impact is on the order of 0.3 ns at 7,000 K and 1 atm. We argue below that, in our high pressure (1 atm) and high temperature experimental conditions, collisional processes compete with predissociation to maintain some population in the predissociated levels.

A complete collisional-radiative model would be required to predict the population of all rota-

tional levels in the C state. Ideally, the following mechanisms would be included:

(a) Rotational relaxation within C state by heavy particle impact (rotational transitions occur through momentum transfer, and electrons are inefficient in transferring momentum[12]).

(b) Collisional excitation and quenching of the C state by heavy particles and electrons.

(c) Recombination of N and O atoms, or NO^+ and electrons to the C state.

(d) Radiative cascading.

(e) Predissociation of the C state.

Such a model is unfortunately out of reach presently for lack of knowledge of most cross sections for the above processes. However, Callear and Pillin (1970) and Lahmani et al (1981) observed fast collisional exchange between the C and the D state in the presence of argon. This is not surprising in light of the proximity of the two levels (the difference of energy between C, v=0, J=0 and D, v=0, J=0 is about 900 cm^{-1}, or about a tenth of an eV). In both studies, the collision rate in the presence of argon was found to be close to the kinetic collision rate. Le Duff et al. (1986) observed the same phenomenon in the presence of other atomic gases (rare gases). On the other hand, molecular gases were found to be much less efficient quenchers (Callear and Pilling, 1970). In our experiment, however, the plasma in the region of intense radiative emission is mainly composed of atomic species (N and O) —the total mole fraction of atoms is over 0.90 at 7,000 K.

Therefore, considering only predissociation and collisions with the D state by heavy particle impact, i.e.

$$NO\,(C,\ v,\ J) + M \leftrightarrow NO(D, v', J') + M,$$

where M is a heavy particle (atom), the population evolution of a given rotational level J in the C state is given by:

$$\frac{dN_J}{dt} = -N_J\left(k^J_{pred} + \sum_{J'} N_M S^{J\to J'}\right) + \sum_{J'} N_{J'} N_M S^{J'\to J} \tag{5.20}$$

where $S^{J\to J'}$ is the collisional excitation rate of the J level, $S^{J'\to J}$ its reverse, and N_M the concentration of heavy particles.

Using detailed balance, the reverse rate can be expressed as

$$S^{J'\to J} = \frac{(N_J)^{LTE}}{(N_{J'})^{LTE}} S^{J\to J'}. \tag{5.21}$$

Assuming that the D level which is not subject to predissociation (see for instance Callear and Pilling, 1970) remains in LTE, and assuming quasi-steady state, Eq. 5.20 becomes:

$$\frac{N_J}{(N_J)^{LTE}} = \frac{\sum_{J'} N_M S^{J\to J'}}{k^J_{pred} + \sum_{J'} N_M S^{J\to J'}} \tag{5.22}$$

or, assuming unit efficiency for heavy particle collisions as suggested by Callear et Pilling (1970):

$$\frac{N_J}{(N_J)^{LTE}} \equiv \frac{k_{collisions}}{k^J_{pred} + k_{collisions}}. \tag{5.23}$$

The collision frequency was approximated by (Vincenti and Kruger, 1965):

$$k_{collisions}\left[\sec^{-1}\right] \equiv 10^{10}\sqrt{\frac{T[K]}{298}}\,P[atm], \tag{5.24}$$

and the values k^J_{pred} were obtained from a fit of the few available experimental and theoretical predissociation data (Fig. 5.6). Because of spin interaction, each rotational level J is split into Ω=1/2 and Ω=3/2 substates. Fig 5.6 shows that the Ω=1/2 components have a much shorter predissociative lifetime than the Ω=3/2 component above the predissociation limit. For this reason, all emission from Ω=1/2 above J=4.5 was neglected.

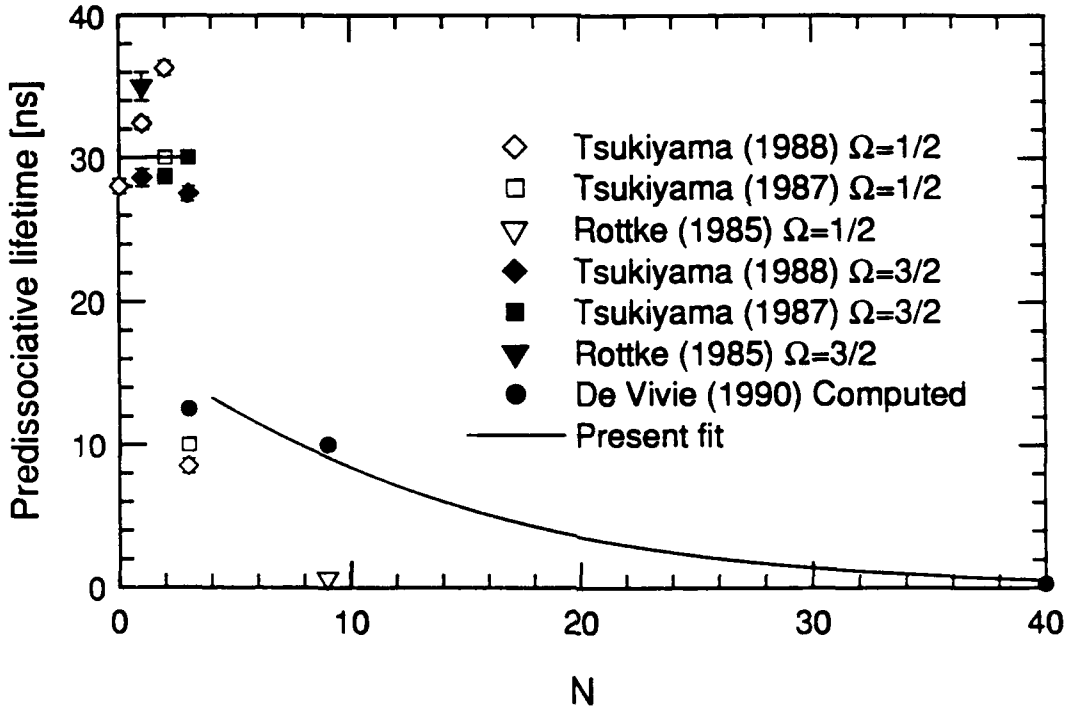

Figure 5.6. Predissociative lifetimes of the rotational levels of the C state of NO (v'=0).

The numerical spectrum predicted by *NEQAIR-2*, with this simplified collision-predissociation model included, is presented in Fig 5.4d. All previously missing features in the computed spectrum are numerically recovered with the simple model developed above. The absolute magnitude of the new spectrum is however a little larger than in the experiment, but self-absorption by the plasma

should be considered. As may be seen in Fig. 5.4e, including self-absorption leads to excellent agreement in shape and absolute intensity between the experimental and numerical spectra.

Of course, more effort is needed to predict accurately the radiation due to NO Delta and Epsilon. Among the most important data required for the collision-predissociation model are better estimates of

(a) predissociation rates for the rotational levels of the C state,

(b) collisional excitation cross-sections between the C and the D states,

(c) radiative transition probabilities for the Delta and Epsilon transitions.

5.5. Comparison with *NEQAIR-2*.

The final comparison between experiment and improved computations is shown in Fig. 5.7. Much better agreement is now obtained for the shape, position, and intensity of the molecular bands. The additional Delta and Epsilon bands of NO have significant effect in the ultra-violet region which is now well reproduced numerically. The addition of NO Beta prime and Gamma prime bands has a negligible incidence on the spectrum presented in Fig. 5.7, but would have more importance in the spectral region below 2,000 Å, where the most intense bands lie, or at higher temperatures where the emitting levels are more populated. The position of the N_2 Second positive bands has been improved; their intensity, too high by a factor 2 in *NEQAIR-1*, was corrected by the addition of the homonuclear factor in partition functions calculations as described by Moreau et al (1992). The CN Violet bands now appear with their correct intensity. Finally, the intensities of the nitrogen and oxygen triplets are closer to the measurements. This change is not due to any physical improvement, but rather to a higher numerical resolution: *NEQAIR-1* used constant wavenumber spacing instead of constant wavelength spacing and therefore few spectral points were considered at long wavelengths.

Some spectral features still appear underpredicted by *NEQAIR-2* (N_2^+ (0,0) band at 3,911 Å, some N_2 bands, and the O and N triplets). These differences (about 20 %) are however within modeling and experimental uncertainties. In any case, predicting the intensity of the oxygen triplet at 7,773 Å with 10 % accuracy would require the temperature to be measured with 0.5 % accuracy. The remaining intensity differences are therefore not significant.

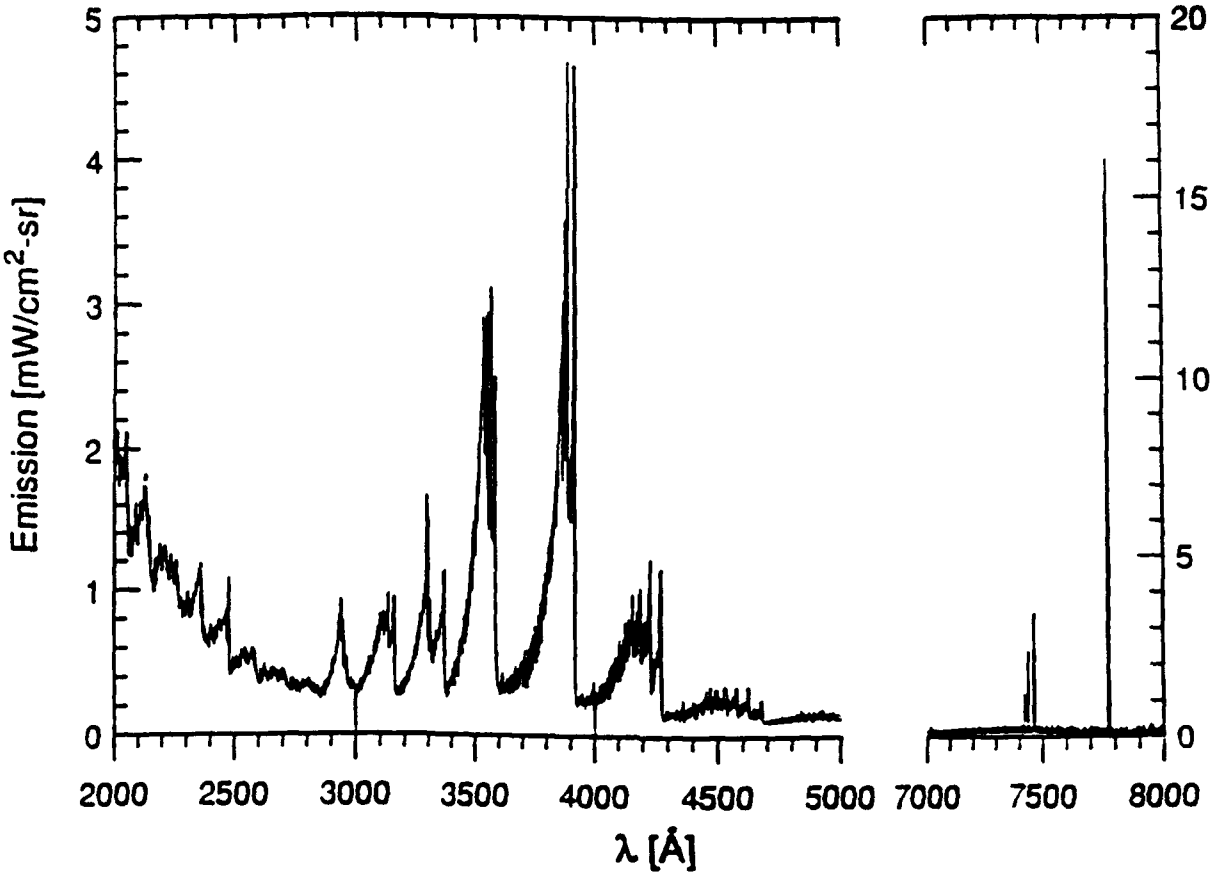

Figure 5.7a. Experimental spectrum.

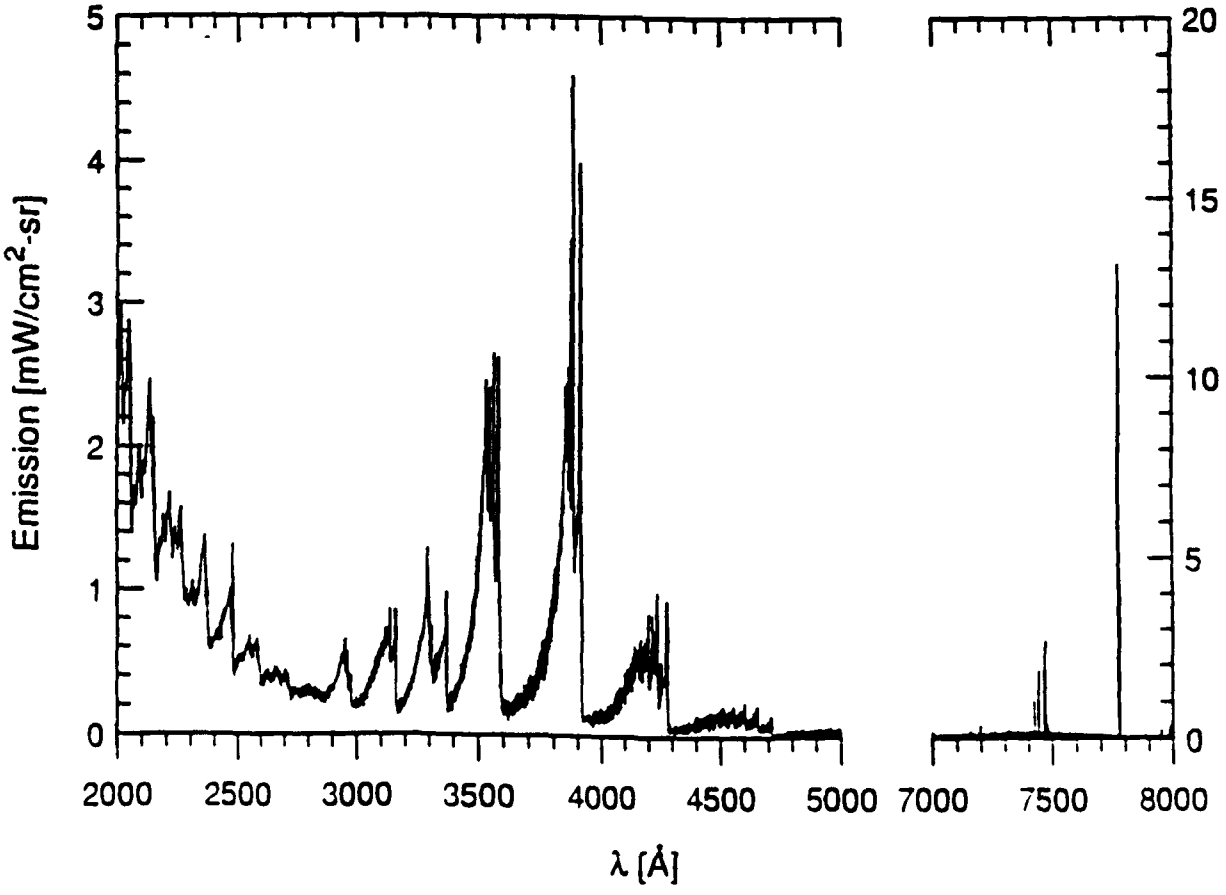

Figure 5.7b. Numerical spectrum (*NEQAIR-2*).

6. Radiative source strength of air plasmas

For atmospheric pressure air at temperatures above 9,000 K, measurements of the radiation source strength, or local emissivity, have been reported by several authors, including Page and Arnold (1964), Nerem (1964), Schreiber et al. (1973), Ogurtsova et al. (1968), and Devoto et al. (1978). These experiments were conducted in shock tubes (Page et al., Nerem), or in arc discharges (Schreiber et al., Ogurtsova et al., Devoto et al.). The emitted radiation was recorded by thermopiles and calibrated with tungsten lamps. Temperatures were determined under the LTE assumption from the absolute intensity of atomic oxygen and nitrogen lines.

In addition, several theoretical models have been developed over the past decades (Kivel and Bailey, 1957, Meyerott et al., 1960, Breene et al., 1963, and Park, 1985). A comparison between the measurements and the predictions from of the codes is presented in Fig. 6.1. The curve labeled as *NEQAIR-2* includes the changes described in the previous sections.

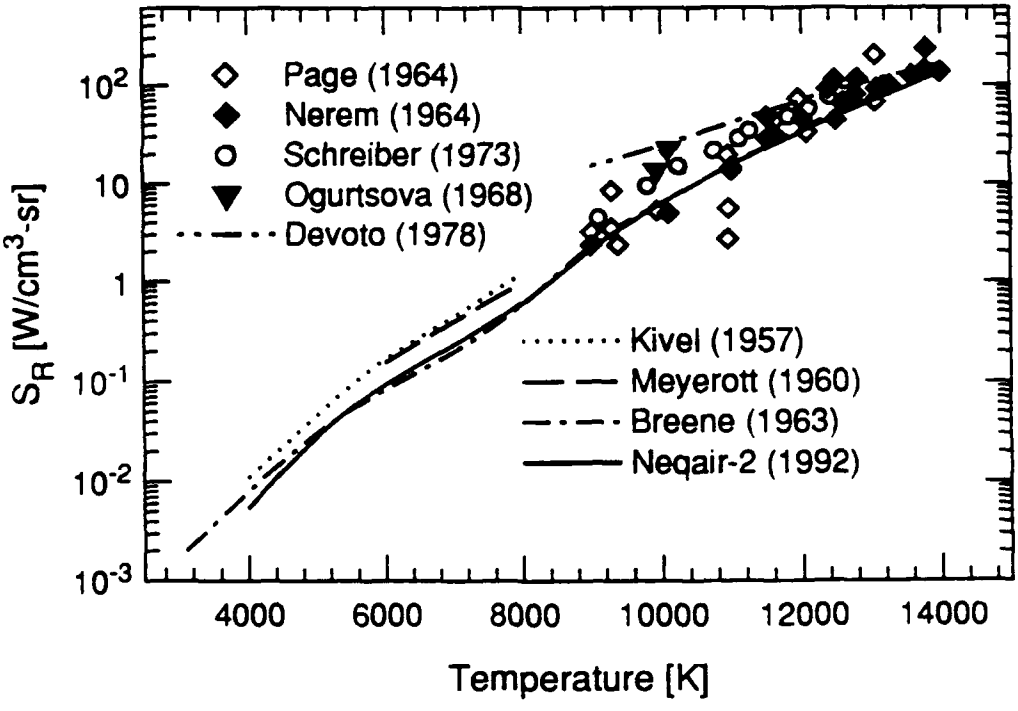

Figure 6.1 Volumetric radiative source strength of LTE air at atmospheric pressure: previous results and enhanced NEQAIR-2 computations.

The measurements conducted during the course of this work cover the range 4,000 to 8,000 K and are, to our knowledge, the first measurements in that temperature range. The radiation source strength, or local emissivity, as a function of lateral position was measured as described in Section 3.

The lateral emission profile was then corrected for plasma self-absorption using the following procedure. The plasma was modeled using the LTE temperature profile, corrected for self absorption, measured in Section 4. The lateral spectrally integrated emission profile was computed for both optically thin and self-absorbed cases using the enhanced version of the *NEQAIR* code, *NEQAIR-2*. The measured profile of spectrally integrated emission, thereby corrected for self absorption effects, was then Abel-inverted and reduced to volumetric radiative source strength. It should be noted here that the self-absorption correction is on the order of about 10%. Finally, the spectrally integrated radiation was plotted against the self-absorption corrected LTE temperature from the 7,773 Å oxygen line. The resulting radiation source strength profile is presented in Figure 6.2, where it is compared to the predictions of the aforementioned codes. In all cases, the spectral range extends from 2,000 to 20,000 Å.

While the early models overestimate the radiative source strength, the enhanced code *NEQAIR-2* agrees closely with the present measurements.

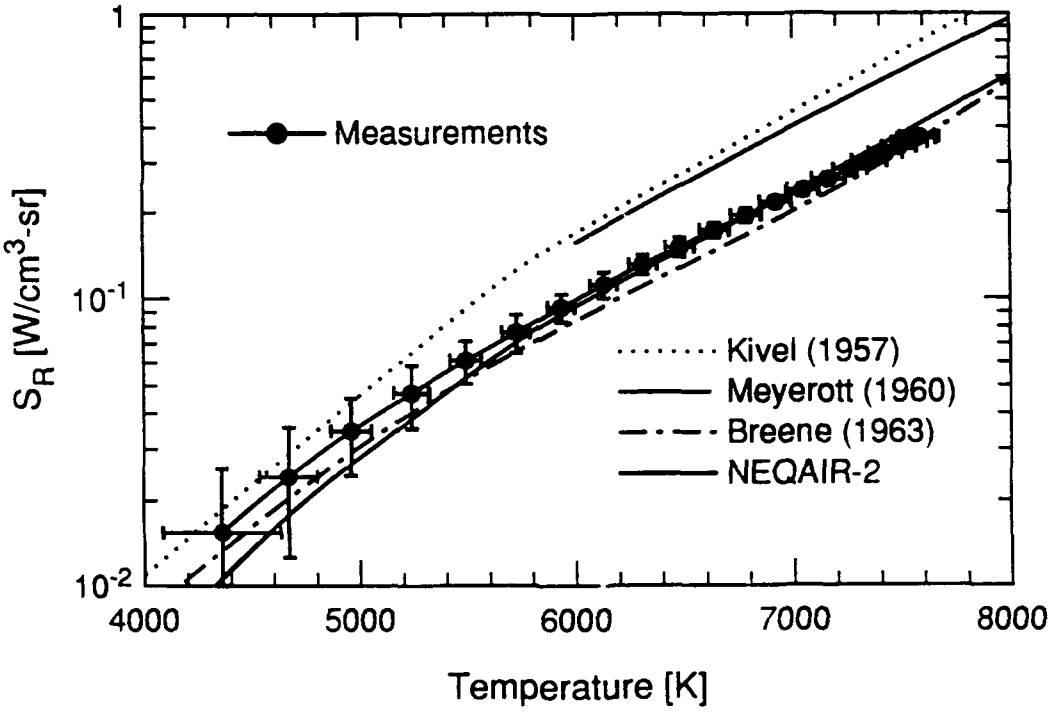

Figure 6.2 Volumetric radiative source strength of LTE air at atmospheric pressure: comparison between our experimental results and the predictions of numerical codes.

7. Conclusions

Optical diagnostics were conducted in an atmospheric pressure plasma torch operating on air in the purpose of studying fundamental plasma processes. The first task consisted in determining the thermodynamic state of the air plasma through atomic and molecular emission spectroscopy. The plasma was found to be close to Local Thermodynamic Equilibrium, and composition and temperature profiles were determined. The spectrum emitted by the air plasma over the spectral range 2,000 to 8,000 Å was then compared to the LTE predictions of the *NEQAIR* code. This comparison led to a number of improvements to the radiative model of the code. In particular, the transition probabilities and spectroscopic constants of the main radiating systems were updated, and additional electronic systems were included in the code. A data base was constituted for several band systems including the First and Second positive systems of N_2, the First negative system of N_2^+, the Beta, Gamma, Delta, Epsilon, Beta prime and Gamma prime systems of NO, the Schumann-Runge system of O_2, and the Violet system of CN. Among the new electronic systems introduced in the code, NO Delta and Epsilon were found to be especially strong radiators in the ultra-violet. A collision-predissociation model for the NO C-state from which the Delta transition originates is however necessary, and a simplified such model has been presented. After the modeling changes, excellent agreement in shape and absolute intensity is obtained between the experimental and numerical spectra. The radiative module of *NEQAIR-2* now predicts radiative intensities within 20% accuracy for most bands over at least the spectral range 2,000-8,000 Å. Finally, the radiation source strength, or local emissivity, was measured for the first time over the temperature range 4,000 to 8,000 K. The predictions of the enhanced *NEQAIR* code are found to be within modeling and experimental error of our source strength measurements.

8. References:

Albritton, D.L., Schmeltekopf, A.L., and Zare, R.N., unpublished results, private communication with R.N. Zare, Chemistry Department, Stanford, CA 94305-5080, 1991.

Allen, R.A., "Air Radiation Tables," *NASA CR-557*, Scientific and Technical Information Division, National Aeronautics and Space Administration, Washington, DC 20546, August 1966.

Allison, A.C., Guberman, S.L., and Dalgarno, A., "A model of the Schumann-Runge continuum of O_2," *J. Geophys. Res.* **91**, 10193, 1986.

Amiot, C., "The infrared emission spectrum of NO: Analysis of the $\Delta v=3$ sequence up to v=22," *J. Molec. Spectrosc.*, **94**, 150, 1982.

Bauschlicher, C.W. and Langhoff, S.R., "Theoretical study of the dissociation energy and the red and violet band systems of CN," *Astrophys. J.*, **332**, 531, 1988.

Benoist d'Azy, O., Lopez-Delgado, R., and Tramer, A., "NO fluorescence decay from low-lying electronic states excited into single vibronic levels with synchrotron radiation," *Chem. Phys.*, **9**, 327, 1975.

Biberman, L.M., Norman, G.E., and Ulyanov, K.N., *Kinetics of Nonequilibrium Low-Temperature Plasmas*, Consultants Bureau. New York, 1987.

Boulos, M., Fauchais, P., and Pfender E., "Diagnostic Techniques in Thermal Plasma Processing," *DOE/ER-0270*, US Department of Energy, Office of Energy Research, Office of Basic Energy Sciences, Washington, DC 20585, 1986.

Breene, R.G., Nardonne, M., Riethof, T.R., and Zeldin, S.S., "Spectral Radiance of Chemicals in High Temperature Air," *R-63SD3*, General Electric Space Sciences Laboratory, Philadelphia, PA, 1963.

Callear, A.B. and Pilling, M.J., "Fluorescence of Nitric Oxide. Part 6," *Trans. Faraday Soc.*, **66**, 1886, 1986.

Chase, J.D., *J. Appl. Phys.*, **42**, 4870, 1971.

Cooley, J.W., "An improved eigenvalue corrector formula for solving the Schrödinger equation for central fields," *Math. Comp.* **15**, 363, 1961.

Cooper, D.M., "Theoretical study of IR band intensities and electronic transition moments for the b and d systems of NO," *JQSRT*, **27**, 459, 1982.

Davies, J. and Simpson, P, *Induction Heating Handbook*, London, New-York: McGraw-Hill, 1979.

DeVivie, R. and Peyerimhoff, S.D., "Theoretical spectroscopy of the NO radical. I. Potential curves and lifetimes of excited states," *J. Chem. Phys.*, **89**, 3028, 1988.

DeVivie, R., Peyerimhoff, S.D., "Theoretical spectroscopy of the NO radical. III. Λ doubling and predissociation in the C state," *J.Chem.Phys.*, **92**, 3613, 1990.

Devoto, R.S., Bauder, U.H., Cailleteau, J., and Shires, E., "Air transport coefficients from electric arc measurements," *Phys. Fluids*, **21**, 552-558, 1978.

Drayson, *JQSRT*, **16**, 611-614, 1976.

Dresvin, S.V., Donskoi, A.V., Gol'dfarb, V.M., and Klubnikin, V.S., *Physics and Technology of Low-Temperature Plasmas*, 1972, S.V. Dresvin, Editor. English edition translated by T. Cheron and edited by H.V. Eckert. Iowa State University Press / Ames, 1977.

Eckert, H.U., *J. Appl. Phys.*, **42**, 3108, 1971.

Erdman, P.W., Zipf, E.C., Espy, P.J., Howlett, C., Levin, D.A., Collins, R.J., and Candler, G.V., "Measurements of ultraviolet radiation from a 5 km/sec bow shock," *AIAA-92-2870*, 1992.

Eyler, E.E. and Pipkin, F.M., "Lifetime measurements of the $B^3\Pi_g$ state of N_2 using laser excitation," *J. Chem. Phys.* **79**, 3654, 1983.

Fraser, P.A., "A method for determining the electronic transition moment for diatomic molecules," *Can. J. Phys.* **32**, 515, 1954.

Freeman, M.P., and Chase, J.D., "Energy transfer mechanism and typical operating characteristics for the thermal rf plasma generator," *J. Appl. Phys.*, **39**, 180, 1968.

Friedman, R.S., "Oscillator strengths of the Schumann-Runge bands of isotopic oxygen molecules," *JQSRT* **43**, 225, 1990.

Gadd, G.E. and Slanger, T.G., "NO($B^2\Pi$) radiative lifetimes: v=0-6," *J.Chem. Phys.* **92**, 2194, 1990.

Gadd, G.E., Huestis, D.L., Slanger, T.G., "Rotational-level-dependent radiative lifetimes and

branching ratios in NO($B^2\Pi$) (v=7, Ω=1/2,3/2)," *J. Chem. Phys.*, **95**, 3944, 1991.

Gallusser, R. and Dressler, K., "Multistate vibronic coupling between the excited $^2\Pi$ state of the NO molecule," *J. Chem. Phys.* **76**, 4311, 1982.

Gol'dfarb, V. and Dresvin, S.V., *Teplofiz. Vys. Temp.*, **3**, 333, 1965.

Gomès, A.M., Bacri, J., Sarrette, J.P., Salon, J., "Measurement of heavy particle temperature in a RF air discharge at atmospheric pressure from the numerical simulation of the NOγ system," *Journal of Analytical Atomic Spectroscopy*, in press 1992.

Gordon, M.H., "Non-Equilibrium Effects in a Thermal Plasma," Ph.D. Dissertation, Department of Mechanical Engineering, Stanford University, Stanford, CA 94305, February 1992.

Goykhman, V.K. et al., *Physics, Technology and Application of a Low-Temperature Plasma*, Alma-Ata, Kazakh. Ped. Inst., Proceedings IV Allunion Conf. Phys. and Generators of Low-Temperature Plasma (See Dresvin et al., 1977, p 196), 1970.

Griem, H.R., *Plasma Spectroscopy*, McGraw-Hill Book Company, New York, 1964.

Hart, D.J. and Bourne, O.L., "High resolution coherent VUV spectroscopy of NO [$C^2\Pi(1)$, $B^2\Pi$ (10), $B^2\Pi$ (11)], and CO[$B^1\Sigma^+(0)$]," *Chem. Phys.*, **133**, 103, 1989.

Hikida, T., Suzuki, T., and Mori, Y., *Chem. Phys.*, **118**, 437, 1987.

Huber, K.P. and Herzberg, G., *Molecular spectra and Molecular structure. IV. Constants of diatomic molecules*, Van-Nostrand-Reinhold, New York, 1979.

Johnson, A.W. and Fowler, P.G., "Measured lifetimes of rotational and vibrational levels of electronic states of N_2," *J. Chem. Phys.* **53**, 65, 1970.

Kee, R.J., Dixon-Lewis, G., Warnatz, J., Coltrin, M.E., and Miller, J.A., *CHEMKIN code*, Sandia National Laboratories, Report SAND86-8246, 1986.

Kivel, B. and Bailey, K., "Tables of radiation from high temperature air," AVCO Research Lab., *Research Report 21*, 1957.

Klubnikin, V.S., *High Temperature*, **13**, 439, 1975.

Klynning, L. and Pagès, P., "The band spectrum of N_2^+," *Phys. Scripta* **25**, 543, 1982.

Kuz'menko, N.E., Kuznetsova, L.A, Monyakin, A.P., Kuzyakov, Y.Y, and Plastinin, Y.A., "Electronic transition probabilities and lifetimes for electronic excited states of diatomic molecules," *Usp. Fiz. Nauk.* **127**, 451, 1979.

Lahmani, F., Lardeux, C., Solgadi, D., "Collision-induced relaxation of NO $C^2\Pi(v'=0)$ and D $^2\Sigma^+$ (v'=0)," *Chem. Phys. Letters*, **81**, 531, 1981.

Langhoff S.R. and Bauschlicher, C.W., "Theoretical study of the first and second negative systems of N_2^+," *J. Chem. Phys.* **88**, 329, 1988a.

Langhoff, S.R., Bauschlicher, C.W., and Partridge, H., "Theoretical study of the NO γ system," *J. Chem. Phys.* **89**, 4909, 1988b.

Langhoff, S.R., Partridge, H., Bauschlicher, C.W., and Komornicki, A., "Theoretical study of the NO β system," *J. Chem. Phys*, **94**, 6638, 1991.

Larrabee, R.D., *J. Opt. Soc. of America*, **49**, 619, 1959.

Lavrov, B.P., "Calculation of Thermodynamic Functions for N_2, O_2 and NO," *SUDAAR-605*, Department of Aeronautics and Astronautics, Stanford University, Stanford CA 94305, 1991.

Le Duff, Y., Chergui, M., Boursey, E., and Schwentner, N., "Intensity enhancement of the NO $C^2\Pi(v=0)$ fluorescence in the presence of rare gases," *Chem. Phys. Letters*, **127**, 557, 1986.

Leger J.M., Coudert, J.F., Grimaud, A., and Fauchais, P., "Study of a nitrogen DC plasma jet at pressures between 20 and 100 kPa using optical and thermal diagnostics. Lecture on Experimental Results, *Proceedings of the Workshop on Hypersonic Flows for Reentry Problems*, Antibes, France, 1990.

Lewis, B.R., Berzins, L., and Carver, J.H., "Oscillator strengths for the Schumann-Runge bands of $^{16}O_2$," *JQSRT* **36**, 209, 1986.

Liu, Y. and Vinokur, M., "Equilibrium gas flow computations. I. Accurate and efficient calculation of equilibrium gas properties," *AIAA-89-1736*, 1989.

Liu, Y. and Shakib, F., "A comparison of internal energy calculation methods for diatomic molecules[a)]," *Phys. Fluids A2*, **10**, 1884, 1990.

Meyerott, R.E., Sokoloff, J., and Nicholls, R.W., "Absorption coefficients of air," GRD TR 60-277, *Geophysical Research Papers*, **68**, 1960.

Mitchner, M. and Kruger, C.H., *Partially Ionized Gases*, John Wiley & Sons, New York, 1973.

Moreau, S., Laux, C.O., Chapman, D.R., MacCormack, R.W., "A more accurate Non-Equilibrium AIr Radiation code: NEQAIR Second Generation," *AIAA-92-2968*, 1992.

Nerem, R.M., "Stagnation point heat transfer in high enthalpy gas flows," Flight Dynamics Lab., Wright Patterson Air Force Base, OH, *TDR-64-11*, 1964.

Nicholls, R.W. and Jarmain, W.R., "*r*-centroids: average internuclear separations associated with molecular bands," *Proc. Phys. Soc.* **69**, 253, 1955.

Nicholls, R.W., "Transition probabilities of aeronomically important spectra," *Ann. Geophys.* **20**, 144, 1964.

Nicholls, R.W., "Note on the electronic transition moment variation on the *r*-centroid approximation in the interpretation of spectral line intensities of diatomic molecules," *JQSRT* **14**, 233, 1974.

Nicholls, R.W., "Transition probability data for molecules of astrophysical interest," *Ann. R. Astro.* **15**, 197, 1977.

Ogurtsova, N.N., Podmoshenskii, I.V., and Shelemina, V.M., "The radiative power of air, N_2 and CO_2 at 10,000 K," *Teplofizika Vysokikh Temperatur*, **6**, 788-793, 1968.

Ortiz, M., Perez, A., and Campos, J., "Experimental lifetime for the $B^3\Pi_g(v=0)$ level of N_2," *Physica C* **150**, 440, 1988.

Owano, T.G., Gordon, M.H., and Kruger, C.H., "Measurements of the radiation source strength in argon at temperatures between 5000 and 10 000 K," *Phys. Fluids B*, **2**, 3184, 1990.

Page, W.A. and Arnold, J.O., "Shock layer radiation of blunt bodies traveling at reentry velocities," *NASA TR-R193*, 1964.

Park, C., "Calculation of Nonequilibrium Radiation in the Flight Regimes of Aeroassisted Orbital Transfer Vehicles," *Thermal Design of Aeroassisted Orbital Transfer Vehicles*, H.F. Nelson ed., *Progress in Aeronautics and Astronautics*, **96**, 395-418, 1985a.

Park, C., "Nonequilibrium Air Radiation (NEQAIR) Program: User's Manual," *NASA TM 86707*, Ames Research Center, Moffet Field, CA 94035, 1985b.

Park, C., *Nonequilibrium Hypersonic Aerothermodynamics*, Wiley, New-York, 1989.

Piper, L.G. and Cowles, L.M., "Einstein coefficients and transition moment variation for the NO($A^2\Sigma^+$-$X^2\Pi$) transition," *J. Chem. Phys.* **85**, 2419, 1986.

Piper, L.G., Holtzclaw, K.W., Green, B.D., and Blumberg, W.A.M., "Experimental determination of the Einstein coefficients for the N_2(B-A) transition," *J. Chem. Phys.* **90**, 5337, 1989.

Piper, L.G., Tucker, T.R., and Cummings, W.P., "Electronic transition moment variation and Einstein coefficients for the NO($B^2\Pi$-$X^2\Pi$) system," *J. Chem. Phys.* **94**, 7667, 1991.

Prasad, C.V.V., Bernath, P.F., Frum, C., Engleman, R., "Fourier transform jet emission spectroscopy of the $B^2\Sigma^+$–$X^2\Sigma^+$ transition of CN," *J. Mol. Spec.*, **151**, 459, 1992.

Reed, T.B., "Induction-coupled plasma torch," *J. Appl. Phys.*, **32**, 821, 1961.

Rehfuss, B.D., Suh, M.-H., Miller, T., "Fourier transform UV, visible, and infrared spectra of supersonically cooled CN radical," *J. Mol. Spec.*, **151**, 437, 1992.

Reynolds, W.C., *STANJAN* code, Mechanical Engineering Department, Stanford, CA 94305-3030.

Rhodes, R. and Keefer, D., "Numerical modeling of a radio frequency plasma in argon," *AIAA J.*, **27**, 1779, 1989.

Rizzo, A., Graham, R.L., and Yeager, D.L., "Accurate transition moments between the $A^3\Sigma_u^+$, $B^3\Pi_g$, and $B'^3\Sigma_u^-$ of N_2 using multiconfigurational linear response," *J. Chem. Phys.* **89**, 1533, 1988.

Rottke, H. and Zacharias, H., *J. Chem. Phys*, **83**, 4831, 1985.

Roux, F. and Michaud, F., "Investigation of the rovibrational levels of the $B^3\Pi_g$ state of $^{14}N_2$ molecule above the dissociation limit N(^{4}S) + N(^{4}S) by Fourier transform spectrometry," *Can. J. Phys.* **68**, 1257, 1990.

Roux, F., Michaud, F., and Vervloet, M., "Extension of the analysis of the $C^3\Pi_u$-$B^3\Pi_g$ system of nitrogen molecule by Fourier transform spectrometry," submitted to *J. Molec. Spectrosc.*, 1992.

Schadee, A., "The relation between the electronic oscillator strength and the wavelength for diatomic molecules," *JQSRT* **7**, 169, 1967.

Schadee, A., "Unique definitions for the band strength and the electronic-vibrational dipole moment of diatomic molecular radiative transitions," *JQSRT* **19**, 451, 1978.

Sharma, S.P., and Gillespie, W.D., "Nonequilibrium and equilibrium shock front radiation measurements," *J. Thermophys. Heat Transfer*, **5**, 257-265, 1991a.

Sharma, S.P., Gillespie, W.D., and Meyer S.A., "Shock front radiation measurements in air," *AIAA-91-0573*, 1991b.

Tauber, M.E., Palmer, G.E., and Yang, Lily, "Earth atmospheric entry studies for manned Mars mission," *J. Thermophysics. Heat Transfer*, **6**, 193-199, 1992.

Tourin, R.H., *Spectroscopic Gas Temperature Measurement. Pyrometry of Hot Gases and Plasmas*, Elsevier, New York, NY, 1966.

Tsukiyama, K., Munakata, T., Tsukakoshi, M., and Kasuya, T., "Fluorescence lifetimes of single rotational levels of NO $B^2\Pi$ and C $^2\Pi$," *Chem. Phys. Letters*, **137**, 315, 1987.

Tsukiyama, K., Munakata, T., Tsukakoshi, M., and Kasuya, T., "Fluorescence lifetimes of NO $A^2\Sigma^+$ (v'=3 and 4), $C^2\Pi$(v'=0) and $D^2\Sigma^+$(v'=0) studied by tunable VUV laser excitation," *Chemical Physics*, **121**, 55, 1988.

Vidal, C.R., Cooper, J., and Smith, E.W., "Hydrogen Stark-broadening tables," *Astrophys. J. Suppl. Series No. 214*, **25**, 37-136, 1973.

Vincenti, W.G. and Kruger C.H., *Introduction to Physical Gasdynamics*, Chapter I, Wiley, 1965.

Werner, H.-J, Kalcher, J., and Reinsch, E.-A., "Accurate *ab initio* calculations of radiative transition probabilities between the $A^3\Sigma_u^+$, $B^3\Pi_g$, $W^3\Delta_u$, $B'^3\Sigma_u^-$ and $C^3\Pi_u$ states of N_2," *J. Chem. Phys.* **81**, 2420, 1984.

Whiting, E.E., Arnold, J.O., Lyle, G.C., "A computer program for a line-by-line calculation of spectra from diatomic molecules and atoms assuming a Voigt line profile," *NASA TN D-5088*, 1969.

Whiting, E.E., Schadee, A., Tatum, J.B., Hougen, J.T., and Nicholls, R.W., "Recommended conventions for defining transition moments and intensity factors in diatomic molecular spectra," *J. Mol. Spectrosc.* **80**, 249, 1980.

Wiese, W.L., Smith, M.W., and Glennon B.M., *Atomic Transition Probabilities*, National Standard Reference Data series, National Bureau of Standards 4, 1966.

Zare, R.N., "Calculation of intensity distributions in the vibrational structure of electronic transitions," *J. Chem. Phys.* **40**, 1934, 1964.

3.0 PUBLICATIONS AND PRESENTATIONS

To date this program has resulted in the following publications and presentations:

Girshick, S. L., and C. H. Kruger, "Evidence of Secondary Flow in Faraday MHD Generators," 21st Symposium on Engineering Aspects of Magnetohydrodynanmics, Argonne, IL, June 1983.

Kruger, C. H., and S. L. Girshick, "A Review of MHD Boundary Layer Research at Stanford, with Emphasis on Measurements of the Effects of Secondary Flows," 8th International Conference on MHD Electrical Power Generation, Moscow, USSR, 1983.

Self, S. A., and L. D. Eskin, "The Boundary Layers Between Electrodes and a Thermal Plasma," IEEE Trans. Plasma Science P.S. 11, 279-285, Dec. 1983.

Girshick, S. L., and C. H. Kruger, "The Transverse Flow Field in an MHD Channel", IEEE International Conference of Plasma Science, May 14-16, 1984, St. Louis, MO.

Girshick, S. L., and C. H. Kruger, "Measurements of Secondary Flow in an MHD Channel," 22nd Symposium on Engineering Aspects of Magnetohydrodynamics, Mississippi State University, MS. June 26-28, 1984.

Girshick, S. L., and C. H. Kruger, "Experimental Study of Secondary Flow in an MHD Channel," 23rd Symposium on Engineering Aspects of MHD, Somerset, PA, June 1985.

Reis, J. C., and C. H. Kruger, "Experimental Study of Secondary Flow in an MHD Channel," 23rd Symposium on Engineering Aspects of MHD, Somerset, PA, June 1985.

Girshick, S. L., Ph.D. Thesis, HTGL Report No. T-250, Dept. of Mechanical Engineering, Stanford University, Stanford, CA, August 1985.

Self, S. A., and L. D. Eskin, "Plasma-Sheath Structure for an Electrode Contacting an Isothermal Plasma: I. Formulation and Quasi-Neutral Solution," 38th Gaseous Electronics Conference, Monterey, CA, October 1985.

Eskin, L. D., and S. A. Self, "Plasma-Sheath Structure for an Electrode Contacting an Isothermal Plasma: II. An Electrically Isolated (Floating) Electrode," 38th Gaseous Electronics Conference , Monterey, CA, October 1985.

Jaffe, S. M., M. Mitchner, and S. A. Self, "Electron-Ion Recombination Rates in an Atmospheric Pressure Plasma," 38th Gaseous Electronics Conference, Monterey, CA, October 1985.

Kruger, C. H., "Boundary Layer Phenomena in MHD Generation," 3rd US/Japan Symposium on MHD, Hakone, Japan, August 1985.

Kruger, C. H., "Stanford MHD Program: MHD Secondary Flows," US/Japan Workshop, Honolulu, HI, March 1986.

Jaffe, S. M., M. Mitchner, and S. A. Self, "Electron-Ion Recombination Rates in an Atmospheric Pressure Plasma," 39th Gaseous Electronics Conference, Madison, WI, October 1986.

Eskin, L. D., and S. A. Self, "Plasma-Sheath Structure for an Electrode Contacting an Isothermal Plasma: III. Cathodes," 39th Gaseous Electronics Conference, Madison, WI, October 1986.

Girshick, S. L., and C. H. Kruger, "Experimental Study of Secondary Flow in a Magnetohydrodynamic Channel," J. Fluid Mech. 170, 233-252, 1986.

Girshick, S. L, and C. H. Kruger, "Secondary Flow in a Linear MHD Channel with Applied Axial Current," 9th International Conference on MHD Electrical Power Generation, Tsukuba, Ibaraki, Japan, 1986.

Kruger, C. H., and R. C. Goforth, "New Measurements of Secondary Flow in an MHD Channel," 25th Symposium on the Engineering Aspects of MHD, Bethesda, MD, 1987.

Jaffe, S. M., M. Mitchner, and S. A. Self, "Measurement of the Recombination Rate of Cs^+ and e^- in High Pressure Molecular Gases," 40th Gaseous Electronics Conference, Atlanta, GA, October 1987.

Eskin, L. D., and S. A. Self, "Plasma Sheath Structure for an Electrode Contacting a Thermal Plasma, Including Electron Energy Effects," 40th Gaseous Electronics Conference, Atlanta, GA, October 1987.

Reis, J. C. and C. H. Kruger, "Turbulence Suppression in Combustion-Driven Magnetohydrodynamic Channels," J. Fluid Mech. 188, 147-157, 1988.

Goforth, R. C. and C. H. Kruger, "Measurements of the Effect of Interaction Parameter and Wall Temperature on Secondary Flow in an MHD Channel," 26th Symposium on the Engineering Aspects of MHD, Nashville, TN, June 1988.

Eskin, L. D. and S. A. Self, "The Transition from Diffuse Mode to Constricted Mode Current Transfer for a Plane Electrode Contacting a Thermal Plasma," 41st Gaseous Electronics Conference, Minneapolis, MN, October 1988.

Goforth, R. C and C. H. Kruger, "An Investigation of Secondary Flow in an MHD Channel," 27th Symposium on the Engineering Aspects of MHD, Reno, Nevada, June 1989.

Laux, C., and T. Owano, M. Gordon, and C. H. Kruger, "Measurement of the Volumetric Radiative Source Strength in Air for Temperatures Between 5000 and 7500K," AIAA/ASME 5th Joint Thermophysics and Heat Transfer Conference, Seattle, WA, June 1990.

Goforth, R. C. and C. H. Kruger, "Secondary Flows in MHD Channels," 28th Symposium on the Engineering Aspects of MHD, Chicago, IL, June 1990.

Gordon, M.H. and C. H. Kruger, "Electronic Quenching Effects of Atom-Molecule Interactions in a Non-Equilibrium Plasma at Atmospheric Pressure," 43rd GEC, Urbana-Champaign, IL, October 1990.

Owano, T.G. and C.H. Kruger, "Electron-Ion Three Body Recombination Coefficient of Argon," AIAA 22nd Fluid Dynamics, Plasma Dynamics & Lasers Conference, Honolulu, Hawaii, June 1991.

Gordon, M.H. and C. H. Kruger, "Ultra-Violet Recombination Continuum Electron Temperature Meaurements in a Non-Equilibrium Atmospheric Argon Plasma," AIAA 22nd Fluid Dynamics, Plasma Dynamics & Lasers Conference, Honolulu, Hawaii, June 1991.

Rosa, R.J., C.H. Kruger and S. Shioda, "Plasmas in MHD Power Generation," IEEE Transactions on Plasma Science (invited), pp. 1180-1190, December 1991.

Laux, C.O., S. Moreau, D.R. Chapman, C.H. Kruger and R.W. McCormack, "Numerical Predictions of Ultra-Violet Signatures," Missile Signatures Meeting, NASA-Ames Research Center, Moffett Field, CA, April 14-15, 1992.

Laux, C.O. and C. H. Kruger, "Arrays of Radiative Transition Probabilities for the N_2 First and Second Positive, NO Beta and Gamma, N_2^+ First Negative, and O_2 Schumann-Runge Band Systems," Journal of Quantitative Spectroscopy and Radiative Transfer, Vol. 48, No. 1, pp. 9-24, July 1992.

Laux, C.O., S. Moreau and C.H. Kruger, "Experimental Study and Improved Modeling of High-Temperature Air Radiation," AIAA 23rd Plasmadynamics and Lasers Conference, Nashville, TN, AIAA 92-2969, July 1992.

Laux, C.O., S. Moreau and C.H. Kruger, "Radiative Emission of High-Temperature Air," Second European Congress on Thermal Plasma Processes, Paris, France, September 7-9, 1992.

Owano, T.G., C.H. Kruger and R.A. Beddini, "Electron-Ion Three-Body Recombination Coefficient of Argon," accepted by AIAA Journal, to appear Jan. 1993.

Goforth, R. C. and C. H. Kruger, " An Investigation of Secondary Flow in an MHD Channel," submitted to AIAA Journal.

4.0 PERSONNEL

The following personnel contributed to this report:

Charles H. Kruger	Senior Associate Dean, School of Engineering, Professor, Department of Mechanical Engineering.
Christophe Laux	Research Assistant, High Temperature Gasdynamics Laboratory, Department of Mechanical Engineering (M.S. Mechanical Engineering, Ecole Centrale De Paris 1988)